University of Groningen

Material structure and functionality in product manufacturing

Zijlstra, Gerrit

Publication date:
2018

Material Structure and Functionality in Product Manufacturing

Proefschrift

ter verkrijging van de graad van doctor aan de
Rijksuniversiteit Groningen
op gezag van de
rector magnificus prof. dr. E. Sterken
en volgens besluit van het College voor Promoties.

De openbare verdediging zal plaatsvinden op

vrijdag 23 november 2018 om 12.45 uur

door

Gerrit Zijlstra

geboren op 6 Juli 1989
in het Bildt

Supervisor
Prof. dr. J. Th. M. De Hosson

Co-supervisor
Dr. V. Ocelík

Assessment committee
Prof. dr. ir. H. Terryn
Prof. dr. ing. J. Post
Prof. dr. P. Rudolf

Material structure and functionality in product manufacturing

Gerrit Zijlstra

PhD thesis
University of Groningen

The front cover shows the *cubic space division*. The cubes illustrate a simple skeleton architecture of a metal system structure. The *cube with magic ribbons* on the back symbolizes the complexity that such a cubic system can inhibit. Both images are created by M.C. Escher.

university of groningen   faculty of mathematics and natural sciences   zernike institute for advanced materials

CONTENTS

Chapter 4
Structure and evolution of steel oxide layers   **57**

Chapter 5
Phase transformation characteristics   **83**

Chapter 6
Steel surface passivity and local corrosion behaviour   **119**

Chapter 1

Introduction

"Substance is the static warp, method the dynamic woof of man's material culture" - R.J. Forbes

As long as mankind is roaming the earth, he uses tools to aid in his daily activities. Sticks, rocks and bones assist for hunting, shelter building and fighting. Tools which can be just found in nature, or attained by a simple modification as cutting or polishing. At a certain moment, perhaps by accident, someone kicked what seemed a rock into a pit fire and discovered -after he took it from the fire- that this rock (or was it a metal?) is more easy to hammer in shape: the first metallurgist was born. Development of the use of materials and their properties can be considered as an ongoing interplay of processing and resulting functionality. The driving force of this interplay is the progressive insight in the structure and applications.

For certain civilizations the evolution of metallurgy can be seen to contain four stages: considering metal ore as stones; processing metal by hammering, cutting, etc.; the ore stage, going from ore to metals by techniques as smelting; iron or steel stage, where the importance lies in complex treatments as tempering and quenching, rather than varying in composition [1]. These stages are not a description of the history of a specific metal, but a general result of discoveries and inventions. There is an important difference between the discovery of the properties of materials and the invention of things to do with them [1,2]. The progress in materials science is not linear step-by-step: one may say that progress is a matter of jerky motion directed by invention and insight in the utilization of the material

world [1]. As the materials science progress is a non-linear motion, materials properties are determined by non-linear effects and collective behaviour of defects over various length scales and time scales [3]. For mechanical properties, the microstructure (intrinsic property) determines the mechanical behaviour. However, at very small scales this no longer holds [3]. The current challenge is to describe these mechanisms at the small scale, to be able to make valuable computing models which can take these mechanisms into account [3]. In engineering, material properties are described such that macroscopic dimensions do not play a role. They are often estimated, for example by applying a safety factor because thorough testing of structure design is too exhaustive on time and resources.

In the field of corrosion science a thrive is to pinpoint processes on a sub-micrometer scale. When corrosion is influenced or dominated by local effects, the study of these effects increasingly requires thorough knowledge on the microstructure.

As miniaturization and net shaping are the trends in product manufacturing, further development in material processing is awaiting material descriptions and surface modification with increasing attention for the microstructure.

Figure 0. Cartoon of Fokke & Sukke [4]. The text on top (in Dutch) reads: Fokke & Sukke don't make any progress. Left: "Go invent the wheel", Right: "Dude! Go invent the wheel yourself!".

1.1 Historic background

The first metallurgist, perhaps a bit fortuitous, was able to work with found lumps of copper. As this process was developed and copper used for everything varying from tools to jewelry, for the Egyptians the stone-age era had gradually shifted into the copper-age. When copper is mixed with tin or arsenic, a much harder alloy named bronze is created. Obtaining copper from the smelting of a copper-rich ore requires a temperature of about 700-800 °C. Alloying requires the melting of copper which takes plase at 1085 °C. Both processes need temperatures higher than a burning campfire can deliver, so the early man had to use some kind of an oven. Pottery furnaces where already extensively used and suitable for this operation [1]. The Egyptians mastered the art of bronze working and were able to cast small and big statues of breathtaking beauty [5]. From which time on the Egyptians started to produce iron is not sure. The lack of iron archaeological specimens and smelting sites is troubling the debate. Garland [5] however suggests that iron could have been used, but that the objects simply vanished. As it was probably extremely scarce, it is plausible that any abundant objects were re-melted. Besides, the Egyptian soil contains a lot of chlorine. Iron pieces which are left in the soil for hundreds or thousands of years simply oxidize and crumble to dust. Despite all of this, extremely old iron artefacts have been found. The oldest known so far are tube-shaped beads found in the tombs at Gerzeh, dated to 3300 B.C. [6]. Another valuable object is a dagger found in the tomb of Tutankhamun (18th dynasty, 1332-1323 B.C.). How is it possible that some objects are still present, while others have been vanished? Partly because the beads and dagger were not buried in the ground and partly because they are rich in nickel [5–7]. So, knew the Egyptians the importance of nickel to strengthen the iron against corrosion, and how to make an iron-nickel alloy? Definitely not! The use of iron making was probably not even developed yet. They were familiar with the metal, as it can be a side product (slag) in the copper melting process. Petrie [8] found large amounts of iron-slag and tools in the Egyptian city of Naukratis, from which he concluded that this city was a center of iron trade and the main source of manufactured iron to the Greeks. This he dated to the 5th - 6th century B.C., much later than the retrieved objects. The answer to the question comes from outside Egypt, but can be found in the written language. The Egyptians used the hieroglyph *biA* meaning -mineral, metal, iron- as a generic term for iron-like material, including the mineral hematite (Fe_2O_3) [6,7,9]. From the 13th century B.C. on the hieroglyph was expanded to *biA*-

n-pt, which can be translated to "Iron of the sky" [6,7]. It is suggested [6] that a broad observed natural event such as a meteorite shower or a large meteorite impact caused a disruption in the language and left the Egyptians no doubt about the origin of the metal. Indeed, meteorites can contain iron with a high percentage of nickel. Fragments of these meteorites were hammered into the desired shape. Therefore the Egyptians did not leave us an ancient method to preserve iron, but merely demonstrated the strength of (unintended) corrosion protection for thousands of years.

East of Egypt, in India, remarkable iron pillars are preserved. Most famous is the Delhi Iron Pillar, forged around 400 A.D.. The pillar is situated in the open-air and is therefore subject to a constant change of the weather. Surprisingly it is in an excellent condition without a thick oxidation scale. Although the production of steel was already established, the early Indian steel production was facing problems with the amount of phosphor in iron. Due to sub-optimized furnaces, lack of lime and temperature, an abundance of phosphor was included in the forged steel [10]. In general too much phosphor is not desirable as it makes steel brittle, but in the case of the (static) pillars it appears to be a blessing in disguise. The amount of phosphor is sufficient to form a layer of iron-hydrogen-phosphate-hydrate (phosphorus rust) on the surface, which protects the pillar from further rusting.

Even further east, in China, a similarity with the Egyptian story can be found. In the Hubei province a bronze water vessel -*Pan*- was found, dating to the $4^{th} – 3^{rd}$ century B.C.. Although being buried for all this time, the surface glitters with dark brown shining, which is in contrast with the green patina that can be expected on a bronze object [11]. After examination of the surface, it was found that the bronze was coated with a layer rich in chromium and iron of at least 1 mm thick. This coating has an extra-terrestrial origin, probably originating from one of many observed meteorites at that time [11]. It is very unlikely that the ancient Chinese produced this alloy themselves, as the chromium containing mineral chromite is not present in this area [11,12]. Although the Chinese were not able to produce such an alloy or even knew about chromium, they recognized the extraordinary features of the meteorite alloy.

In separated parts of the (ancient) world, civilizations started to understand how to work with iron and learned the properties of its alloys. It would take however a couple of millennia before experimenters were able to systematically investigate the contribution of various elements to the corrosion properties of iron.

It was in 1820 when Michael Faraday, together with James Stodart, experimented with adding noble metals to steel in order to: "*Ascertain whether any of such alloys would, under similar circumstance, prove less susceptible to oxidation*" [13]. One year later Pierre Berthier, who was inspired by this publication, followed by adding chromium to steel. By combined reduction of iron- and chromiumoxides, he was able to make an alloy called Ferrochromium with 17 to 60 % Cr [14,15]. In turn this inspired Faraday and Stodart to alloy with chromium. They noticed that a higher iron-chromium alloy resulted in a better corrosion resistance compared to plain steel [16], but the used content of only 3% Cr was not enough to improve the corrosion resistance dramatically. Several researchers worked independently on different aspects of chromium steel in the late 19th- beginning of the 20th century. Phillip Monnartz concluded in 1908 that there is a steep drop in the corrosion rate when the alloy contains nearly 12% of chromium [17] - leaving it stainlessness - and indicated that "passivity" is the responsible phenomenon. He stated that: "*Passivation is dependent upon the oxidizing conditions, as opposed to reducing conditions*". So far, Monnartz is known as the first person recognizing the cause of, what he named, the stainlessness of steel.

1.2 Steel in product manufacturing

The industrial use of stainless steel started with Harry Brearley. He made a cast of stainless steel for rifle barrels, but upon failure for that purpose looked for another application. With trial and error he succeeded in convincing a manufacturer of cutlery to use his "rustless steel". The manufacturer first tested the steel with vinegar and said: "*This steel stains less*". From that moment on he referred to the material as stainless steel and succeeded in making a dozen of knives. The result of their efforts was a first order of 7 tons of stainless steel in 1914 [15]. The demand for this type of steel increased rapidly once it also found its usage in the production of exhausts for aeroplanes in the beginning of the first World War. The application nowadays is found in many branches including tools, food packaging and architecture, resulting in a wobbling world stainless melt shop production of 48 million tons in 2017 [18].

Stainless steels can roughly be divided in two classes based on their microstructure: ferritic and austenitic. The austenitic stainless steels have an excellent corrosion resistance, but are limited in hardness. The austenitic Cr-Ni

grades are the 'general purpose grades' and for example used for transport pipes and storage tanks of food and chemicals [19]. Ferritic stainless steels do not contain the relative expensive nickel and therefore have a lower cost. They are soft with a good formability and easy to polish. Examples for applications are washing-machine drums and exhaust pipes [20]. A sub-class is formed by the ferritic-martensitic family members which are also soft in the ferritic phase, but can be transformed to martensite which increases the hardness. These alloys encounter the necessary minimum chromium content of 10.5 weight percent, one of the factors making them less corrosion resistant. The low chromium content is therefore a tradeoff between formability and corrosion resistance. These alloys are often used in cutlery and (chirurgical) knives, because of their ability to stay sharp. In fact, Harry Brearly used a martensitic stainless steel to produce his cutlery.

Manufacturers of stainless steel products gratefully make use of the natural (passive) protection system. However, some user conditions demand more corrosion resistance of the product. A surface treatment can be applied to match the increased requirements: chemical passivation. In this process free iron is dissolved in nitric acid and simultaneously the chromium at the surface oxidizes. This process causes an enrichment of chromium at the surface resulting in a more adequate passive layer compared to a natural air-formed layer. Prior to chemical passivation, the surface must be cleaned thoroughly. This can be done by pickling, where contamination and the old passive film is removed with the help of aggressive nitric-, hydrochloric- or hydrofluoric acids [20,21]. An alternative is electrochemical removal. Hereby a potential is applied between the product (anode) and a cathode, causing the oxides to dissolve in the electrolyte of sulfuric- or phosphoric acid.

In a different approach, chromium is externally applied. One method is electroplating, where an effective thick Cr_2O_3 coating is induced by soaking the product in an extreme acidic bath (pH of 0) of CrO_3 with sulfuric acid. A current is applied to grow a Cr_2O_3 (with chromium from the bath) layer on the product. A secondary path is applying a chromium containing paint. Both approaches imply that the used chromium is in a 6^+ valence state. These paints have been extensively used by e.g. the Dutch Ministry of Defence [22,23], but also in a civilian organisation as the Dutch Railways [24]. However hexavalent chromium compounds, also known as Cr(VI), are carcinogenic to humans [25–27]. Workers who ground these surfaces and inhaled the Cr(VI) compound rich dust, were found

later to suffer from lung cancer. Therefore Cr(VI) compounds are excellent for protection of the applied surface, not for human health.

Miniaturization and net shaping of metallic parts are important topics in manufacturing of consumer products, resulting in narrower tolerances for smaller products and more stringent requirements [28]. As a result, the manufacturing process of high precision components suffers from an ever increasing number of complexities, i.e. the components become geometrically more demanding by specifications in three dimensions. To keep up with this trend, the development cost of new products as well as the development time of new products have to be reduced.

A common type of material used is (AISI420) ferritic-martensitic stainless steel, which is soft in the ferritic state and therefore easy to deform into a desired shape. After shaping a thermal treatment can be applied to harden the material. During this step unwanted shape change in the formed products can occur. Also the surface is subjected to alterations due to changes in temperature and composition of the present gass. Steel with a high chromium content is preferable for corrosion protection, but the high content makes the alloy more brittle and therefore decreases the forming properties. A trade-off between the two functions is reached with the class of AISI 420 steel, with a Cr-content between 12-14 wt.%. As this is approaching the limit of 12 %, where Monnartz observed a steep change in the corrosion rate [17], maintaining the quality of the passive layer throughout the production process is of upmost importance. Both shape change and a sub-optimal passive layer of the products require finishing steps afterwards and should be avoided.

1.3 Thesis aim and outline

The aim of this thesis is twofold:

1. To validate experimentally the reliable and robust constitutive models that are essential for effective process simulations aimed at reducing product development time and costs;
2. To characterize and optimize surface treatment for the required stringent surface properties.

The thesis aim is addressed by means of the following Chapters:

Chapter 2 summarizes the basic characteristics of the main material investigated in this work. An introduction to a typical metal component production process is provided. Furthermore a short description of the principal experimental techniques is given.

Chapter 3 concentrates on the effect of the residual stress state on a product during its manufacturing. The mechanical behavior during forming and heat treatment is characterized by experiments and implemented in a Finite Element routine, in order to measure and model product shape change.

Chapter 4 aims at investigating the influence of the different crystal orientations of a polycrystalline stainless steel substrate on the formation of the thermal oxide layer.

Chapter 5 presents the results obtained with in-situ high temperature Electron Backscatter Diffraction (EBSD), in a study on the dynamics of interphase boundary motion during transformations. A novel method was designed to derive the velocity of the interphase boundaries from the EBSD phase maps.

Chapter 6 sheds light on the time scales involved with passivation of steel surfaces. Corrosion resistance of these surfaces is assessed by a very local determination of the oxide layer chemical composition.

1.4 References

[1]   R.J. Forbes, Metallurgy in Antiquity. A notebook for archaeologists and technologists, E.J. Brill, Leiden, the Netherlands, 1950.

[2]   C.S. Smith, Materials and the Development of Civilization and Science, Sci. New Ser. 148 (1965) 908–917.

[3]   J.R. Greer, J.T.M. De Hosson, Plasticity in small-sized metallic systems: Intrinsic versus extrinsic size effect, Prog. Mater. Sci. 56 (2011) 654–724. doi:10.1016/j.pmatsci.2011.01.005.

[4]   Reid, Gelijnse, V. Tol, Fokke & Sukke boeken geen vooruitgang, Fokke&Sukke Scheurkal. (2017).

[5]   H. Garland, Ancient Egyptian Metallurgy, Charles Griffin & Company LTD., London, 1927.

[6]   D. Johnson, J. Tyldesley, T. Lowe, P.J. Withers, M.M. Grady, Analysis of a prehistoric Egyptian iron bead with implications for the use and perception of meteorite iron in ancient Egypt, Meteorit. Planet. Sci. 48 (2013) 997–1006. doi:10.1111/maps.12120.

[7]   D. Comelli, M.D. Orazio, L. Folco, M. El-halwagy, T. Frizzi, G.C. Vittozzi, R. Alberti, V. Capogrosso, A. Elnaggar, H. Hassan, A. Nevin, F. Porcelli, M.G. Rashed, G. Valentini, The meteoritic origin of Tutankhamun's iron dagger blade, 9 (2016) 1–9. doi:10.1111/maps.12664.

[8]   W.M.F. Petrie, Naukratis, in: Vol. I, London, 1886: p. 39.

[9]   A. Erman, H. Grapow, Wörterbuch der aegyptischen Sprache, Berlin: Akademie-Verlag, 1982.

[10]   R. Balasubramaniam, On the corrosion resistance of the Delhi iron pillar, Corros. Sci. 42 (2002) 2103–2129. doi:10.1016/S0010-938X(00)00046-9.

[11]   W. Luo, T. Li, The use of chromium minerals in the 4th-3rd century BC China? A preliminary study of a bronze Pan unearthed from Jiuliandun Graves, Hubei Province, central southern China, J. Raman Spectrosc. 43 (2012) 303–306. doi:10.1002/jrs.3015.

[12]   M. Zhou, W. Bai, Chromite deposits in China and their origin, Miner. Depos. 27 (1992) 192–199.

[13]   J. Stodart, M. Faraday, Experiments on the alloys of steel made with a view to its improvement, Philos. Mag (Ser. 1). 56 (1820) 26–35. doi:10.1080/14786442008652361.

[14]   P. Berthier, Sur les Alliages du chrôme avec le fer et avec l'acier, Ann. Chim. Phys. XVII (1821) 55–64.

[15]   H. Kobb, History of Stainless Steel, ASM International, 2010.

[16]   J. Stodart, M. Faraday, On the Alloys of Steel, Philos. Trans. R. Soc. London. 112 (1822) 253–270.

[17]   P. Monnartz, Beitrag zum Studium der Eisen-Chromlegierungen unter besonderer Berücksichtigung der Säurebeständigkeit (The study of iron-chromium alloys with special consideration of resistance to acids),

Metallurgie. 8 (1911) 161–176.

[18]   International Stainless Steel Forum, Stainless Steel in Figures 2017. http://www.worldstainless.org.

[19]   Outokumpu, Handbook of Stainless Steel. http://www.outokumpu.com.

[20]   I.S.S. Forum, The Ferritic Solution, (2012). http://www.worldstainless.org.

[21]   S. Ramachandra, Resource Recovery and Recycling from Metallurgical Wastes, Elsevier, 2006.

[22]   De Volkskrant, Defensie erkent aansprakelijkheid chroom-6-ziekten; verzweeg gezondheidsrisico's voor medewerkers, 04-06-2018. https://www.volkskrant.nl/nieuws-achtergrond/defensie-erkent-aansprakelijkheid-chroom-6-ziekten-verzweeg-gezondheidsrisico-s-voor-medewerkers~b3cbcdb3/.

[23]   NOS, Defensie aansprakelijk voor schade door kankerverwekkend chroom-6, 01-06-2018. https://nos.nl/artikel/2234597-defensie-aansprakelijk-voor-schade-door-kankerverwekkend-chroom-6.html.

[24]   N. (Dutch Railways), Chromium trioxide dossier. https://www.ns.nl/en/about-ns/dossier/chrome-6/chromium-trioxide-dossier.html.

[25]   International Agency for Research on Cancer, CHROMIUM Compd. http://www.iarc.fr.

[26]   M.B. Heringa, P. Janssen, Achtergrondinformatie over chroom-6: gebruik, voorkomen in het leefmilieu en gedrag in het lichaam, Rijksinst. Voor Volksgezond. En Milieu. (2018). doi:10.21945/RIVM-2018-0051.

[27]   Rijksinstituut voor Volksgezondheid en Milieu, Chroom-6 en ziekten: wat is er bekend uit de wetenschap?, (2017). https://www.rivm.nl/Documenten_en_publicaties/Wetenschappelijk/Rapporten/2018/Juni/Achtergrondinformatie_over_chroom_6_gebruik_voorkomen_in_het_leefmilieu_en_gedrag_in_het_lichaam.

[28]   R. van Ravenswaaij, R. van Tijum, P. Hora, T. van den Boogaard, U. Engel, Towards zero-defect manufacturing of small metal parts, in: Towar. Zero Fail. Prod. Methods by Adv. Model. Tech. a Process Integr. Virtual Control IDDRG 2013 Conf., ETH Zurich, 2013: pp. 87–92.

Chapter 2

Production process and characterization techniques

This Chapter summarizes the basic charasteristics of the materials investigated in this work. An introduction to a typical metal component production process is provided. Furthermore a short description of the principal experimental techniques used, is given.

2.1 Material

The material under investigation is a martensitic stainless steel of class AISI 420. The chemical composition is listed in Table 2.1 [1]. In comparison: the steel that Harry Brearly used for his first cast of stainless steel contained about 13% Cr and 0.24% C [2] and is therefore also categorized as AISI 420. It is remarkable that this widely used steel remains a subject for studies, even 100 years after its industrial introduction. During those years the control of the the thermal-mechanical forming processes has improved significantly. The research is driven by the impetus to produce products with increasing precision and quality in conjuncture with optimized corrosion resistance.

Table 2.1. Chemical composition of AISI 420 martensitic stainless steel (wt.%).

C	Cr	Si	Mn	P	S	Fe
Min 0.15	12-14	1	1	0.04	0.030	Bal

The final steps in the production of the steel, after casting, include cold rolling followed by annealing. The final product of the steel manufacturer is provided as a coiled strip of steel in the ferritic phase. Due to the rolling, the material is heavily textured and exhibits anisotropic behavior. For isotropic materials often the Von Mises definition is applied as a yield function, i.e. describing when elastic strain is followed by plastic strain. For anisotropic materials one of the simplest and most used is the yield function proposed by Hill in 1948 [3]:

$$2f = F(\sigma_{yy} - \sigma_{zz})^2 + G(\sigma_{zz} - \sigma_{xx})^2 + H(\sigma_{xx} - \sigma_{yy})^2 + 2L\sigma_{yz}^2 + 2M\sigma_{zx}^2 + 2N\sigma_{xy}^2 = 1, \tag{2.1}$$

where σ_{ii} are the stresses in the rolling- (RD), transverse- (TD) and thickness (Z) direction, and σ_{ij} the shear stress components *F, G, H, L, M, N* are characteristic constants reflecting the state of anisotropy. They are derived from the yield stresses σ_0, σ_{45} and σ_{90} along 0, 45 and 90° to the RD; and corresponding R_0, R_{45}, R_{90} [3,4]. The R-value corresponds to the stress applied 0, 45 and 90° to the RD and defined as the ratio of the strain of the width (ε_{width}) and the thickness ($\varepsilon_{thickness}$):

$$R = \frac{\varepsilon_{width}}{\varepsilon_{thickness}} \tag{2.2}$$

Higher R-values imply a stronger anisotropic effect.

2.2 Material structural changes during a production process

Commonly used consecutive processing steps for the fabrication of metallic components include metal forming so as to achieve the desired shape and followed by a heat treatment to obtain the required mechanical strength. Metal forming is done by deep drawing, according to well-established techniques [5]. A preeminent way in studying the plastic and elastic deformation behaviour, is by making a cup according to the Erichsen method [6]. First a round plate, the blank, is punched from a strip. The blank is stretched with a punching die with a spherical tip until the desired cup is formed. The anisotropic behaviour can be seen in Fig. 2.1 by the ears appearing on the open side of the cup.

Figure 2.1. Cup made by deep drawing of a cound blank. Earing is seen on the open side of the cup, facing the bottom of the image.

This steel is iron based, but also consists of hard inclusions called carbides with the chemical structure $Cr_{23}C_6$ [7]. The phase diagram for Fe-Cr-C steel with 13% Cr is shown in Fig. 2.2. The steel is initially in the ferritic phase with a Body Centred Cubic (BCC) structure, which is also denoted as α-iron. As seen in Fig. 2.2 the ferrite transforms to austenite Face Centered Cubic (FCC) or γ-iron between 850 and 1080 °C. In the austenite matrix much more carbon can be dissolved compared to ferrite, where only 0.022 wt.% C can be present in solid solution. The phase change to austenite will act as a driving force for the carbides to dissolve. Depending on longer dwell time and higher temperatures, more carbides will dissolve. Typical austenitization conditions for martensitic stainless steel ranges between 925 – 1065 °C for 30 to 90 minutes [8].
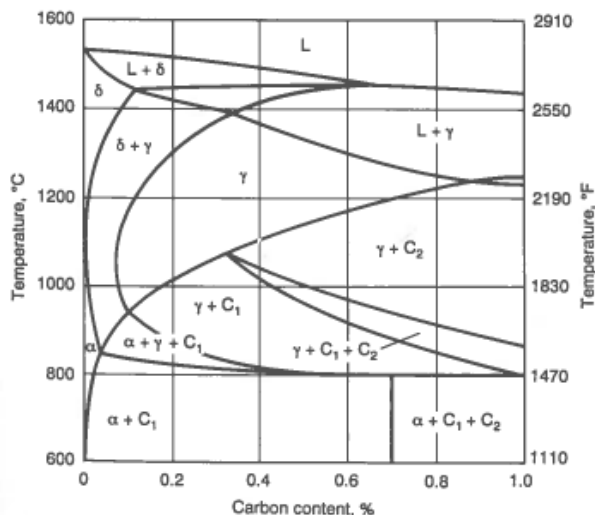
Figure 2.2. Phase diagram for Fe-Cr-C steel with 13% Cr (obtained from [1]).

The chromium carbides can be made visible at the surface by etching. This process involves exposure of the surface to a reactant which can enhance surface features as grain boundaries or different phases, due to localized attack or different dissolution rates. Several etchants have been tested, the best result was obtained with exposure for 15 s to Vilella's picrine, which consists of 1g Picric acid + 5ml HCl + 100ml ethanol.
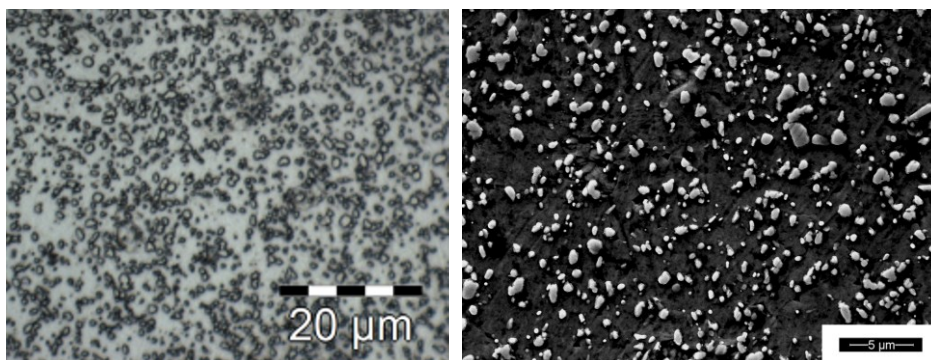
Figure 2.3.Ferritic steel etched with Vilella's pricrine for 15 s. Left image obtained by optical microscopy, right by SEM (with higher magnification).

The surface after etching is shown in Fig. 2.3, where the carbides can be recognized as the spherical particles which cover a significant part of the surface. The contrast in the SEM image of Fig. 2.3 of the carbides (white) with the black background of the substrate allowes area indexation. Image analysis was done with the open source software ImageJ [9]. The as-received ferritic material was indexed with the "analyze particle" function, to give a carbide areal density of 14.1 ± 1 %. The error orginates from the chosen threshold value for the cut-off between black and white areas, which may vary a bit when the black-white contrast is not optimal. As a demonstration of the carbide dissolution in the austenite region: after heating for 10 minutes at 980 °C followed by quenching to room temperature, the carbide areal density decreased to 9.1 ± 1 %. In a similar temperature treatment, but at a higher temperature of 1050 °C the areal fraction decreased to 2.7 ± 1 %.

The as-received material has also been analyzed with ImageJ to obtain the carbide size distribution as shown in Fig. 2.4. Carbides smaller than 0.05 μm were cut-off from the analysis. The distribution shows that the chromium carbides are not monodisperse or normally distributed. The large positive skew indicates the

presence of significant more small than large carbides. The larger carbides may be the result of conglomeration of many small carbides during a heat treatment in the steel manufacturing process.

The presented data and analysis of the etched chromium carbides is a selection of a broader work, which can be found in [10].
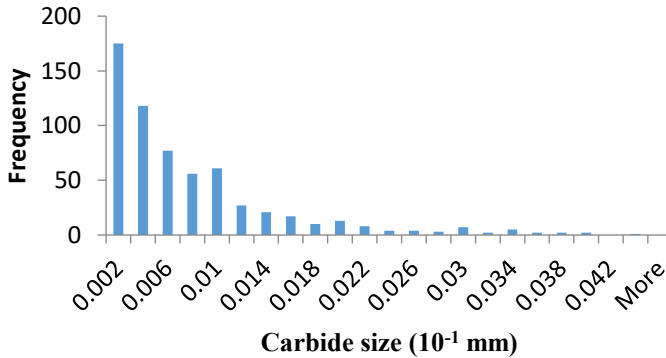
Figure 2.4.Carbide size distribution of the as-received ferritic steel.

The phase transformation from ferrite to austenite is a crucial step in the thermal hardening process. While at the austenite temperature region, carbon from the carbides dissolves in the iron matrix. Upon rapid cooling to room temperature, the carbon becomes trapped in the matrix and the much harder phase martensite is formed. The amount of carbon dissolving depends on the austenitization time and temperature, as has previous been quantified by the reduction of carbides. The fraction of martensite after cooling is dependent on the amount of free carbon. An increase of the fraction of martensite also increases the hardness. Vickers Hardness tests have been performed to quantify this dependency. In Fig. 2.5 the hardness values after cooling are given for various austenitization temperatures (900 to 1100 °C) and dwell times of 2 and 10 minutes The as-received material exhibits a value of 176 ± 4 HV. More results are presented in [11].
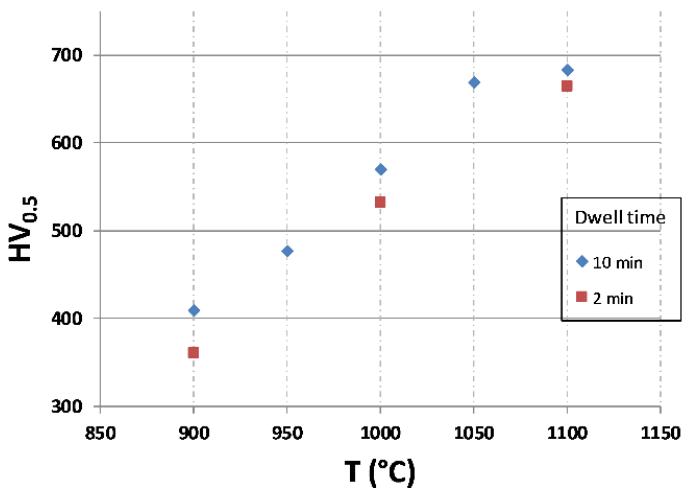
Figure 2.5.Vickers hardness after hardening at various austenitization temperature for two different dwell times.

In order to obtain the desired hardness, a carefull balance between temperature and dwell time must be found. To ensure a repeatable achieved hardness value, furnaces with a large heat capacity are used in order to maintain a stable temperature. An industrial scale pushbelt furnace for a continuous hardening process is shown in Fig. 2.6.

Figure 2.6. Industrial sized pushbelt furnace (at Philips Drachten).

2.3 Characterization techniques

A rather diverse set of experimental techniques has been used to characterize various materials aspects, such as, structure, composition and mechanical behavior. A summary of most of the microscopy techniques is listed in Table 2.2. The abreviations and a description of the main working principle will be presented later.

Table 2.2. List of analysis equipment used in this work.

Abbreviation	Technique	Description
OM	Light Microscopy	Olympus VANOX-T
SEM	Scanning Electron Microscopy	Philips XL-30 ESEM Lyra SEM
EDS	Energy-dispersive X-ray Spectroscopy	EDAX
EBSD	Electron Backscatter Diffration	EDAX – with TSL OIM setup
XPS	X-ray Photoelectron Spectroscopy	Surface Science SSX-100 ESCA
AFM	Atomic Force Microscopy	Veeco Dimension 3100
ToF-SIMS	Time-of-Flight Secondary Ion Mass Spectroscopy	Lyra3 with TofWerk-C module
XRD	X-ray Diffraction	Brukers and Pan-Analytical

2.3.1 High temperature structural and mechanical testing

Mechanical properties at elevated temperature were determined using a setup consisting of a Zwick / Roell Z30 tensile bench, equipped with a three-zone Maytec furnace with induction heating elements. During regular tensile testing at room temperature, straining of the tensile bar can be deduced by recording the movement of the tensile bench grips. As the grips are solid pieces of metal, they are a heat sink for the tensile bar at high temperature. Due to the expected thermal gradient at the top and bottom of the tensile bar, the recorded strain is not a description of the strain at the centre of the tensile bar. Therefore the strain was

determined by continuous measurement of the spacing of two markers at the centre of the tensile bar. To this end a Laser Extensometer (LEX) P-100 from Fiedler Optoelektonik [12] was installed in front of the furnace, as shown in Fig. 2.7. The tensile bars are laser cutted from a 0.5 mm thick plate with a length of 43 mm and width of 20 mm.

The LEX has a rotating deflector in the Scanner which projects a laser beam parallel with the tensile bar. The reflected beam from the specimen is redirected by a mirror into the reciever. Since the LEX derives the positon of the markers from the transition of the marker and the background, the contrast between the tensile bar and the marker should be as large as possible. Therefore, the highly reflective metal surface is treated with a heat resistant black paint along the bar. Two heat resistant markers were applied using white TiO_2 paint. This paint combination works well to temperatures as high as 800 °C. Above this temperature, the black paint becomes a bit fainter, but the white paint becomes dark.

Figure 2.7. Tensile bench equipped with a furnace and a laser extensometer installed in front of the furnace.

The elevated temperature tensile tests were performed taking the following procedure. First, the furnace was pre-heated to the desired temperature. Once this temperature was reached, the tensile bar was placed in the furnace and clamped in the top grip of the bench, allowing the tensile bar to expand during its heating trajectory. Then the furnace was closed and the top and bottom holes were filled with mineral wool. After a ceramic tube with glass for the laser was inserted (closing the porthole of the laser to prevent air flow), the furnace had to be heated

again. Once the target temperature of the furnace was reached again, five minutes were taken for the system to stabilize. Since the material has a thickness of 0.5 mm, it is assumed that the temperature of the tensile bar is the same as the furnace after stabilisation.

Due to the huge difference in furnace temperature and the room temperature, a lot of convection occurs. Hot air is exhausted at the opening of the furnace where the tensile bar comes out to be clamped, and through the porthole made for the laser beam. At the same time air at room temperature is sucked in through the gap at the bottom of the furnace and the lower part of the porthole. The strong convection induces turbulence in and outside the furnace. Due to the turbulence, the laser beam goes through a medium with a frequently changing refraction index, as hot air has a different refractive index compared to air at room temperature. Therefore, the amount of reflected light that reaches the reciever is decreasing with increasing turbulence, (i.e. increasing temperature gradient). The remaining light that reaches the reciever can have travelled different paths for the two markers and therefore will be noticed by the reciever with a delay, so the markers appear to be at different places. To prevent and reduce the turbulence, the furnace has been insulated and sealed as much as possible.

The porthole in the furnace through which the laser beam is guided into the furnace, is closed to prevent turbulence. For this purpose a ceramic tube of Al_2O_3 has been designed. A piece of heat resistant glass was cut out and placed in the ceramic tube on the outside of the furnace to close the tube, preventing an air flow. The tube was slid into the furnace up to the tensile bar. Therefore the air inside the tube was shielded from any remaining turbulence inside the furnace. After 5 minutes the system was stable with the air in the tube at a similar temperature as the furnace. In this way, the noise in the measurements has been reduced from 25 μm to values below 1 μm. Markers on the tensile bars were spaced 50 mm. Due to the precision better than 1 μm, the error in the strain was only 0.002 % at 700 °C

2.3.2 Imaging

A conventional way to make microscopical (surface) observations is using an optical microscope. The use of a glass lense with a magnification allowing observation of microbes, dates back to 17th century with Antonie van Leeuwenhoek, who became the most skillful person in polishing glass lenses [13]

in those days (taking the secrets of the methodology with him into his grave). The optical images in this work were obtained using an Olympus Vanox-T.

The theoretical resolution limit of a light microscope was derived by Ernst Abbe in 1873, and yields: $d = \frac{\lambda}{2\,n\,sin\alpha}$. According to Abbe this was the highest achievable magnification. The limit was streched by Frits Zernike, our Physics Nobel Laureate in 1953 for the phase contrast microscope.

With the electron microscope the used wavelength λ is not the one of visible light, but the wavelength of electrons instead. The wavelength of electrons is proportional to the acceleration voltage: $\lambda_e \propto \frac{1}{\sqrt{V_{acc}}}$. An estimate of the spatial resolution of a Scanning Electron Microscope (SEM) gives about 4–6 nm when using accelerating voltages ranging between 15 and 30 kV. The systems used in this work are a Philips XL30 ESEM and a Lyra SEM, both operated with a Field Emission Gun.

2.3.3 Structure

A material crystal orientation can be determined with Electron Backscatter Diffration (EBSD), also known as Orientation Imaging Microscopy (OIM). Here, incident electrons from an SEM-gun hit the surface under an angle of about 70° such that the electrons are inelastically scattered. These backscattered electrons form a diffraction (Kikuchi) pattern from which the crystal phase and orientation can be determined. To achieve this, the surface must be flat (mirror polished) and free from deformation zones caused by e.g. scratches. Furthermore, the material must have crystalline grains at the surface of at least a few tenths of nanometers in order to obtain a clear diffraction pattern. Due to the common used electron acceleration voltage of about 25 kV and incident angle, the information depth is limited to 100 nm. EBSD is therefore a surface sensitive technique. For further reading on orientation imaging microscopy is referred to [14].

For the characterization of an oxide layer on the surface, both classical X-ray Diffraction (XRD) as well as grazing incidence XRD (GIXRD) operating with Cu anode, can be used. With XRD crystal orientations and crystallographic phase of the bulk are measured. With GIXRD the angle of incidence is so small that information is obtained from a limited depth in the order of 20 nm. Therefore, the phase and distribution of the crystal orientations are measured from the outermost layer of the specimen. In contrast to EBSD, the XRD methods do not give spatial

information, but only the volume averaged crystallographic information over a large area.

EBSD is usually applied ab-initio and/or post-mortem a certain material treatment. Technical advances in, for example computing power, have decreased the collection time needed to map an area. Therefore subsequent maps can be made much faster, resulting in the ability to acquire more frames of a dynamical process. The good spatial resolution in combination with crystal phase and orientation determination makes EBSD an excellent technique to study structural dynamics during e.g. tensile tests or a heat treatment. Thermal in-situ EBSD experiments were conducted in a Tescan Lyra FEG/FIB dual beam microscope, equipped with an OIM system by EDAX including a Hikari super camera, which can achieve a maximum of 1400 indexed points per second. Annealing inside the microscope was performed with a Kammrath & Weiss heating module (see Fig. 2.8), which contains a ceramic resistance heater.
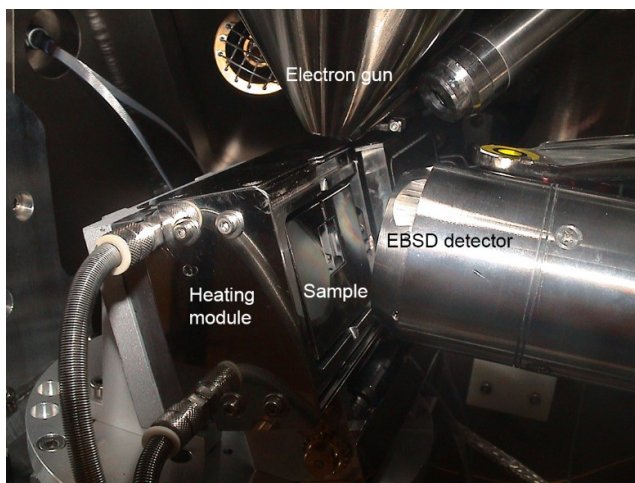
Figure 2.8. Experimental setup for High Temperature EBSD, showing position of the heating module with respect to the electron gun and the EBSD detector.

As heating is applied from the bottom side, a sample thickness of 0.5 mm was chosen to keep the thermal gradient in the sample to a minimum. The temperature control of the module is calibrated for optimal performance at elevated temperatures with a maximum of 1500 °C. The temperature could be maintained within a fluctuation of 0.1 °C through a coupled PID-temperature controller. The

temperature was monitored through thermocouples at the heating element and just above the specimen.

It is noteworthy that in-situ high temperature EBSD data collection differs from standard EBSD observations in a couple of issues. Although the Kammrath & Weiss heating module is actively water cooled, there is a strong thermal radiation from the sample surface directly facing the EBSD phosphorous screen detector. This creates an additional background signal, which has to be subtracted from the collected Kikuchi patterns.

At constant temperature the background could be collected just once for the non-diffracted back scattered electrons and the thermal radiation component. However, when temperature is changed the so-called background signal for the CCD camera has to be collected before optimal Kikuchi pattern recognition. This procedure requires an additional time to optimize observations at different temperatures. Another issue is the limited cooling ability of EBSD detector itself, which may lead to the substantial temperature increase and even to thermal damage of the phosphorous screen, especially for sample temperatures over 750 °C. We placed another thermocouple at its vicinity and retracted the whole EBSD detector for a while when its temperature exceeded 120 °C. Data collection is therefore limited to times less than 100 s at temperatures higher than 800 °C. Finally, a problem with the drift of SEM image, appearing mainly at moments when a substantial change in heating rate is required, has to be minimized/corrected. We did not perform OIM scans at these conditions. Final drift was always corrected by placing a selected object (e.g. small carbide particle or surface feature) into the SEM image center. Measurements with the foward-scattered-electron detector were not performed, since this detector has been removed to avoid its damage at high temperatures.

OIM analysis was performed with TSL OIM Analysis v.7.3 software. This included a two step data cleaning procedure with Grain Confidence Index Standardization (grain tolerance angle 5°, minimum grain size of 5 pixels, with a condition that grains contains multiple rows) and a Neighbor Orientation Correlation (level 4, tolerance 5, minimal Confidence Index 0.1). All remaining data points with a confidence index below 0.1 were removed and are shown as white points in OIM maps. It is worthwhile to note, that always less than 2.5% of the scanned points changed their crystal orientation after this cleaning and that the phase assignment to the particular point (ferrite or austenite) was not changed.

The time to make a mapping with EBSD is initially prescribed by the size of the map and the density of scanning points. Secondly, the hypothetical processing speed may suffer if the indexation time per Kikuchi pattern increases due to decreasing signal quality. This can require multiple frames averaging to improve the signal to noise ratio. Observation of the dynamics of interphase boundary movement demands a rapid successive mapping. Therefore, selection of scanning parameters is a trade-off between map size and spatial resolution (step size). This results in typical map parameters of a 30x30 μm^2 scanning area with step size 0.4 micrometer in a hexagonal type of grid, and an indexing speed of 50 points per second. The time between successive scans was 85 s, with an additional 15 s in isochronal experiments, when in the latter case background collection and correction had to be applied due to its change with temperature.

2.3.4 Surface chemical composition

Information about the surface chemical composition can be obtained in various ways. The most suitable technique depends on the required information, e.g. elemental distribution, valence state or a fine depth resolution. The techniques as Energy-dispersive X-ray Spectroscopy (EDS), X-ray Photoelectron Spectroscopy (XPS) and Scanning Auger Microscopy (SAM) rely on various processes which take place due to irradiation, as illustrated in Fig. 2.9. Detailed information on these techniques can be found in [15–18], a brief description is given below.
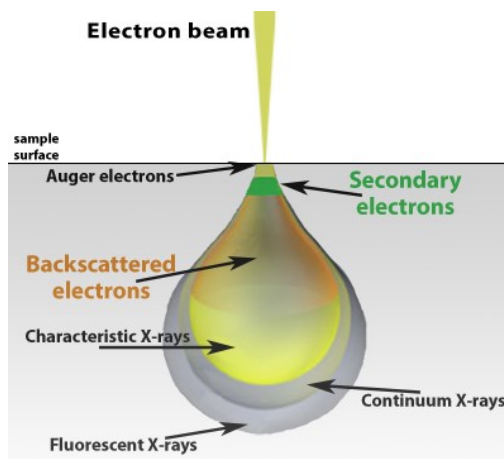

Figure 2.9. Interaction volume and characteristic radiation after irradiation by an electron beam, from [19].

EDS

EDS relies on an incident electron beam on an area of interest, often applied in a SEM. The incoming electron knocks out a core shell electron of the irradiated atoms. The energy release by an electron from an outer shell to fill the vacancy of the core shell, is in the form of an X-ray. These X-rays have a characteristic energy from which the parent atom can be determined. EDS is often used as a quantitative method to determine the atomic distribution, but is less accurated for lighter atoms up to oxygen. Although a very small area can be irradiated with the accurate electron beam, a large interaction volume is activated from which the X-rays are orginating. The precise volume is dependent upon the electron accelerating voltage, but is typically in the order of a few micrometers deep, and wide.

Auger spectroscopy

If we consider again a vacancy of the core shell caused by a knocked out electron from an incident elctron beam (a similar scenario as for EDS), the outer shell electron which is about to fill this vacancy, can also pass its energy to another outer shell electron which is than ejected. The ejected particle is called the Auger electron. Typically the detected Auger electrons originate from the atoms in the top of the specimens surface, from a depth less than 5 nanometers. This depth resolution in combination with the excellent lateral resolution of about 20 nm, allows for detailed mapping of the chemical composition.

XPS

The operational principle of XPS is somewhat the opposite of EDS. Here the surface of interest is irradiated with monochromatic X-rays, originating form e.g. an Al Kα X-ray source. Here the X-ray will knock out a core shell electron. The kinetic energy of this so called photoelectron is characteristic for the energy transition at the parent atom. The strength of the XPS is the resolution in resolving the kinetic energy of the photoelectron. The detailed energy spectrum can reveal chemical shifts in the atom bonding, from which the valence of the atoms in a certain structure or molecule can be determined. Similar to Auger, XPS is a very surface sensitive technique with an information depth of about 8-10 nm for perpendicular to the surface incident X-rays. Due to the spotsize of the X-ray beam, the lateral resolution is generally limited to a spot with a diameter of 100 μm.

Auger spectroscopy and XPS can applied for depth profiling for surface layers which are too thin (or vulnerable) to be analysed by making a cross section. This is done by alternating the removal of a certain layer and chemical analysis. Typical layers are removed or sputtered away with Ar^+ ions. In this work we applied Ar^+ ions with an energy of 2 kV, under a 50° degree angle of incidence with the normal of the specimen surface.

ToF-SIMS

Instead of an analysis after the removal of a certain layer, also the removed atoms themselves can be analysed with Time-of-Flight Secondary Ion Mass Spectroscopy (ToF-SIMS). ToF-SIMS (at Brno Tescan application lab) experiments have been conducted on a Tescan-Lyra system with a C-TOF module provided by TOFWERK. In this system, surface atoms are ionized (sputtered) through Ga-ions. Ionized atoms or molecules are attracted and collected in either positive or negative mode. The charged particles are separated by their characteristic Time-of-Flight. The mass resolution $M/\Delta M$ is 700-1100 Th/Th [20,21]. The result is a mass over charge spectrum from the spot where the Ga beam was focused, which allows e.g. detection of Fe-isotopes. The above mentioned setup is capable of mapping with high spatial resolution (smallest spot of ~20nm), which allows for detailed chemical mapping of the surface layer. By repeating the 2D mapping, also the chemical composition in depth (3D mapping) can be retrieved. An extensive background on SIMS can be found in [15,22].

2.4 References

[1]   J.R. Davis, ASM Specialty Handbook: Stainless Steels, 1994.

[2]   H. Kobb, History of Stainless Steel, ASM International, 2010.

[3]   R. Hill, A Theory of the Yielding and Plastic Flow of Anisotropic Metals, Proc. R. Soc. Lond. A. Math. Phys. Sci. 193 (1948) 281–297. doi:10.1098/rspa.1948.0045.

[4]   P. Dasappa, K. Inal, R. Mishra, The effects of anisotropic yield functions and their material parameters on prediction of forming limit diagrams, in: Int. J. Solids Struct., 2012: pp. 3528–3550. doi:10.1016/j.ijsolstr.2012.04.021.

[5]   V.P. Romanovski, Handbook of Cold Stamping, Machinery-Building, Moscow, 1979.

[6]   ISO 20482: Metallic materials — Sheet and strip — Erichsen cupping test.

[7]   C. García De Andrés, L.F. Álvarez, V. López, J.A. Jiménez, Effects of

carbide-forming elements on the response to thermal treatment of the X45Cr13 martensitic stainless steel, J. Mater. Sci. 33 (1998) 4095–4100. doi:10.1023/A:1004424329556.

[8]   ASM International, ASM Handbook Volume 04 - Heat Treating, 1991.

[9]   ImageJ. https://imagej.nih.gov/ij/.

[10]   J. Hopman, Influence of heat treatment on chromium carbide content in stainless steel, University of Groningen - Bachelor Thesis, 2016.

[11]   C. Jansen, Influence of time and temperature during hardening of a martensitic steel, University of Groningen - Bachelor Thesis, 2015.

[12]   Fiedler - Laser Extensometer P100, (n.d.). http://www.foe.de/en/products/lex/parallel.html.

[13]   Mystery of superior Leeuwenhoek microscope solved after 350 years, (2018). https://www.tudelft.nl/en/2018/tu-delft/mystery-of-superior-leeuwenhoek-microscope-solved-after-350-years/.

[14]   O. Engler, V. Randle, Introduction to texture analysis: macrotexture, microtexture, and orientation mapping, 2nd ed., CRC PRESS, 2010.

[15]   J.C. Vickerman, I.S. Gilmore, Surface Analysis – The Principal Techniques 2nd Edition, 2009. doi:10.1002/9780470721582.

[16]   D. Briggs, M.P. Seah, Practical Surface Analysis. 2nd Edn. Volume 1 — Auger and X-Ray Photoelectron Spectroscopy, Wiliey, Oxford, 1990.

[17]   J.I. Goldstein, D.E. Newbury, J.R. Michael, N.W.M. Ritchie, J.H.J. Scott, D.C. Joy, Scanning Electron Microscopy and X-Ray Microanalysis, 4th ed., Springer, NY, 2018.

[18]   C.D. Wagner, W.M. Riggs, L.E. Davis, J.F. Moulder, G.E. Muilenberg, Handbook of X-ray Photoelectron Spectroscopy, Perkin-Elmer Corporation, Minnesota, 1979.

[19]   NanoScience Instruments, Sample-Electron Interaction. https://www.nanoscience.com/technology/sem-technology/sample-electron-interaction/.

[20]   F. Drewnick, S.S. Hings, P. DeCarlo, J.T. Jayne, M. Gonin, K. Fuhrer, S. Weimer, J.L. Jimenez, K.L. Demerjian, S. Borrmann, D.R. Worsnop, A new time-of-flight aerosol mass spectrometer (TOF-AMS) - Instrument description and first field deployment, Aerosol Sci. Technol. 39 (2005) 637–658. doi:10.1080/02786820500182040.

[21]   T.H. Bertram, J.R. Kimmel, T.A. Crisp, O.S. Ryder, R.L.N. Yatavelli, J.A. Thornton, M.J. Cubison, M. Gonin, D.R. Worsnop, A field-deployable, chemical ionization time-of-flight mass spectrometer, Atmos. Meas. Tech. 4 (2011) 1471–1479. doi:10.5194/amt-4-1471-2011.

[22]   R.G. Wilson, F.A. Stevie, C.W. Magee, Secondary ion mass spectrometry: a practical handbook for depth profiling and bulk impurity analysis, Wiley, 1989.

Chapter 3

The role of stresses in product manufacturing

This Chapter concentrates on the effect of the residual stress state on a product during its manufacturing. Cold forming by deep drawing introduces large residual stresses. When the products experience a thermal treatment, these stresses relax and cause a shape change of the product. The mechanical behavior during forming and heat treatment is characterized by experiments and implemented in a Finite Element (FE) routine. Product shape change has been modelled and validated with experiments.

3.1 Introduction

Miniaturization and net shaping are the trends in manufacturing of consumer products, electronics and automotive, resulting in narrower tolerances for smaller products and more stringent requirements. As a result, the manufacturing process of high precision components suffers from an ever increasing number of complexities, i.e. the components become geometrically more demanding by specifications in three dimensions. Other critical quality requirements such as hardness, surface roughness and density [1–3] have to be produced within narrower specification limits. To keep up with this trend and to be competitive, the development cost of new products as well as the development time of new products have to be reduced. This can be achieved by increasing the predictability of production processes by Finite Element (FE) analysis. The advantage of this numerical analysis is the ability to model complex forming processes. In contrast,

the downside of FE analysis is the complexity in preparing input data from experimental results and selection of meaningful output variables.

It should be realized that in practice the complete product manufacturing consists of shaping operations (i.e. forming), heat treatments, finishing operations and assembly. When martensitic chromium steel is used as a base material, the most critical step lies in the middle of the production chain, i.e. the hardening of the steel. Here, residual stresses introduced by forming may cause plastic deformation during heating to the austenitization temperature. However, the material is commonly known to produce little shape change during the hardening because in most applications the material is already made stress-free prior to a heat treatment. Obviously, fewer finishing processes are needed when the product is already more accurate in shape after the hardening. A reduction of the finishing processes increases the production efficiency and therefore lowers the fabrication costs. As a consequence there is a strong need to simulate the shape of the components through the various processing steps so that the consequence of any modification of the production process can be predicted in advance. Also novel products can be tested thereby decreasing the design-to-product time.

For the aforementioned hardening, a thermal- driven process which should not be confused with work hardening, the typical austenitization temperature for martensitic stainless steel ranges between 925 – 1065 °C for 30 to 90 minutes [4]. After forming by cold work, which could include stretching and bending, the material has a high residual stress state [5]. In general we may say that there are three mechanisms responsible for the relaxation of residual stresses [6]: (i) At lower temperatures creep mechanisms (diffusional and dislocation creep affected by grain size) allow areas of tensile and compressive stresses to expand or contract, respectively; (ii) At high temperatures the yield strength decreases, promoting strain relieve through dislocation glide and dislocation creep mechanisms, and finally (iii) precipitation and ageing effects may lead to volumetric changes that can also relax the residual stress state. We should emphasize that in many circumstances it is a combination of processes and various relaxation mechanisms which may operate at the same time. When diffusional creep (Nabarro-Herring, Coble) occurs at low temperature it is still active at high temperature where dislocation creep and dislocation glide maybe become operational depending on the stress state, i.e. the ratio between then effective stress state and the temperature dependent shear modulus.

Although the hardening process is used to improve the mechanical properties of the formed product, it comes often at the expense of the shape change. If the shape change can be maintained and controlled during forming and hardening, the sequential finishing and assembly steps can be less costly as well as energy consuming.

Product forming operations as deep drawing, which include stretching and bending, introduce a high residual stress state [5]. Residual stresses arise from the natural shape between different regions, parts or phases [7,8]. These stresses can be measured by destructive techniques such as sectioning, contour, hole-drilling, ring-core and deep-hole [9] through the release of residual stresses upon removal of material from the specimen [10], either on a macroscopic scale or at a local scale [11,12]. Non-destructive methods as X-ray or neutron diffraction [7,13–15], ultrasonic methods and magnetic methods, usually measure a microstructure stress-related parameter [7,10].

Several authors have investigated various aspects of the heating cycle: i.e. FE modeling of cold forming [16,17], phase transformation [18] and quenching [19,20], including stress relaxation [21]. Furthermore, high temperature deformation [22] and the evolution of distortions during quenching [23]. Surm et al. [24] noticed the importance of the residual stress state during heating, attributing stress relieve to plastic deformation due to the decrease of the yield strength at high temperatures. Relaxation of residual stresses with a creep model has been shown in [25,26], however no predictions for shape change have been done.

In general, shape change of steel during a hardening treatment is attributed to the transformation induced stress or thermal stress [18,27,28]. But, little attention is paid to the role of residual stresses in the shape change at the lower temperatures of the heating cycle. In this Chapter we will measure and model the shape change during forming and hardening. In particular, we highlight the contribution of the low temperatures heating region to the overall shape change during hardening and the role of residual stresses.

However, as the individual processes are studied in depth, there is a gap for coupling the dedicated individual models. The aim of this study is to calculate and predict the shape change in a product based on interaction between phenomena rather than presenting a detaileded constitutive modeling of the individual material phenomena. To this end, a novel approach will be proposed to predict and validate the shape change during a hardening treatment of a metal formed product in 3-Dimensions. The overall idea is that forming of a metallic product induces

inhomogeneous strains resulting in residual stresses. The latter are calculated by using the commercial Finite Element (FE) software package 'Marc'. The residual stress distribution is obtained by making a comparison between the simulated work hardening with the hardness profile of the product.

The shape change (or total strain) can be seen as the sum of material phenomena; the elastic strain, plastic strain, creep strain, thermal strain and transformation strain. The calculation for the shape change during heating includes: elasticity, thermal expansion, plasticity, and creep. The assumption here is that the various shape changes can be added linearly to the total strain, with the same global stress acting on the various individual elements. Consequently, the underlying constitutive equations for a specific mechanism can be determined individually. Hence the combined total strain rate equation is written as the sum of the elastic strain ($\varepsilon_{elastic}$); plastic strain ($\varepsilon_{plastic}$); creep strain (ε_{creep}); thermal strain ($\varepsilon_{thermal}$) and transformation strain ($\varepsilon_{transfomation}$):

$$\varepsilon_{tot} = \varepsilon_{elastic} + \varepsilon_{plastic} + \varepsilon_{creep} + \varepsilon_{thermal} + \varepsilon_{transfomation} \qquad (3.1)$$

A regular FEM approach is strongly concentrated on one set of operation at the time, e.g. forming followed by the subsequent heat treatment. When multiple subroutines need to be taken into account simultaneously, the modeling space becomes impractically large as visualized in Fig. 3.1. Instead, two partial models are preferable. The full process chain model requires a smaller amount of model space. In this work a novel method is used to integrate these two models. The method allows to switch between FE analysis of the forming and the hardening. Since the material model of the forming and the material model of the hardening have a limited physical overlap, the models can be divided with minimal accuracy loss. Filling up the two resulting model spaces with data, results in a lower requirement of measurement data. This approach is called FlexMM, after Flexible Material Model.

Key in the simulation of the heat treatment step is the assumption that the residual stresses leads to creep and that the creep strains may predominate the shape change of the product.
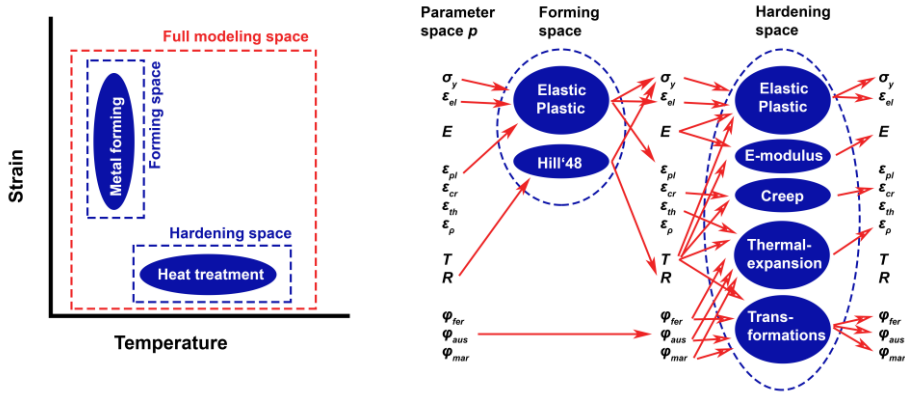
Figure 3.1. Schematic of the span of the modeling space for cold forming and heat treatment (Left), and the work flow through the parameter space p and subroutines, in the multi-stage forming-hardening model (Right). The symbols of p represent: σ_y the flowstress, ε_{el} the elastic strain vector, E the elastic modulus, ε_{pl} the equivalent plastic strain, ε_{cr} the equivalent creepstrain, ε_{th} the thermal strain, ε_ρ strain by mass density change, T the temperature, R the anisotropy and φ_{fer}, φ_{aus}, φ_{mar} the fractions of ferrite, austenite and martensite respectively.

3.2 Metal forming

Metal forming by deep drawing introduces residual stresses, which are not uniformly distributed along the cup [29]. In reference [30] it is shown that residual stresses increase due to pre-straining, with a relation that indicates a work-hardening (or strain-hardening) mechanism. In order to validate the FE calculations after deep drawing, we have visualized the residual stress by comparing the hardness of the actual formed cup with the simulation. Therefore the hardness of pre-strained material has been used to translate the calculated stress to hardness. This assumption/method has no influence on the further calculations of the evolution of the stresses during the heat treatment. Hardness measurements have been chosen, as they are an indirect but simple experiment to perform. The justification of this procedure can be found in [31], where a linear relation between the hardness and residual stress is derived.

The studied cup shaped products were fabricated using cold forming by deep-drawing, following the design rules and procedures described in [32]. The result is

a cup with a diameter of 20 mm and a height of 10 mm. The FE simulation of the forming has been done by implementing the deep-drawing parameters into the Marc software. Material specific properties as yield stress and Young's modulus at room temperature have been stated in the software. The deep-drawing is simulated using planar anisotropy and dislocation work hardening. The parameters of the Hill'48 planar anisotropy model are derived from the magnitude of the flow stress in various directions with respect to the rolling directions (see Chapter 2). The dislocation work hardening description from [33] is calibrated with the data presented in Fig. 3.2.
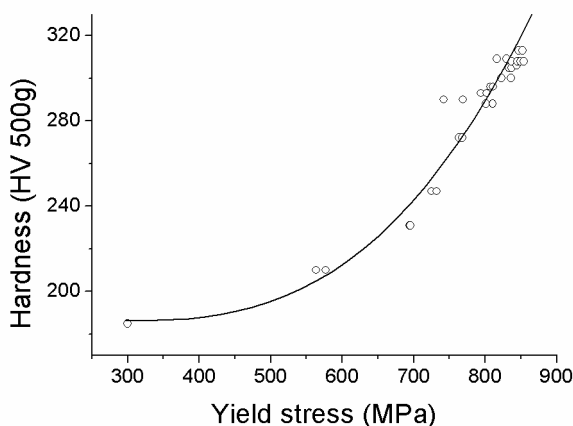
Figure 3.2. Hardness of the pre-strained samples (circles) as a function of flow stress measured in tension, with a continuous fit.

It is known that the hardness changes depending on the amount of cold work, i.e. work hardening [33]. Experimentally this is verified with tensile tests on pre-strained material. The stress at the onset of plastic deformation (yield stress) for various strains is recorded. Thereafter the hardness of each strained sample is measured. The hardness with the corresponding flow stress after the tensile test is depicted in Fig. 3.2. Since the flow stress depends on the amount of strain, an indirect relation between the strain (thus residual stress) and the hardness exists. The calculated residual stresses of a cup after forming can therefore be expressed by a calculated hardness profile. The prediction of the hardness is verified in Fig. 3.3 by comparing the calculation with a hardness profile of a fabricated cup.
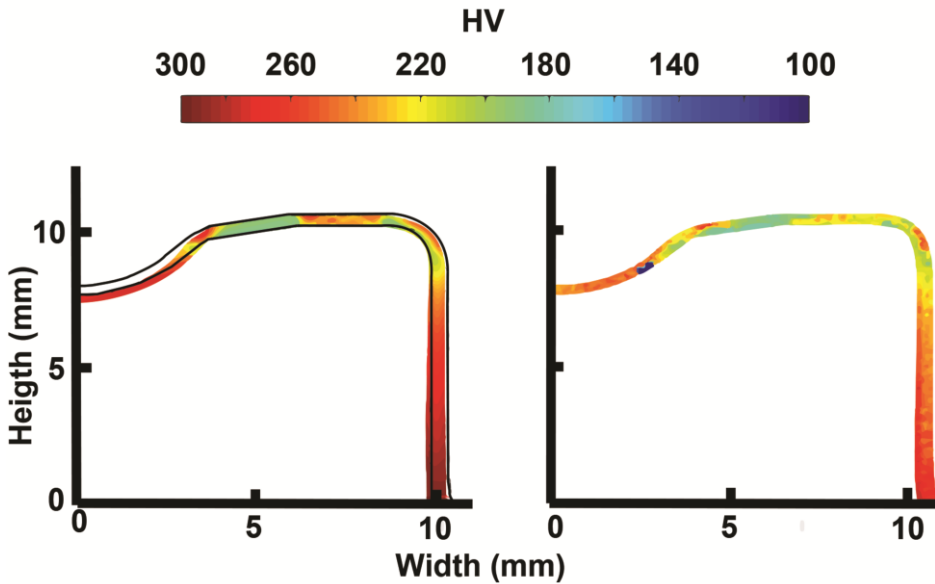
*Figure 3.3. Hardness profile measured on the product cross-section **a**), and FE simulation **b**). The black line in a) is the contour of the simulated cup b) and indicates the shape deviation between the product and the simulation.*

The cup was first cold mounted in an epoxy resin and then dissected twice. The mounting prevented spring-back of the cut section and therefore a relaxation of the residual stress. The surface was then carefully prepared for hardness measurements by consecutive refining steps of grinding and polishing: a common method of sample preparation for hardness measurements and EBSD microscopy (where surface stress perturbations by cutting and polishing should be erased). The hardness is measured by a grid of indentations. The contour is obtained by interpolation of the hardness values for the body, and extrapolation to the edges [34].

Based on symmetry, only half of the product cross-section is shown. The black line in Fig. 3.3 represents the contour of the simulated cup. The difference can be due to geometrical errors in the settings of the press, which cause more deformation of the fabricated cup compared to the FE simulation. The overall hardness distributions match quite well, indicating that the calculation of the residual stresses is validated.

Calculation of cold forming requires a plasticity model. Due to rolling during manufacturing of the steel, the material is textured. Therefore, the plasticity

behavior of the material is not homogeneous for all directions. This anisotropic mechanical behavior of sheet steel is described by the Lankford coefficient or planar R-values [35]. The R-values are experimentally derived by tensile testing from the magnitude and the plastic deformation in various directions with respect to the rolling direction, and yield 1.35, 1.81, 1.17, 1.03 and 1.02 for R_0, R_{90}, R_{45}, $\sigma_{0/90}$ and $\sigma_{0/45}$ respectively. R_0 is determined parallel with-, and R_{90} perpendicular to the rolling direction.
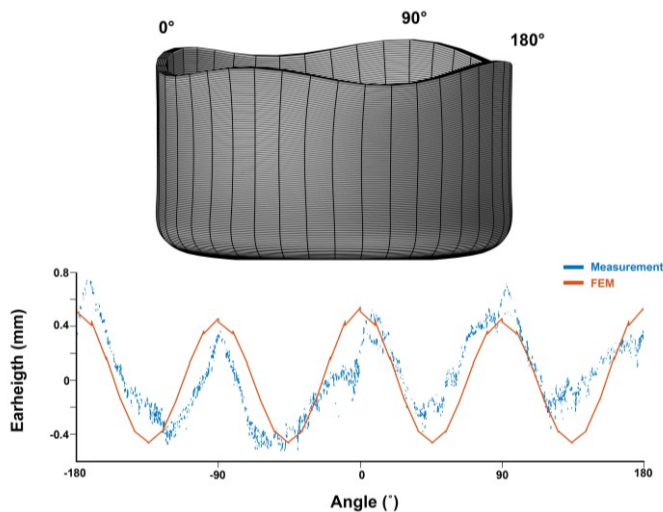
Figure 3.4. Result of the metal forming. Top: shape after forming in the FE model. Bottom, comparison of the height of the ears from the calculated cup (solid red line) and a measured specimen (scattered blue dots). The ear profiles vary from cup to cup due to small imperfections like cutting burrs in the blank, which cause large defects in the edge of the cup, but have minor impact on the deep drawing process. Compression in the edge of the cup has a leveraging effect on the edge defects. Also slight eccentric movement during the forming process can affect the height of the individual ears. The specimen showed here suffered less from the possible forming defects, but some imperfections in the blank can still be seen.

The elastic-plastic behavior is calculated using the commercial available software Marc [37]. The subroutine requires a yield curve of the material. The data for the yield curve was acquired by tensile testing and for the higher strains by rolling, and fitted with an Estrin description [36,38]. The flow stress is thus described by a constant*(dislocation density)$^{0.5}$. This description is used to calculate the cold forming of the cup by deep drawing. The FEM calculation was

validated in two ways. First, deep drawing introduces residual stresses. This pre-straining can be related to work–hardening. The calculated stress distribution can be indicated by a hardness measurement profile [31] as is demonstrated in Fig. 3.3. Second, anisotropic behavior is typically exhibited by earing at the open side of the cup. The earing (amplitude and phase) has been calculated and compared to the measured average profiles of 46 cups. The profiles are compared in Fig. 3.4 and show a good agreement in both the ear-height, as in the angle with respect to the rolling direction.

3.3 Thermal hardening treatment

Typically the forming process is followed by a thermal hardening treatment. The thermal profile of the experiments described in this section consists of heating with a ramp of 4 °C/s to a temperature of 970 °C. After a dwell time of 900 s, the cups are cooled down to room temperature using a cooling rate of 6 °C/s. The temperature evolution of the yield stress of this material during heating and cooling was experimentally determined using compression (carried out in a plastodilatometer) and tensile tests. The temperature evolution of the relative change in length and the volume fractions of austenite (during heating) and martensite (during cooling) were also obtained using high resolution dilatometry experiments.

3.3.1 Mechanical behavior at elevated temperature

Tensile tests in the range of RT – 900 °C were performed. A set with this range is shown in Fig. 3.5. The dependence of the yield stress on temperature is derived from these curves and is displayed in Fig. 3.6. The minimum value at 800 °C marks the onset of austenitization. The E-modulus also has a temperature dependence [39–44] as derived from the tensile experiments. This is not always very reliable since at elevated temperature creep effects make the elastic regime shorter and often not even linear. For the experiments above room temperature, the markers on the tensile bar were measured with a high precision, prior to the beginning of the tensile test. The start of the tensile tests at 300 °C caused disturbance in the recording of the strain, with the result of a derivation of the elastic modulus which is too high. The values of 500 - 700 °C have been obtained from tensile tests with various strain rates, i.e. $0.012 – 0.00012 \ s^{-1}$.
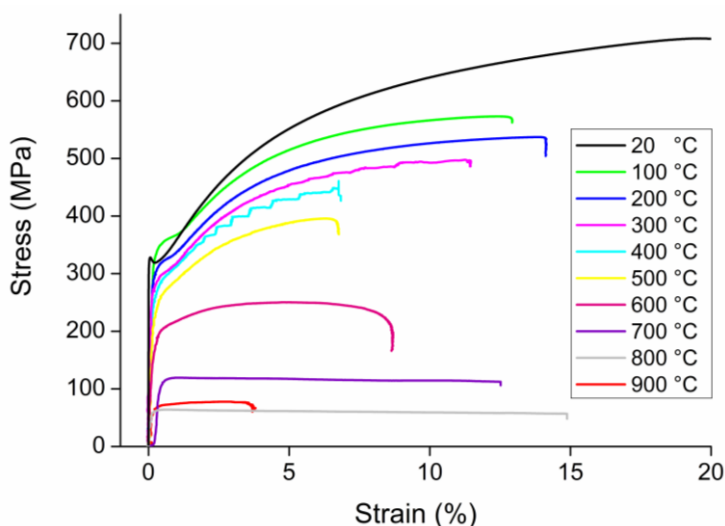
Figure 3.5. True stress – true strain diagram of tensile tests at elevated temperatures, obtained with a strain rate $\dot{\varepsilon}$ = 0.012 s^{-1}.

Especially at these temperatures creep phenomena influenced the elastic response and made the elastic regime shorter and non-linear for the highest temperatures and lowest strain rates. Given these results, tensile tests at elevated temperatures are not the optimal experiments to determine the Young's modulus. The Refs. [39–43] supplemented with the work of Masumoto [44] with acoustic waves on similar steels, indicate a mainly linear decrease of Young's modulus up to 700 °C. Therefore we assume a linear fit to the data of Fig. 3.6 is appropriate, with a fixed starting point at E_T / E_{RT} = 1 at room temperature.
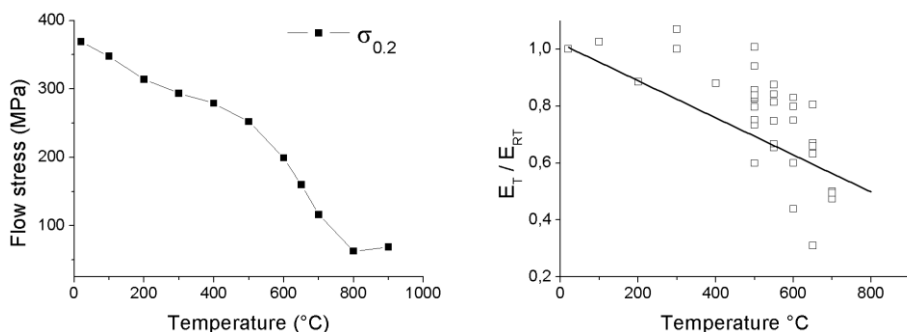
*Figure 3.6. **a)** Yield stress ($\sigma_{0.2}$) as a function of temperature, obtained from tensile tests with $\dot{\varepsilon}$ = 0.012 s^{-1}. **b)** E-modulus derived from tensile test (squares), with a linear fit.*

As it has been described before, the thermal hardening requires heating the sample to transform the ferrite into austenite, followed by air cooling to room temperature to induce a martensitic microstructure during cooling. In Fig. 3.7 the temperature evolution of the yield stress during the heating and cooling stage is provided again. Blue and green full dots were determined from compression experiments carried out at 0.01 s^{-1} in a Bähr DIL 805A/D plastodilatometer [45]. For these experiments small cylindrical samples of 5 mm in length and 3 mm in diameter machined along the rolling (RD) and transversal (TD) directions were heated at a rate of 4 °C/s to the testing temperature. A range of temperatures between 25 °C and 970 °C was tested during heating (light and dark blue full dots). The green full dots corresponds to experiments in which samples, with the same geometry, were heated at 4 °C/s to 970 °C, held for 10 minutes and cooled at a rate of 6 °C/s to the targeted testing temperature. The red full dots represent the yield stress obtained from the tensile test as presented in Fig. 3.6. For these tensile tests, bars of length 430 mm and width 20 mm were cut from a steel plate of 0.5 mm thickness. Indicated by arrows are the austenite start temperature A_s at 852 °C, the austenite finishing temperature A_f at 937 °C and the martensite start temperature M_s at 367 °C. This figure shows that during heating the yield stress decreases continuously down to the range of temperatures where the austenite forms. During cooling, once the M_s has been attained, the hard martensite phase which is now present in the microstructure, increases the yield stress of the steel significant, reaching a value of about ~1350 MPa at room temperature (TD sample), compared to yield stress obtained for the initial ferritic microstructure (~370 MPa for the TD sample). There is not a significant dispersion among the results obtained: i) using samples machined along the RD or TD; ii) using tensile or compression samples. Therefore the anisotropy is disregarded for the thermal cycle.
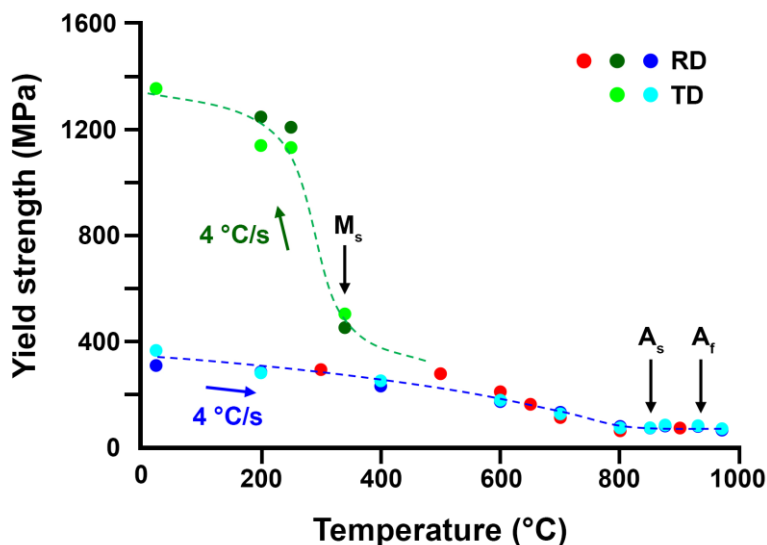
Figure 3.7. Temperature evolution of the yield stress during heating up to 1100 ˚C and cooling down to room temperature. Red full dots have been acquired from tensile tests, while the green and blue full dots correspond to compression tests performed in a plastodilatometer. Symbols RD and TD stand for the rolling and transversal directions. Symbols A_s and A_f stand for the start and end of the ferrite to austenite transformation during heating, while M_s stands for the start of the austenite to martensite phase transformation during cooling. The dashed lines have been drawn as a guide to the eye.

Fig. 3.8 shows the ferrite to austenite (for different heating rates), and austenite to martensite transformations derived form high resolution dilatometry experiments. The curves cannot be implemented into the material model directly, since the thermal expansion is also incorporated in the results. More importantly, as the ferrite to austenite (left plot of Fig. 3.8) is a diffusional transformation: the heating rate affects atom diffusion involved in the transformation. As the heating rate is increased, the transformation needs higher temperatures to activate the diffusion of the carbon atoms and the transformation shifts to higher temperatures as shown in these figures. Besides, the speed of the transformation might be also influenced by the heating rate. Therefore, a transformation rate description has to be used for this transformation. A (mathematical) Avrami equation is used to describe the fraction of a new phase. A simple empirical relation is used to integrate start and stop temperatures in this modified JMAK equation: the martensitic

transformation (right plot of Fig. 3.8), as described by Koistinen and Marburger [46]. The main intention of this work is to fit the experimental determined material behavior, in order to demonstrate the capability of this work flow for modelling on a product-sized level.

The relation proposed by Koistinen and Marburger is only temperature dependent and can only facilitate a dual phase transformation. However for the thermal treatment applied here, three phases can be present: ferrite, martensite and austenite. In order to avoid that in the calculation the material would transform back into ferrite instead of martensite, the curve is implemented with respect to temperature and phase.
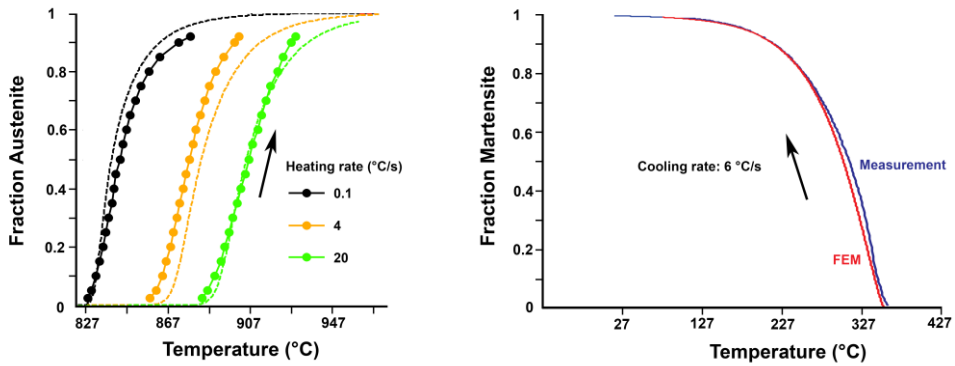
*Figure 3.8. Dilatometer tests showing: **Left)** the ferrite to austenite transformation, dots are measured values, the dashed lines represent the FE model; **Right)** the austenite to martensite transformation.*

The thermal expansion coefficient has been determined by dilatometry from the temperature dependent evolution of the relative change in length ($\Delta l / l_0$), as shown in Fig. 3.9. As for Fig. 3.8, these experiments have been carried out on planar samples, 12 mm in length, 4 mm in width and 0.7 mm in thickness using an Adamel Lhomargy DT1000 high resolution dilatometer. The heating and cooling rates have been 4 and 6 °C/s respectively.

During heating the sample expands linearly up to a temperature (A_s) where the ferrite starts transforming to austenite and the samples contracts; when the transformation has finished (A_f), the sample continues expanding linearly again. During cooling, the sample contracts linearly down to a temperature (M_s) where it starts transforming to martensite and an expansion is recorded. A linear expansion

coefficient of 10^{-6} K^{-1} and 1.9^{-5} K^{-1} has been experimentally measured for ferrite and austenite phases respectively. The thermal expansion of martensite is difficult to derive from Fig. 3.9, and therefore assumed being equal to the thermal expansion of ferrite.
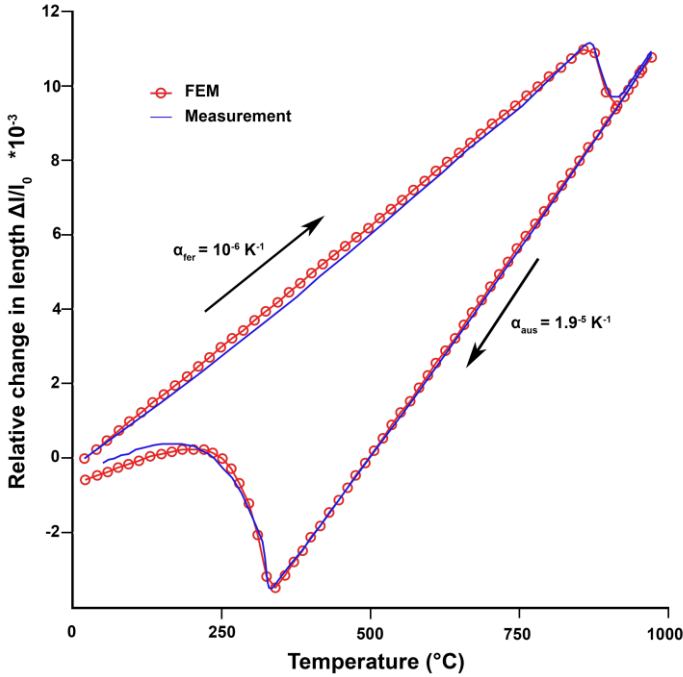
Figure 3.9. Temperature evolution of the relative change in length during heating at 4 °C/s up to 970 ˚C (10 minutes holding) and subsequent cooling at 6 °C/s. The dark blue solid line corresponds to the experimental behavior recorded by dilatometry, and the red circles reproduce the FE model.

3.3.2 Relaxation of residual stresses

Since creep forms an important phenomenon in our work a brief summary of the equation used in the following is given here. Strain rate due to creep in solid solutions is described as a diffusion controlled process [47–50] by:

$$\dot{\varepsilon}_{creep} = A\left(\frac{b}{d}\right)^p \left(\frac{\sigma - \sigma_0}{E(T)}\right)^n \ e^{\frac{-Q_C(T)}{RT}} \tag{3.2}$$

where b represents the magnitude of the Burgers vector, d is the grain size diameter, p represents the grain size exponent. Q_c represents the activation energy for self-

diffusion, in bulk or along grain-boundaries or along dislocation cores, depending on the actual operating mechanism. The external applied stress is σ and the threshold stress is σ_0.

Creep tests at 500 °C, 600 °C and 700 °C were done at constants load in the elastic regime. The response at 500 and 700 °C, at three different loads are shown in Fig. 3.10.
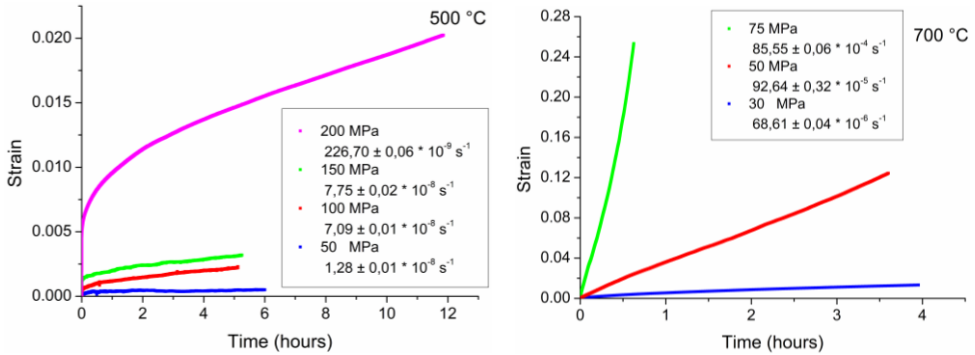
Figure 3.10. Time versus strain for constant loads at 500 °C (left) and 700 °C (right).

The steady state creep rates are displayed in Fig. 3.11 and show an increase over several orders of magnitude between 500-600 and 600-700 °C for a stress around 100 MPa. The stresses have been chosen to about a maximum of 75% of the yield stress (in the elastic zone) for every temperature. Therefore the temperature dependent flow stress determined in Fig. 3.6 acts as an upper limit. For higher stresses the creep regime changes from a power-law to exponential creep, whereby the steady state creep is a relative short state and tertiary creep is active.
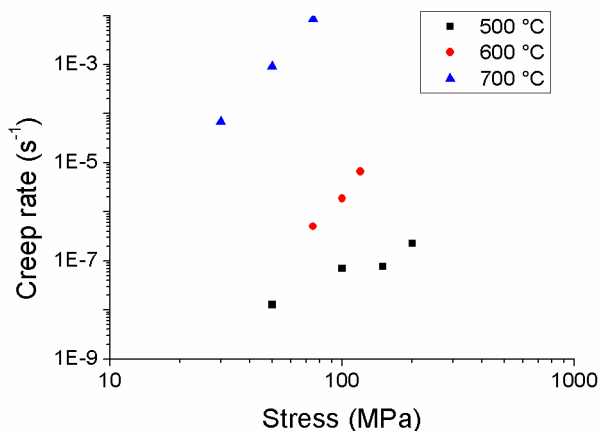
Figure 3.11. Secondary creep rate as a function of load at 500 °C (triangles), 600 °C (dots) and 700 °C (squares).

The slope of the double log plot yields the stress exponent *n* of 2.1, 5.4, 5.3 at 500, 600 and 700 °C, respectively. The creep stress exponent is an indication of the creep rate controlling mechanism. For *n* =3, viscous dislocation glide is rate controlling; for *n* = 4-6 dislocation creep is rate controlling through dislocation climb [51,52]. Likely both creep mechanisms are active simultaneously. Therefore, dislocation glide is the predominant mechanism between 500-600 °C and dislocation climb is the predominant phenomenon at 600-700 °C. For the threshold stress σ_0 in Eq. 3.2 a value of zero was derived.

Strain rates at different temperatures provide information about the activation energy for creep Q_c [49] and two creep regimes were found, i.e. Q_c is 57 ± 30 and 141 ± 2 kJ/mol for 500-600 °C and 600-700 °C, respectively. The latter value of Q_c is close to self-diffusion activation energy whereas the former points to carbon diffusional processes.

The microstructure was investigated in detail with electron back scatter diffraction (EBSD). A specimen from the strip of material (as-received) was heated 30 minutes at 700 °C prior to analysis. More than 1000 grains from each sample where measured, but no significant grain growth was observed compared to the as-received material. Therefore the term with the grain size exponent *p* reduces to a constant, and is merged with the material constant *A*. As the creep regimes shift drastically in the described temperature range, *A* had been given a small temperature dependence to ensure a better fit for the temperature range 500 - 700 °C.

The derived values are summarized in Table 3.1.

Table 3.1. Experimentally obtained values for the functional set of variables n, Q_c and A of the creep model (see Eq. 3.2.) in the temperature range 500-700 °C.

	500 °C	600 °C	700 °C	500-600 °C	600-700 °C
n	2.1.	5.4	5.3	-23+0.033*T(K)	-6.6-0.001*T(K)
Q_c				57 kJ/mol	141 kJ/mol
A				-123+0.16*T(K)	-12+0.008*T(K)

Finally, stress relaxation calculations based on this creep model are done using a FE bending test. The sample is heated to the temperature of interest and bended between two tilted dies until the desired stress (load) is reached in an element on the outside of the sample (inducing tensile stress). Thereafter the dies are fixed in their final positions and the temperature is kept constant. In every time step the creep strain due to the stress is evaluated resulting in a decrease of the stress. This test is repeated at different loads and at various temperatures (Table 3.2). Fig. 3.12 shows the resulting equivalent Von Mises stress together with the tensile tests. Here the specimen is deformed elastically due to a particular load, after which the stress relaxation is recorded by the load cell. The calculated stress relaxation is in good agreement with the tests: i.e. for the initial stage 0-10 seconds (rapid decrease) and the second stage where the stress level remains quasi-static. It demonstrates that the creep model is suitable to calculate stress relaxation below the austenitization temperature of 800 °C.

Table 3.2. Initial loads used for stress relaxation tests at different temperatures.

	500 °C	600 °C	700 °C
Initial load #1 (MPa)	210.	160	100
Initial load #2 (MPa)	160	120	75
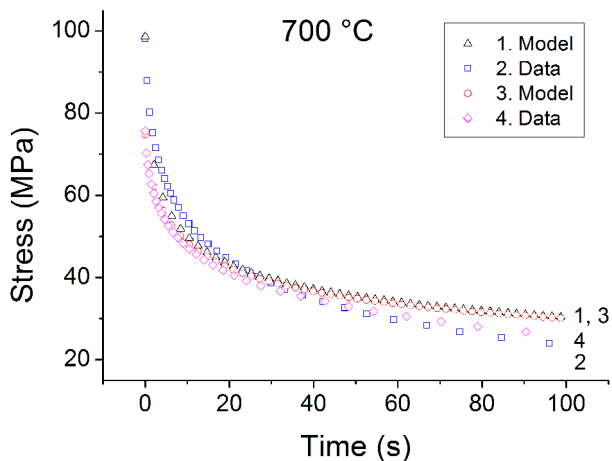
Figure 3.12. Stress relaxation tests with fixed strain, lines 2 (squares) & 4 (diamonds) for different initial load values; together with the calculated stress relaxation by creep of a bending test, lines 1 (triangles) & 3 (circles).

The creep model is implemented in the FE software and enables calculation of the evolution of the residual stresses and creep strains during a heat treatment. The residual stresses in the cup calculated by FE modelling of the forming process are shown in Fig. 3.13 left. This is the initial state before heat treatment. In the simulation of the heat treatment a linear temperature profile from 20 to 700 °C in 1000 seconds is applied. Due to the convergence of the constitutive equations, the calculation can be done in just 11 FE steps. The internal stress decreases significantly to nearly 0 MPa. Although the yield strength decreases with increasing temperature considerably (as shown in Fig. 3.6), the residual stresses remain in the elastic zone during the entire heat treatment. The relaxation by creep lowers the residual stress faster than the decrease of the yield strength as a function of temperature.

The resulting creep strains affect the bottom flatness and are therefore responsible for shape change during heating. It has been noticed that the shape change of a full hardened cup is equal to a cup heated to 700 °C. This observation is supported by the calculation results in Fig. 3.13 right, showing that almost all stresses have been relaxed after heating to 700 °C.
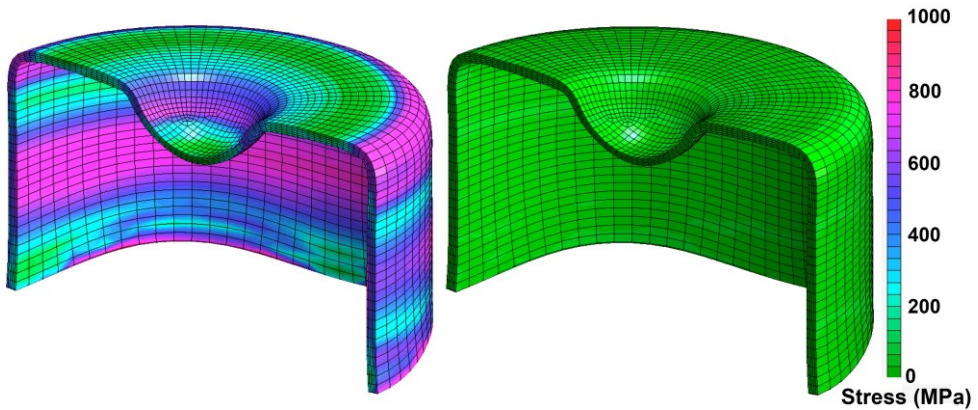
Figure 3.13. Cross-section of simulated cups with contour plots of the equivalent Von Mises stress. **Left)** *Local high stresses after forming,* **Right)** *relaxation of the stresses after heating to 700 °C.*

3.4 Product shape change

The shape of the cup was recorded at different stages in the process: after forming, during stress relaxation during annealing, and after thermal hardening. The critical geometric parameter for the shape change is the bottom flatness and defined as indicated in Fig. 3.14. The bottom flatness is defined as the angle between the side of the cup and the top, and measured by scanning the top with a Nanofocus μscan confocal microscope [53]. A radial measurement has been performed at points r = 9 mm (y_1) and r = 7 mm (y_2). The absolute difference between y_1 and y_2 then quantifies the bottom flatness of the cup. To point out the effect of the thermal cycle on the shape change, the flatness after forming was taken as a reference. The shape change Δ is therefore expressed as $\Delta = (y_1 - y_2)_{forming} - (y_1 - y_2)_{hardening}$. The measured values of y show angular variations caused by the anisotropy in the material. The final value of y is the average over the circumference To be able to make a statistical comparison and distinguish between reproducible shape defects and distortions, the experiment was repeated for a set of 50 specimens.
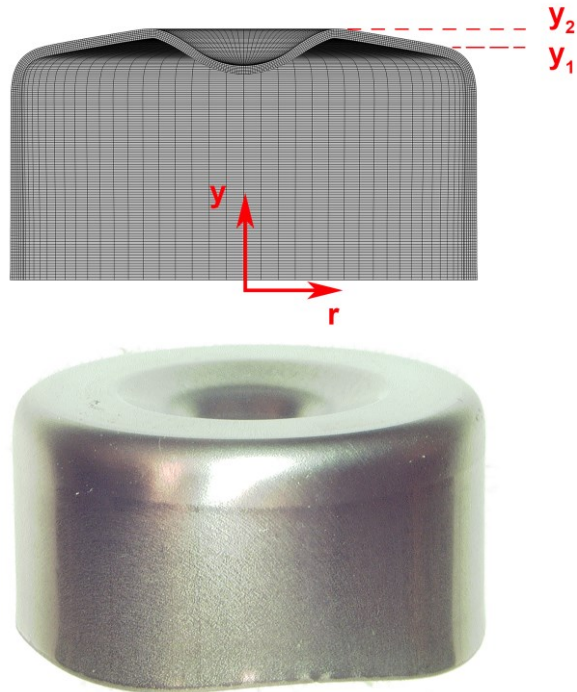
Figure 3.14. Real fabricated cup (bottom) and its cross section with points y_1 and y_2. The absolute difference between y_1 and y_2 defines the bottom flatness of the cup

The initial calculation of the forming of the cup (see Section 3.1) was subjected to a heat treatment up to 970 °C. The various implementations for heating, were used to calculate the strains caused by: cold forming, creep, thermal expansion and phase transformation. These calculated strains are displayed in Fig. 3.15 for different stages of the thermal treatment: elastic strain after cold forming; thermal strain after heating to 970 °C with a temperature difference over the cup of 1 °C; total creep strain after the full thermal cycle (heating and cooling).
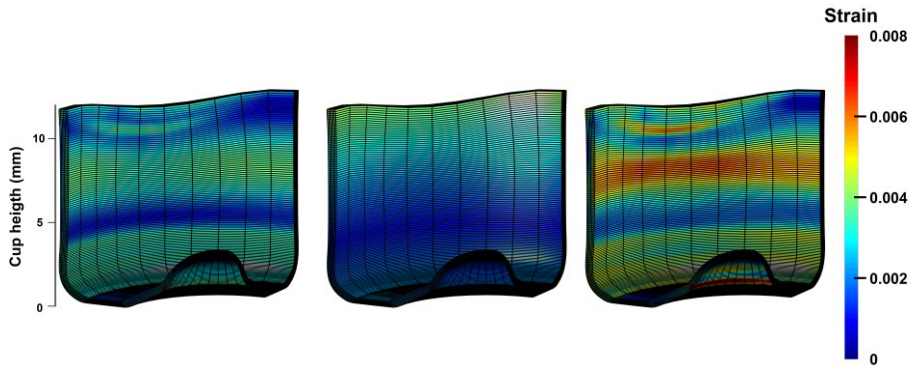
Figure 3.15. Example of a FE calculation of the strain distribution in a cold-formed cup at different stages of the thermal treatment. **Left)** *elastic strain after cold forming;* **Center)** *thermal strain after heating to 970 °C with a temperature difference of 1 °C between the top and bottom of the cup;* **Right)** *total creep strain after the full thermal cycle (heating and cooling).*

From the calculations it is observed that:
- Residual stresses have been relaxed due to creep strains before the austenite start temperature (A_s).
- Thermal strains are relatively small, but not homogeneously spread due to an applied thermal gradient.

The critical parameter used to characterized the shape of the cup, the bottom flatness, can be extracted from the calculations as a function of temperature. The results are compared to the experimentally measured shape changes due to the heat treatment (Fig. 3.16). The shape after forming is taken as the reference values and set to zero (dotted line in Fig. 3.16). The test samples have to be at room temperature before the shape change can be determined by confocal microscopy. This implies that the samples heated to 970 °C, which is above the austenite start temperature, are actually transformed to martensite during the (air) cooling to room temperature after this temperature has been reached.

FE calculations have been subjected to the same temperature profile and contain therefore also the austenite to martensite phase transformation. In Fig. 3.16 can be seen that the bottom flatness decreases as the temperature increases. Up to 300 °C the shape change is the result of plastic deformation due to the decrease of the flow stress with increasing temperature. The majority of the shape change is gained in the following temperature region up to the temperature at which the phase

transformation starts (A_s=852 °C). Here the residual stresses induce the largest strain due to creep processes, which is also seen in Fig. 3.16. The modeling of the shape change is in good agreement with the experimental values as the same trend is observed in both cases with increasing temperature. The calculations provide a final shape change of 6 micrometer, and 5.0 ± 0.8 micrometer for the experimentally measured cups. The shape change of the batches of experimental measured cups is depicted as a box plot [54] in order to visualize the spread of the batch values on top of the average value.
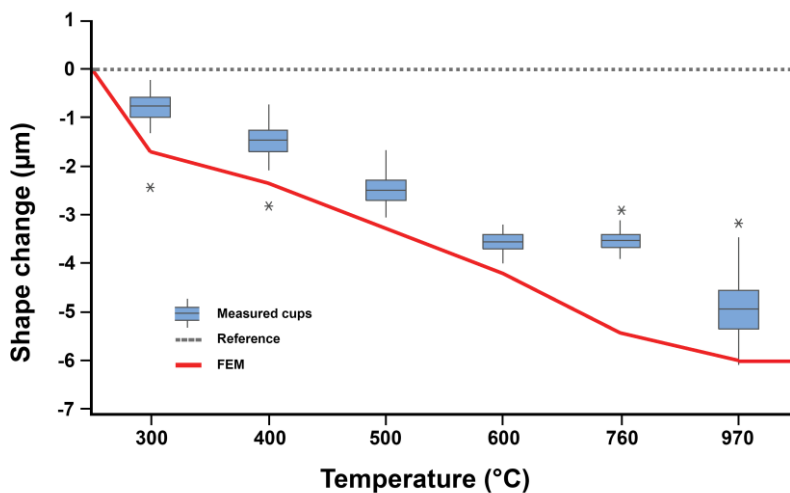
Figure 3.16. Cup shape change after heating as predicted by the FEM modelling (solid red line) compared to experimentally measured values (blue box plots). All samples (experimental and calculated) have been cooled down to room temperature before the shape change has been determined. Samples heated to 970 °C have therefore been transformed to martensite. The shape change after forming.is taken as a reference value and indicated by the dotted line. The experimental measured values obtained from 46 cups are represented by the box plots. Outliers are indicated by asterisks.

The novel contribution of this work is the successful coupling of a forming and a hardening calculation, in which several material subroutines are called at the same time. Not only has the material behavior been implemented and modeled, but also validated for both the forming and thermal hardening. Thanks to the integrated modeling of both the forming and the hardening, the effect of the metal forming on the shape change after heat treatment can now be calculated directly. A unique

insight in the interactions between the material phenomena and the residual stresses caused by the forming is now created. We now have the special opportunity to investigate the relative impact of individual parameters on the shape change. The design of the work-flow can be investigated and adjusted, without the necessity of installing a new production setup and performing time consuming experiments. To this end, various parameter changes have been explored, such as:

- amount of material flattening during cold forming;
- the temperature gradient on the product during the heat treatment;
- the heating rate;
- the amount of FE calculation steps;
- deviation of the experimental determined E-modulus;
- deviation of the creep rate.

These calculations are performed in 2D, as opposed to the 3D calculations shown here, to limit the required calculation time. The effect of these parameter changes on the calculated shape change is listed in Table 3.3. The metal forming shows a strong influence on the calculation. Less flattening results in less shape change after the heat treatment.

The flattening of the metal influences the stiffness of the product; more (plastic) deformation can take place when flattening is increased. This alters the residual stress state after forming, which will cause higher creep strains during the thermal treatment. A temperature gradient can be present in the cup, due to experimental conditions such as furnace design and product throughput. The reference calculation is in good agreement with the experimental results where a temperature difference of 1°C between the top and bottom of the cup is assumed. The calculations with adjusted thermal gradients (none and 10 °C) show a large deviation in shape change and indicate that the thermal gradient is an important parameter in the fabrication process and therefore on the final product quality.

The implementation of the temperature dependent E-modulus assumes a linear temperature dependence up to 800 °C. For temperatures higher than 800 °C no data is available from the experimental technique, as the drop in the yield stress and creep effects cause flowing behavior even for low applied stresses. The elastic module is therefore assumed to remain constant above 800 °C. A deviation of the E - modulus of 10%, seems to have a minor influence on the shape change calculation, as seen in Table 3.3. Another underlying assumption is that process of relaxation of the residual stresses by creep is faster than the drop of the yield stress due to increasing temperature. The creep rate is also taken as constant from 800 °C

towards the phase transformation. The influence of this assumption seems not to be of impact on the results, as the calculations with this model show that the residual stresses are already relaxed when a temperature of 700 °C is reached (see Fig. 3.15). The calculation with a 10% lower creep rate at every temperature below the transformation point, does not even show an effect on the calculated shape change.

An increase of the amound of calculation steps, also has a small influence on the calculated shape change. This indicates that the model is robust with a relatively big time step of 200 increments per load case. This is an important parameter with respect to checking the quality of the FE analysis

Table 3.3. Effect of adjusted input parameter on the calculated shape change.

Parameter	Adjustment in FEM model	Shape change during heat treatment (%)
Flattening	Lower reduction of material thickness: 30% to 20%	-62.5
Heating rate	Reduced heating rate: 10 °C/s to 1 ˚C/s	-12.5
Temp. diff. over cup	Decreased temp. difference: 1 ˚C to 0˚C	100
Temp. diff. over cup	Increased temp. difference: 1 °C to 10 °C	300
# of calc. steps	Increase of increments: 200 to 1000	8
E-module	10% lower	8
Creep rate	10% lower	0

3.5 Conclusions

The processing steps of the forming and a thermal treatment have been successfully implemented in FE. Cold forming by deep drawing is calculated whereby planar anisotropy is implemented. The distribution and magnitude of the residual stresses was successfully predicted in comparison with the micro hardness profile of a fabricated cup.

The important thermal hardening treatment consists of three contributions: creep, thermal expansion and phase transformation. Two creep regimes were

experimentally identified in the heating trajectory to 700 °C. The relaxation by creep lowers the residual stresses faster than the decrease of the yield stress by temperature. Dilatometer tests have been performed to measure the thermal expansion and phase transformation as a function of temperature and heating rate. An important message is that, in contrast to what is commonly believed, residual stresses play a crucial role during creep and that the shape change occurs at lower temperatures, i.e. not at higher temperatures and in fact well below the transformation temperature.

Following the new FEM approach, the data could be implemented either directly, or after a simple fit, into the material model. With this simplified but robust model, the complete forming and heat treatment of a cup have been successfully calculated. The defined shape change of this cup was compared to experimental measured shape change at various temperatures, and showed good agreement.

It has been demonstrated that through modeling a successful coupling between forming and thermal treatment could be made. Measurement and model show that the individual material phenomena can clearly be distinguished in the products during observation as well as the FE model.

Preliminary investigations of critical parameters indicate that metal forming (flattening) and a temperature gradient have a significant impact on the final shape change, and can both positively and negatively influence the product quality. Usually the thermal treatment in the fabrication process is difficult to adjust, due to a fixed production setup. Therefore the brief investigation with the FE model is laboriously and costly to validate with a quick series of experiments. However it can be helpful in optimizing the temperature profile and play an important role when a new furnace has to be installed, with a full understanding of the effects of stress and stain during hardening, hereby reducing time and costly experiments.

With this model the effect of a new tooling design or an adjustment on the current design can now be predicted, but also the following interaction with the thermal treatment. This coupling is key in the design and the novel demonstration of this work.

Ultimately this investigation can and will increase the predictability and accuracy of the process chain.

3.6 References

[1]   R. Husson, J.Y. Dantan, C. Baudouin, S. Silvani, T. Schreer, R. Bigot, Evaluation of process causes and influences of residual stress on gear distortion, CIRP Ann. - Manuf. Technol. 61 (2012) 551–554. doi:10.1016/j.cirp.2012.03.106.

[2]   C.M. Amey, H. Huang, P.E.J. Rivera-Díaz-del-Castillo, Distortion in 100Cr6 and nanostructured bainite, Mater. Des. 35 (2012) 66–71. doi:10.1016/j.matdes.2011.10.008.

[3]   R. Husson, C. Baudouin, R. Bigot, E. Sura, Consideration of residual stress and geometry during heat treatment to decrease shaft bending, Int. J. Adv. Manuf. Technol. 72 (2014) 1455–1463. doi:10.1007/s00170-014-5688-8.

[4]   ASM International, ASM Handbook Volume 04 - Heat Treating, 1991.

[5]   P.J. Withers, Residual stress and its role in failure, Reports Prog. Phys. 70 (2007) 2211–2264. doi:10.1088/0034-4885/70/12/R04.

[6]   M.R. James, Relaxation of Residual Stresses an Overview, Adv. Surf. Treat. (Ed. A. Niku-Lari). 4 (1987) 349–365.

[7]   P.J. Withers, H.K.D.H. Bhadeshia, Residual stress. Part 1 – Measurement techniques, Mater. Sci. Technol. 17 (2001) 355–365. doi:10.1179/026708301101509980.

[8]   P.J. Withers, H.K.D.H. Bhadeshia, Residual stress. Part 2 – Nature and origins, Mater. Sci. Technol. 17 (2001) 366–375. doi:10.1179/026708301101510087.

[9]   D. Peral, C. Correa, M. Diaz, J.A. Porro, J. de Vicente, J.L. Ocaña, Measured strains correction for eccentric holes in the determination of non-uniform residual stresses by the hole drilling strain gauge method, Mater. Des. 132 (2017) 302–313. doi:10.1016/J.MATDES.2017.06.051.

[10]   N.S. Rossini, M. Dassisti, K.Y. Benyounis, A.G. Olabi, Methods of measuring residual stresses in components, Mater. Des. 35 (2012) 572–588. doi:10.1016/J.MATDES.2011.08.022.

[11]   C. Mansilla, D. Martínez-Martínez, V. Ocelík, J.T.M. De Hosson, On the determination of local residual stress gradients by the slit milling method, J. Mater. Sci. 50 (2015) 3646–3655. doi:10.1007/s10853-015-8927-y.

[12]   I. Basu, H. Fidder, V. Ocelík, J. Th.M de Hosson, Local Stress States and Microstructural Damage Response Associated with Deformation Twins in Hexagonal Close Packed Metals, Crystals. 8 (2018) 1–15. doi:10.3390/cryst8010001.

[13]   J. Ahn, E. He, L. Chen, R.C. Wimpory, J.P. Dear, C.M. Davies, Prediction and measurement of residual stresses and distortions in fibre laser welded Ti-6Al-4V considering phase transformation, Mater. Des. 115 (2017) 441–457. doi:10.1016/J.MATDES.2016.11.078.

[14]   K. Hemmesi, M. Farajian, M. Boin, Numerical studies of welding residual

stresses in tubular joints and experimental validations by means of x-ray and neutron diffraction analysis, Mater. Des. 126 (2017) 339–350. doi:10.1016/J.MATDES.2017.03.088.

[15]   Z. Wang, E. Denlinger, P. Michaleris, A.D. Stoica, D. Ma, A.M. Beese, Residual stress mapping in Inconel 625 fabricated through additive manufacturing: Method for neutron diffraction measurements to validate thermomechanical model predictions, Mater. Des. 113 (2017) 169–177. doi:10.1016/J.MATDES.2016.10.003.

[16]   G. Vastola, G. Zhang, Q.X. Pei, Y.-W. Zhang, Controlling of residual stress in additive manufacturing of Ti6Al4V by finite element modeling, Addit. Manuf. 12 (2016) 231–239. doi:10.1016/J.ADDMA.2016.05.010.

[17]   F. Foadian, A. Carradó, T. Pirling, H. Palkowski, Residual stresses evolution in Cu tubes, cold drawn with tilted dies – Neutron diffraction measurements and finite element simulation, Mater. Des. 107 (2016) 163– 170. doi:10.1016/J.MATDES.2016.06.028.

[18]   S. Denis, E. Gautier, A. Simon, G. Beck, Stress – phase-transformation interactions – basic principles, modelling, and calculation of internal stresses, Mater. Sci. Technol. 1 (1985) 805–814. doi:10.1179/026708385790124071.

[19]   L. Huiping, Z. Guoqun, N. Shanting, H. Chuanzhen, FEM simulation of quenching process and experimental verification of simulation results, Mater. Sci. Eng. A. 453 (2007) 705–714. doi:10.1016/j.msea.2006.11.023.

[20]   C. Simsir, C.H. Gur, 3D FEM simulation of steel quenching and investigation of the effect of asymmetric geometry on residual stress distribution, J. Mater. Process. Tech. 207 (2008) 211–221. doi:10.1016/j.jmatprotec.2007.12.074.

[21]   S.C. Polytechnic, The Effect of Stress Relaxation Rate on the Generation of Thermal Stress During Quenching, 82 (1986) 101–115.

[22]   M.C. Somani, L.P. Karjalainen, M. Eriksson, M. Oldenburg, Dimensional Changes and Microstructural Evolution in a B-bearing Steel in the Simulated Forming and Quenching Process, ISIJ Int. 41 (2001) 361–367.

[23]   S. Lee, Y. Lee, Finite element simulation of quench distortion in a low-alloy steel incorporating transformation kinetics, Acta Mater. 56 (2008) 1482–1490. doi:10.1016/j.actamat.2007.11.039.

[24]   H. Surm, O. Kessler, F. Hoffmann, H.W. Zoch, Manufacturing Residual Stress States in Heat Treatment Simulation of Bearing Rings, Mat. -Wiss. u. Werkstofftech. 37 (2006). doi:10.1002/mawe.200500973.

[25]   S. Hossain, C.E. Truman, D.J. Smith, R.L. Peng, U. Stuhr, A study of the generation and creep relaxation of triaxial residual stresses in stainless steel, Int. J. Solids Struct. 44 (2007) 3004–3020. doi:10.1016/j.ijsolstr.2006.09.001.

[26]   Z. Zhou, A.S. Gill, A. Telang, S.R. Mannava, K. Langer, V.K. Vasudevan, D. Qian, Experimental and Finite Element Simulation Study of Thermal

    Relaxation of Residual Stresses in Laser Shock Peened IN718 SPF
    Superalloy, Exp. Mech. 54 (2014) 1597–1611. doi:10.1007/s11340-014-9940-9.

[27]   M. Hunkel, Anisotropic transformation strain and transformation
        plasticity : two corresponding effects, Mat. -Wiss. u. Werkstofftech. 40
        (2009). doi:10.1002/mawe.200900478.

[28]   M. Wolff, M. Böhm, S. Bökenheide, D. Lammers, T. Linke, An implicit
        algorithm to verify creep and TRIP behavior of steel using uniaxial
        experiments, J. Appl. Math. Mech. 379 (2012) 355–379.
        doi:10.1002/zamm.201100083.

[29]   T. Gnaeupel-Herold, H.J. Prask, R.J. Fields, T.J. Foecke, Z.C. Xia, U.
        Lienert, A synchrotron study of residual stresses in a Al6022 deep drawn
        cup, Mater. Sci. Eng. A. 366 (2004) 104–113.
        doi:10.1016/j.msea.2003.08.059.

[30]   V.M. Radhakrishnan, C.R. Prasad, Relaxation of residual stress with
        fatigue loading, Eng. Fract. Mech. 8 (1976) 593–597. doi:10.1016/0013-7944(76)90033-3.

[31]   J. Frankel, A. Abbate, W. Scholz, The effect of residual stresses on
        hardness measurements, Exp. Mech. 33 (1993) 164–168.
        doi:10.1007/BF02322494.

[32]   V.P. Romanovski, Handbook of Cold Stamping, Machinery-Building,
        Moscow, 1979.

[33]   Y. Estrin, H. Mecking, A unified phenomenological description of work
        hardening and creep based on one-parameter models, Acta Metall. 32
        (1984) 57–70. doi:10.1016/0001-6160(84)90202-5.

[34]   J. Post, C. de Vries, J. Huétink, Validation tool for 2D multi-stage metal-
        forming processes on meta-stable stainless steels, J. Mater. Process.
        Technol. 209 (2009) 5558–5572. doi:10.1016/j.jmatprotec.2009.05.020.

[35]   W.T. Lankford, S.C. Snyder, J. Bausher, New criteria for predicting the
        press performance of deep drawing sheets, Trans. ASM. 42 (1950) 1197–1205.

[36]   R. Hill, A Theory of the Yielding and Plastic Flow of Anisotropic Metals,
        Proc. R. Soc. Lond. A. Math. Phys. Sci. 193 (1948) 281–297.
        doi:10.1098/rspa.1948.0045.

[37]   Marc 2016: Computational Procedures for Elastic-Plastics Analysis,
        Volume A: (2016).

[38]   Y. Estrin, Dislocation-Density–Related Constitutive Modeling in: Unified
        constitutive laws of plastic deformation - Eds. A.S. Krausz, K. Krausz, 1
        (1996) 69–106.

[39]   J.H. Lee, M. Mahendran, P. Makelainen, Prediction of mechanical
        properties of light gauge steels at elevated temperatures, J. Constr. Steel
        Res. 59 (2003) 1517–1532. doi:10.1016/S0143-974X(03)00087-7.

[40]   H.M. Ledbetter, R.P. Reed, Elastic Properties of Metals and Alloys, I.

Iron, Nickel, and Iron-Nickel Alloys, J. Phys. Chem. Ref. Data. 2 (1973) 531–618. doi:10.1063/1.3253127.

[41]   M. Fukuhara, A. Sanpei, Elastic moduli and internal friction of low carbon and stainless steels as a function of temperature, ISIJ Int. 33 (1993) 508–512.

[42]   J. Chen, B. Young, Corner properties of cold-formed steel sections at elevated temperatures, Thin-Walled Struct. 44 (2006) 216–223. doi:10.1016/j.tws.2006.01.004.

[43]   J. Chen, B. Young, Experimental investigation of cold-formed steel material at elevated temperatures, Thin-Walled Struct. 45 (2007) 96–110. doi:10.1016/j.tws.2006.11.003.

[44]   H. Masumoto, S. Sawaya, M. Kikuchi, Thermal Expansion Young' s and Temperature Modulus in Fe-Cr Dependence Alloys, Trans. J I M. 12 (1971) 18–21.

[45]   TA Instruments - DIL 805A/D. http://www.tainstruments.com/dil-805ad/.

[46]   D.P. Koistinen, R.E. Marburger, A general equation prescribing the extent of the austenite-martensite transformation in pure iron-carbon alloys and plain carbon steels, Acta Metall. 7 (1959) 59–60.

[47]   J. Weertman, Steady-State Creep through Dislocation Climb, J. Appl. Phys. 28 (1957) 362. doi:10.1063/1.1722747.

[48]   J. Weertman, Steady-state creep of crystals, J. Appl. Phys. 28 (1957) 1185–1189. doi:10.1063/1.1722604.

[49]   O.D. Barret, C.R., Ardell, A.J., Sherby, Influence of Modulus on Temperature Dependence of Activation Energy for Creep at High Temperatures, Trans. Metall. Soc. AIME. 20 (1964) 200.

[50]   O.D. Sherby, P.M. Burke, Mechanical behavior of crystalline solids at elevated temperature, Prog. Mater. Sci. 13 (1968) 323–390. doi:10.1016/0079-6425(68)90024-8.

[51]   O.D. Sherby, E.M. Taleff, Influence of grain size, solute atoms and second-phase particles on creep behavior of polycrystalline solids, Mater. Sci. Eng. A. 322 (2002) 89–99. doi:10.1016/S0921-5093(01)01121-2.

[52]   S. V. Raj, S.C. Farmer, Characteristics of a new creep regime in polycrystalline NiAl, Metall. Mater. Trans. A. 26 (1995) 343–356. doi:10.1007/BF02664671.

[53]   Nanofocus - μscan select. http://www.nanofocus.com/products/uscan/uscan-select/.

[54]   J.W. Tukey, Exploratory Data Analysis, 1977. doi:10.1007/978-1-4419-7976-6.

Chapter 4

Structure and evolution of steel oxide layers

In this Chapter we concentrate on the influence of the different crystal orientations of a polycrystalline stainless steel substrate and on the formation of the oxide layer. The work aims at investigating whether the substrate orientation has a predominant influence on the composition and thickness of the oxide layer.

4.1 Introduction

Bare metal surfaces have a tendency to form a thin oxide film on the metal-gas interface. Cabrera and Mott [1] describe that the growth of this film is driven by a potential field across the layer. The initial growth is very rapid, but it slows down when the electrons transfer is more and more hampered by the increasing oxide layer thickness. When electron and ion transport is diminished, the growth of the film ends. The resulting passive layer is generally between 2 – 10 nm [1].

Upon heating, the equilibrium of the passive film is disrupted. The passive film thickens until a thermal oxide layer is formed which acts now as a barrier for further corrosion.

The formation of oxides has been studied extensively on iron, as it is a base metal in many (structural) alloys. Pure iron is not used in structural or industrial applications because of the low mechanical strength and corrosion resistance. The oxidation of iron is very well described by Vernon [2,3]. When iron is heated above 200 ºC in air, a duplex oxide layer will form. The inner oxide consists of Fe_3O_4, also known as magnetite, the outer of Fe_2O_3 (hematite). For an extensive

background on iron oxides as Fe_2O_3 and Fe_3O_4 reference is made to the reviews in [4,5].

The positive influence of chromium on the retardation of oxidation of iron has been noticed for almost two centuries. Research on this topic was initiated and driven by the pioneering work of Michael Faraday, James Stodart and Pierre Bertier [6–8], starting in 1820. Nowadays, it is well known that the protective passive layer on Fe-Cr steel consists of a mixed film of iron- and chromium oxides such as $(Fe,Cr)_2O_3$ and $(Fe,Cr)_3O_4$ [9], with a thickness of the order of several nanometers [10–12]. The formation of these oxides depends critically on the conditions such as oxygen pressure and temperature. Studies involving the particular oxide growth along the three main directions, i.e. <100>, <110>, <111>, focus on e.g. iron [13,14], chromium [15–18] or Fe-Cr [19,20] single crystals, often under well-controlled laboratory conditions with precise amounts of oxygen at low pressure. The phase transformation between Fe_2O_3 and Fe_3O_4 has also been considered on deposited nano-layers [21,22].

These systems reported in literature on single crystals however may not apply for polycrystalline alloys, such as steel used in civil engineering. Moreover, oxidation during daily use often takes place in ambient conditions, as opposed to laboratory conditions with very low oxygen pressure. The bulk corrosion resistance of industrial used ferritic-martensitic (iron-chromium) steel depends critically on applied thermal treatments such as hardening and tempering, which promote either the dissolution or growth of chromium carbides [23–25]. The microstructure of the oxide layer on Fe-Cr steel as subjected to severe corrosion conditions was reported, e.g. the oxidation of steel under steam pipe conditions in wet and dry air at 600 ℃ of ferritic Fe-Cr and austenitic Fe-Cr-Ni 304L steel [26–28], and both types at a high temperature of 1000 ℃ [29]. The failure mechanism of a Fe-Cr-Ni steel at 700 ℃ in steam is presented in [30]. As the scale structure, growth, no special attention was paid to the bulk grain orientation. The thickness of the oxide scales varied from 0.1 – 100 μm. Only one singular study focused on the orientation of oxides found on polycrystalline Fe-Cr steel, with respect to the substrate [31]. Due to the high temperatures of 650 - 800 ℃ and a Cr content of 22%, mainly Cr-oxides were found. Scant work on pure polycrystalline iron revealed that after several hours oxidizing at 450 ℃ in air, mainly μm-thick magnetite-hematite duplex layers evolve, independent of the substrate microstructure [32]. In a recent interesting study by Takabatake et al. [33], polycrystalline iron with grains of several hundreds of micrometers was heated for one hour at 300 ℃ in air. The resulting oxide film

had a thickness of about 150 nm, and was investigated with Raman spectroscopy and ellipsometry. It was found that the $Fe_3O_4 : Fe_2O_3$ ratio varied for different crystal orientations: the proportion of Fe_3O_4 in the oxide is in the order of {100} > {111} > {101}.

Electrochemical tests indicate that for pure iron, the passive film formed at the same conditions on {110} surface is thinner than on {100} surface [34]. When we consider anodic dissolution of iron, the majority of cases show that the [100]-oriented crystal faces exhibit the fastest rate of metal removal after electro-polishing or chemical polishing. The metal removal from the faces {101} and {111} seems to be similar in most cases [35]. Another study on polycrystalline iron was not conclusive: in one case the corrosion current increased for different crystal planes in the order {101} < {111} < {100} for single grains, while in another study a dissolution rate of {100} < {111} ~ {101} was obtained [36].

Galvanostatic reduction of an oxidized iron surface in a borate solution with pH 8.4, suggests that {001} grains, which posses a thicker Fe_3O_4 layer compared to the other present crystal orientations, are more susceptible to reduction of the oxide layer [33]. Micro-cappilary cell measurements showed that the charge resistance and the donor density each depended on the substrate orientiation, but no clear correlation towards each other was found [37].

One can conclude that the studies on the substrate orientation dependent oxidation of iron, intended to derive the oxidation mechanism for a relative simple metallic system, show that the passivity is caused by complex (and not fully understood) factors. The branch of FeCr alloys is less developed and may be regarded as still be in its infancy. In particular the initiation of corrosion in the early stages has still to be understood for ferritic-martensitic stainless steel with an amount of 13% Cr. Therefore this work focusses on exposure in air for low temperatures, up to 450 ℃. The resulting thin oxide film with a thickness below 100 nm demands a non-trivial approach, as study by cross-section is only (local) achievable by transmission electron microscopy. A combination of optical- and scanning electron microscopy, X-ray photoelectron spectroscopy (XPS) and X-ray Diffraction (XRD) is used to characterize the oxide film.

4.2 Optical appearance of tempered steel surfaces

Thin oxide films were acquired in the following way. Specimens were cut from a strip of AISI 420 stainless steel and mirror polished, where the final step included polishing with 0.25 micrometer diamond particles. Colloidal water-based silica particle suspension was not used to avoid chemical etching. Exposure to water was also prevented by making use of an alcohol-type lubricant during polishing with diamond particles. After polishing, the specimens were rinsed with ethanol and dried in hot air. Recovery of the passive layer was executed in ambient conditions, i.e. at room temperature and 50 % Relative Humidity, for at least 24 hrs.

The corrosion films were established by oxidizing the mirror polished and recovered surfaces in air. The specimens were put in a quartz tube with openings at both ends and were introduced into a heat induction furnace (ThermoFisher). Temperature was measured with a thermocouple placed inside the quartz tube, and kept constant within ±5℃. Oxide layers were grown by a series of heat treatments. The applied temperatures are typical used at annealing for stress relieve, and well above the 200 ℃ to stimulate Fe diffusion to the surface [3]. First, the specimen was kept at 260℃ for 20 minutes. Thereafter the specimen was brought subsequently to 300, 350, 400 and 450℃, with a dwell time of 20 minutes at each temperature (see Table 4.1). After each oxidation step the specimen was taken out of the furnace for observation with the optical microscope. The area of interest, prior indexed by EBSD, was investigated with an Olympus VANOX-T optical microscope, making use of hardness indentations as markers.

Table 4.1. Heat treatment of the different samples used for the comparison of relative oxide thickness and crystal orientation.

Oxidation step	Heat treatment
1	260 °C for 20 minutes
2	After step 1 + 300 °C for 20 minutes
3	After step 2 + 350 °C for 20 minutes
4	After step 3 + 400 °C for 20 minutes
5	After step 4 + 450 °C for 20 minutes

A palette of various colours can be obtained at the surface due to the thermal treatments. For illustration: Fig. 4.1 shows the surface of a (non polished) piece of

the strip which was subjected to a different heat treatment such that a thermal gradient was established over the sample. The right side (blue) experienced the highest temperature. The various colours originates from the oxide layer by thin film interference, where the thickness of the layer controls the interference at certain wavelengths. The thickness of the oxide layer depends on the oxidation temperature and exposure time [2,38,39]. The order from thin to thicker oxide layers is: straw yellow, brown yellow, rosy mauve, blue [38]. An oxide thickness of 35 nm (straw yellow) and 59 nm (blue) has been obtained for iron by [2], and 46 & 72 nm for straw & blue by [40]. This general colour scheme/order can also be recognized in Fig. 4.1.
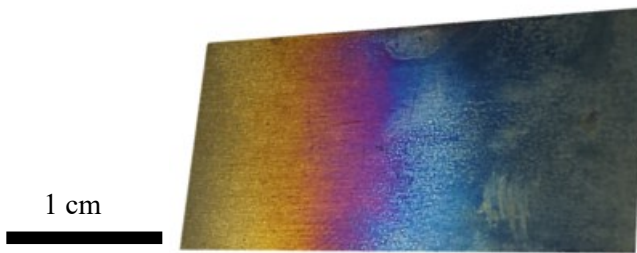
Figure 4.1. Various temper colours due to increasing oxide thickness, established with a temperature gradient. Right side (blue) experienced the highest temperature.

4.3 Grain orientation dependent temper colours

The crystal orientation of the stainless steel substrate was detected by an electron back scatter diffraction (EBSD) system within a Field Emission Gun (FEG) Environmental Scanning Electron Microscope (ESEM). By adding markers in the area of interest through micro-indentations, the same area prior and after the recovery of the passive layer was analyzed. Both the polished and recovered surfaces were still suitable for EBSD examinations. The area of interest has a size of 250 x 200 μm^2 and was scanned in a hexagonal grid with a step size of 0.4 μm, using an acceleration voltage of 30 kV. EBSD data were analysed by using the TSL OIM Analysis 7.3 software. Grain boundaries were defined for a misorientation angle larger than 5°.

Figure 4.2. Two s*equences (area I & II) of local change in colour due to oxidation. Each sequence shows* ***(a)*** *a [001] inverse pole figure map and the light microscopy image of the same area after heating at* ***(b)*** *260 °C;* ***(c)*** *260, 300 °C;* ***(d)*** *260, 300, 350 °C;* ***(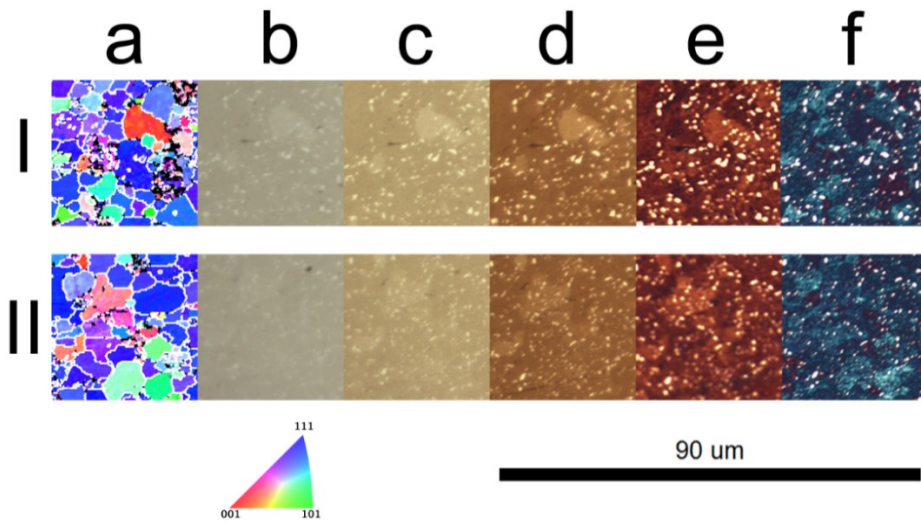e)*** *260, 300, 350, 400 °C and* ***(f)*** *260, 300, 350, 400, 450 °C, for 20 minutes at each temperature (also described in Table 4.1).*

Several distinct colours are observed at the surface due to the thermal treatments (see Table 4.1), as shown in Fig. 4.2. Within each image, local colour differences are noticed: the general coloured surface is decorated with small areas with a deviating colour. The particular areas remain deviating in colour throughout the tempering colour scheme. The deviating areas are attributed to a thinner oxide layer compared to the remaining surface. The difference is estimated to be of the order of several nm. The surface colour can be a combination of oxide thickness and surface morphology. Differences in surface structures as in [31] were not seen. Large sized nodules up to almost 1 μm as in [39] were not found either. Small spheres of about 100 nm, however, cover the surface. In any case, the deviating areas are lacking behind in the corrosion scheme compared to the rest of the surface.

When these areas are compared to the [001] inverse pole figure (IPF) map on the crystal plane parallel to the specimen surface, it is noticed that they correspond to particular crystal planes parallel to the surface. On a local level this is observed very clearly.
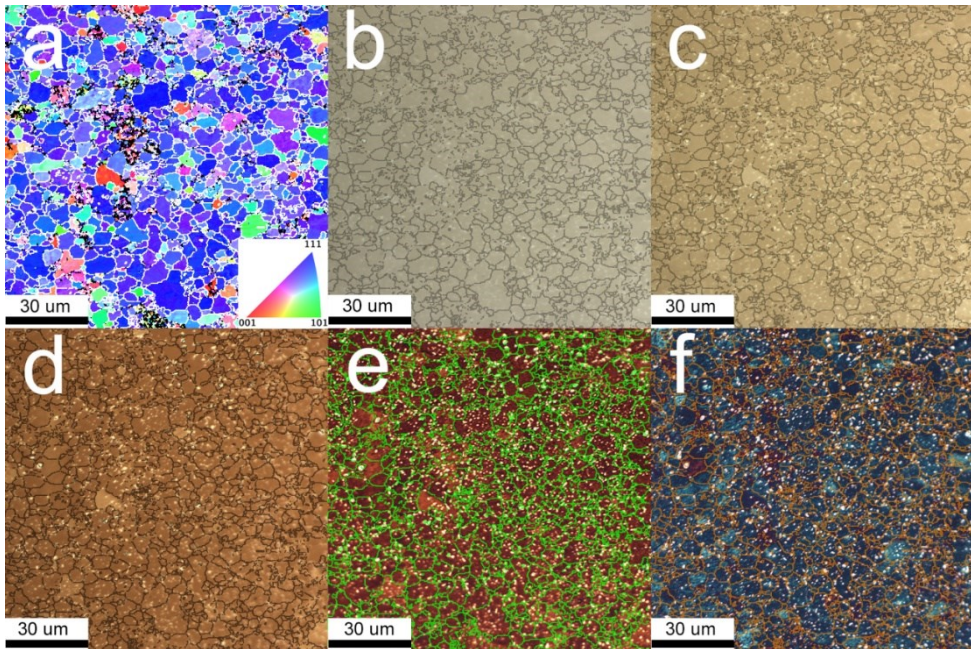
Figure 4.3. **(a)** *[001] inverse pole figure map of the global area of interest. Optical images with EBSD grain boundaries superimposed after heating at* **(b)** *260 °C;* **(c)** *260, 300 °C;* **(d)** *260, 300, 350 °C;* **(e)** *260, 300, 350, 400 °C and* **(f)** *260, 300, 350, 400, 450 °C, for 20 minutes at each temperature. The superimposed boundaries are varied in colour to enhance the contrast of the boundaries and the microstructure.*

The deviating areas have the same size and shape as the grains with the {100} planes on the surface (red/orange grains in Fig 4.2a). Not only "pure", but also orientations close to {100} planes show a lack of oxidation. The surface after oxidation step 5, shown in Fig. 4.2f, is different compared to oxidation step 1 to 4. Here three main colours can be distinguished: dark red, dark blue, light blue. The intense light blue grains, which are the most oxidized, correspond to the grains with {101} planes (in green) of Fig. 4.2a. The dark red spots correspond to the {100} grains, however they are not homogeneously coloured and partly decorated by ridges of blue oxide spheres. There are two reasons to exclude that the orientation of the planes at the surface are influencing the reflectivity and therefore the brightness of individual grains.

First, no difference in brightness between the grains are observed on a fresh polished surface, but after short oxidation it is seen (Fig. 4.2b). Second, these particular {100} grains should also be brighter in the final oxidation step in

Fig. 4.2f, which is not the case. A similar observation was confirmed on a more global scale in Fig. 4.3 and therefore the correlation between surface crystal plane and its degree of oxidation is not due to local effects. In Fig. 4.3 for each oxidation step the global microstructure is seen with the grain boundaries highlighted. The colour of the grains for different oriented planes is schematically depicted in Fig. 4.4. Hence the relative oxidation speed of the particular grain orientations can be categorized in two stages. Figs. 4.2 and 4.3 show snapshots of the oxidation at discrete temperatures. The different oxidation processes change gradually whereby the first stage is mainly present up to 350 °C; the second stage is most pronounced at 450 °C.

- At the first stage of oxidation the system is split in {001} planes lacking behind and {111} & {101} both progressing more: {001} < {111} & {101}.
- The second stage of oxidation is split into a threefold system with {001} planes still behind but {101} more progressed than {111}: {001} < {111} < {101}.
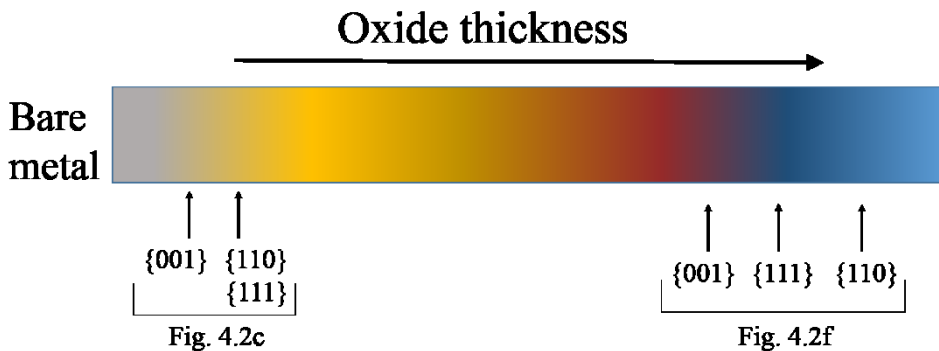
Figure 4.4. Colour change of the grain due to increase of oxide thickness according to [2,38,39]. The colour of the grains with different oriented planes is placed together with the colour sequence for two stages of the oxidation process as seen in Fig. 4.2.

In Fig. 4.5 an area of 240 x 240 μm^2 shows that stage 1 oxidation is not a local or an incidental phenomenon, but observed on a global scale. The clearly visible deviating areas again coincide with the grains with {100} planes parallel to the surface, underlining their relation. Darker patches are also observed where the

colour difference is caused by the lack of carbides on the surface in these areas. The carbides have a high reflection, which is facile observed with the optical microscope at high (100x) magnification, contributing to a lighter or darker perception of the area. There is no relation between these patches and the orientation of the grains.
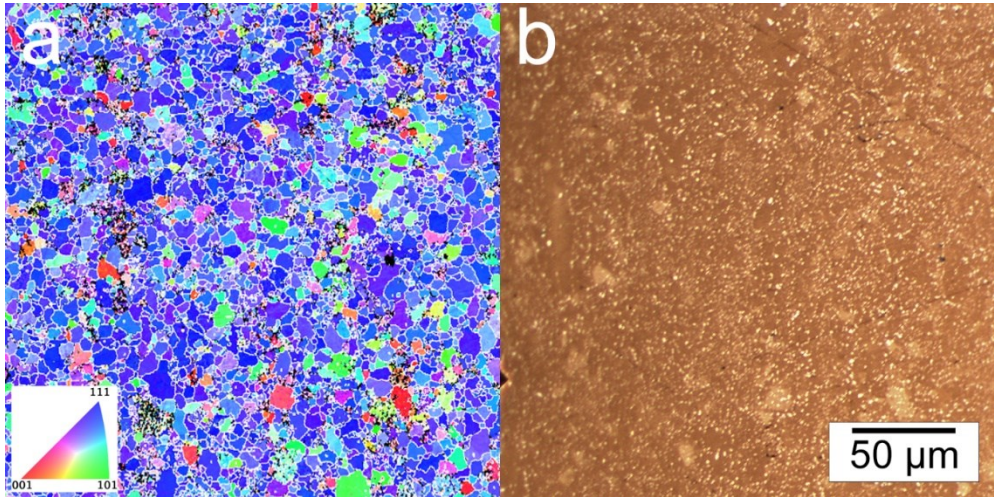
Figure 4.5. Specimen surface after sequential heating at 260, 300 and 350 °C for 20 minutes at each temperature. (a) (001) Inverse Pole Figure with grain boundaries (white) on which the different crystal plane orientation parallel to the surface of the substrate are shown. (b) Light microscopy image from the same area on which a difference in degree of oxidation is observed on the surface. A good correlation between the grain with a {001} plane on the surface and the lighter degree of oxidation is observed. Furthermore, {011} and {111} planes have a similar degree of oxidation.

4.3.1 Oxide layer chemical composition

In order to characterize the chemical composition of the oxide layer, a specimen was oxidized for 20 minutes at 300 °C in air. An XPS depth-profile was obtained by alternating measurements and sputtering of the surface by Ar ions. A selection of the Fe-2p spectra with increasing sputtering time is shown in Fig. 4.6. The initial –not Ar ion etched- surface shows a Fe-2p spectrum with the Fe-2p$_{3/2}$ peak position around 711.3 eV and a satellite peak at around 720 eV, which is associated to the Fe^{3+} valence and therefore the chemical compound Fe$_2$O$_3$ oxide

[41,42]. After 20 minutes of etching the satellite at 720 eV vanished, but it reappears at 716 eV after 110 minutes. In the latter structure, where the Fe $2p_{3/2}$ peak position also shifts towards 710.5 eV a structure containing Fe^{2+} valence is detected. A structure containing solely Fe^{2+}, e.g. Wüstite (FeO), also shows a satellite at 715.5 eV, but also a main peak at 709.5 eV [41,42]. Magnetite (Fe_3O_4) has a main peak at 710.6 eV, but no clear satellite peak [41,42]. The clear spectrum after 345 minutes etching has a peak at 707.4 eV, which agrees very well to metallic Fe; it indicates that the oxide layer has been removed and the bulk/substrate is reached. Therefore it is clear that the spectrum from the surface matches very well to Fe_2O_3, and the spectrum at the end of the oxide layer to (bulk) metallic Fe, however in-between additional (satellite) peaks are observed which is an artefact of the argon ion etching, whereby Fe^{3+} is chemically reduced to Fe^{2+} and preferential sputtering of O can take place. It is demonstrated in [43] how an XPS spectrum can change by sputtering of pure Fe_2O_3, in which the first three stadia of the depth profile as seen in Fig. 4.6 can also be recognized. It is important to mention that the magnetite can be written as $FeO.Fe_2O_3$, however since Wüstite is only stable at a temperature above 550 °C [4], it is not likely to be present. Pure magnetite is an inverse spinel with divalent and trivalent Fe and describes as $Fe^{3+}(Fe^{3+}Fe^{2+})O_4$ [44,45]. In contrast Chromite, $FeCr_2O_4$ is a normal spinel with $Fe^{2+}(Cr^{3+})_2O_4$. Due to the relative abundance of Fe, it is more likely that Cr inhibited in the spinel will be present in an inverse spinel of $Fe^{3+}(Cr^{3+}Fe^{2+})O_4$ [46]. It has been shown that XPS spectra can be deconvoluted to resolve the Fe-2p [47] spectra, but in this work they cannot provide a conclusive answer to the question which specific iron oxides are present in the core of the oxide layer as the oxides can contain both Fe^{2+} and Fe^{3+}. Therefore, we turn to the quantitative information from the elemental distribution ratio.
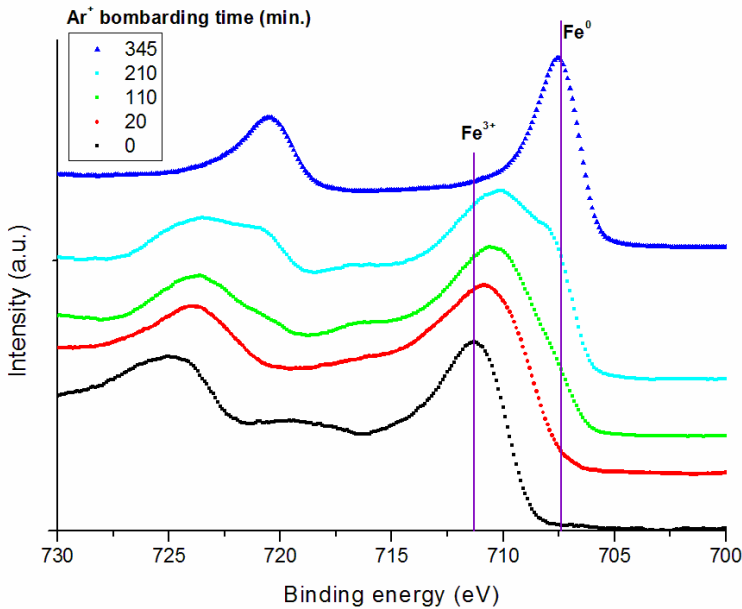
Figure 4.6. Fe-2p XPS spectra after Ar etching for 0, 20, 110 210 and 345 minutes, from a specimen oxidized for 20 minutes at 300 °C. Observed is the transition from Fe^{3+} (0 min.) to fully metallic Fe (345 min.).

The normalized peak intensities as a function of the sputtering time for Fe, Cr and O, which are the three main elements found in the oxide layer, are plotted in Fig. 4.7. This elemental depth-profile is constructed by the summation of all valence peaks of each individual element, e.g. the full Fe-$2p_{3/2}$ peak. No other elements were detected; except for carbon which is only present in small quantities in the carbides, grain boundaries and as contamination on the surface. At the initial oxide/gas interface (t=0 min.) a relative high concentration of oxygen is present. This can be due to carbon contamination, but it is also likely that hydroxide groups are present [48,49]. After 10 minutes of sputtering these hydroxide groups were removed. Up to t=100 min. the iron/oxygen ratio is about 40/60, indicating presence of the structure Fe_2O_3. The following decrease of O content and increase of Fe suggests a shift towards the inverse spinel Fe_3O_4. At t=160 min. a small peak of metallic Fe is noticed, which increases as the bulk is reached (see Fig. 4.6). The contribution of this peak increases the relative intensity of iron in Fig. 4.7, troubling the determination of iron oxide structure. Finally, a Cr enrichment peaking after 300 minutes is observed, just before the substrate–oxide interphase.

It must be noted that the XPS provides information over a depth of 5 - 10 nm. Therefore, acquired information from layers of specific oxide structures of only several nm thick, will be accompanied by signals from the surrounding layers. The lateral resolution is limited by the spot size of 600 μm in diameter. The retrieved signal contains therefore in our case the information of the surface of several thousands of grains. It is concluded that on average after heating at 300 °C the outer layer consist of Fe_2O_3, which is about 1/3 of the total oxide layer thickness.

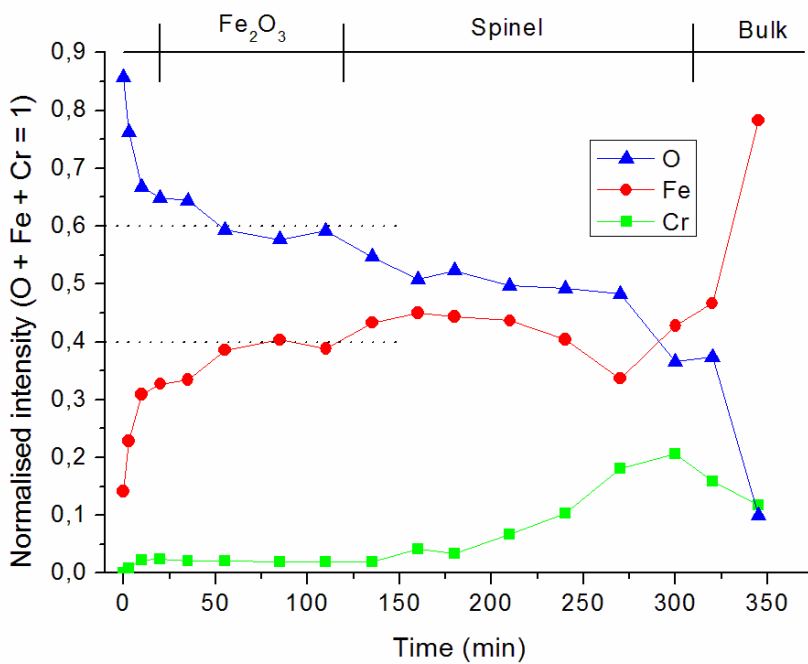*Figure 4.7. XPS depth profile of the surface, after tempering for 20 minutes at 300 °C in air. The top layer (t=0-100 min.) consists mainly of iron oxide, presumably Fe_2O_3 with a Fe/O ratio of 40/60; a chromium enrichment is observed before bulk composition values are reached (t = 345 min.). The intensity of each element is the summation of all valence peaks.*

4.3.2 Oxide structural composition

We have examined in detail the crystallography and crystal phases with XRD and GIXRD. Both X-ray methods give us global information about the crystallographic phases present, in contrast to the EBSD measurement which gives primarily local information. The crystallinity and texture of the substrate was measured with powder-XRD and was used as a reference measurement. For the phase and crystallinity information of the grown oxide layer we performed GIXRD measurements after short tempering, 20 minutes at 300 °C (yellow surface), and after long tempering procedure, oxidized up to 450 °C (purple surface) with the same treatment as oxidation step 5 in Table 4.1. The information depth was varied by changing the incident angles; we used three different incident angles 0.25°, 0.33° and 0.50° corresponding to an information depth of 18, 24 and 37 nm, respectively.

The GIXRD spectra for both specimens are shown in Fig. 4.8 for both the short tempered (yellow) and long tempered (purple) specimens with the corresponding crystal planes of the phases present. For the short tempered specimen the peak positions and intensities for the different depths are similar. However, small differences in peak intensities are observed for peak 1 and 3, whilst peak 2 has a constant intensity. The inset in Fig. 4.8a is a magnification of peak 3 (near $2\theta=83°$) and shows a clear increase of peak height with increasing incident angle. Peak 1 (near $2\theta=45°$) and peak 3 correspond to both the Fe$_{bcc}$ as well as the Fe$_3$O$_4$ phase. Whilst both the (Fe-Cr)$_{bcc}$ substrate and the Fe$_3$O$_4$ give diffraction peaks at similar angles, by removing the background we observed that the peak positions agree better with Fe$_3$O$_4$ than the (Fe-Cr)$_{bcc}$ phase. Moreover, the relative peak intensity for the three peaks differs from the bulk measurement performed by powder XRD. This difference is in agreement with an additional magnetite top layer on the substrate. The normalized intensity peaks seen in the inset of Fig. 4.8a show an increase of the Fe$_3$O$_4$ fraction with decreasing incidence angle. It is therefore concluded that the measured oxide film is very thin and a large part of the information is measured from the oxide-substrate interface.

The GIXRD spectra reveal that the oxide layer of the purple surface is more developed compared to the short tempered yellow specimen due to the clear presence of crystalline Fe$_2$O$_3$ and Fe$_3$O$_4$ phases. Fig. 4.8b shows a more distinct change in diffraction spectrum with depth than the short tempered specimen with more peaks. Again, we observe a difference in the relative peak intensities for the peaks at 44.8, 65.2 and 82.5° 2*theta compared to the substrate measurement;

thereby confirming a magnetite layer. The additional peaks are all attributed to the formed hematite layer due to the extra oxidation steps. The hematite crystals grow according to a specific orientation relation on the crystalline magnetite surface therefore only specific hematite crystal planes are measured. Because the polycrystalline stainless steel substrate is highly crystallographic textured, some magnetite and hematite crystal orientations are more pronounced present than others, due to the orientation relationship (OR) between substrate and magnetite, and a second OR between the hematite grown on magnetite. These orientation relationships for a pure Fe system with its oxidation products was already demonstrated for single crystals in [50].

In our analysis of a polycrystalline Fe-Cr system several oxide phases were found; an overview is presented in Table 4.2. Cr can be present in the inverse spinel as well as Cr_2O_3 with the corundum hexagonal structure. These Cr containing phases have a similar diffraction spectrum as the iron oxide phases, however in the GIXRD results in this work the Cr phases show a worse agreement with the expected peak position than Fe_3O_4.and Fe_2O_3. Furthermore, considering the maximum information depth of 37 nm at an incidence angle of 0.5°, it is likely that the Cr-enriched layer close to the metal/oxide interphase (as seen in Fig. 4.7) is not reached. The total oxide thickness of a purple oxidized Fe specimen suggests a total oxide thickness of 59 – 72 nm [38,40]. With increasing angle of incidence, i.e. deeper in the oxide layer, we see that the intensity of the peaks corresponding to Fe_3O_4 (222) as well as Fe_2O_3 (211) decreases, and Fe_2O_3 (312) decreases significantly; the intensity of the peak corresponding to Fe_2O_3 (433) decreases and almost vanishes.

Table 4.2. Phases found on oxidized polycrystalline Fe-Cr steel, as detected in Fig. 4.8.

Phase	Crystal plane ‖ surface
Fe-Cr$_{bcc}$	(101); (200); (211)
Fe$_3$O$_4$	(222); (400); (404); (444)
Fe$_2$O$_3$	(211); (312); (332); (433)
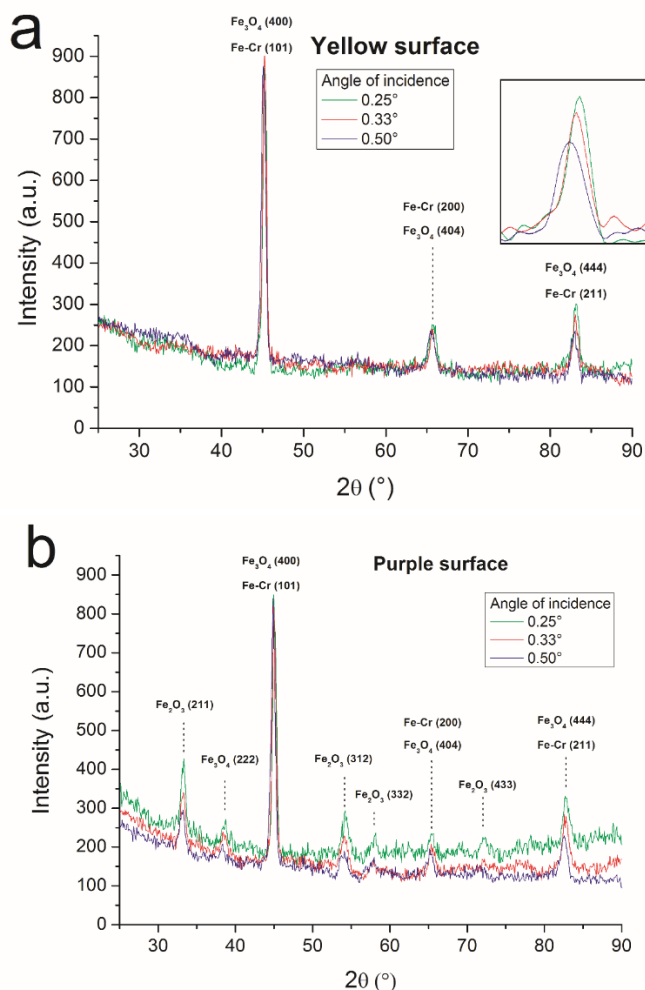
Figure 4.8. Phase and crystallographic information of the top oxide layer measured by GIXRD at different incident angles (0.25°, 0.33° and 0.50°) which correspond with a maximum information depth of 18, 24 and 37 nm, respectively. (a) GIXRD spectrum for the yellow specimen. The composition up to a depth of 37 nm has no significant change in layer composition. Moreover, the amounts of oxide products (magnetite and hematite) are hardly present at all. The inset shows a magnification of peak near $2\theta=83°$. (b) GIXRD spectrum for the purple specimen. The amount of oxide products (magnetite and hematite) are well detectable, however the amounts do not vary a lot. A significant difference in background signal is observable due to a change in the amorphous/crystalline ratio.

4.4 Discussion

For polycrystalline stainless steel we observed a similar build-up of the oxidation layer as found in Fe systems: the short tempered (yellow) specimen at 300 °C, XPS results indicate both the outer hematite and inner magnetite layer. However, the GIXRD results show mainly the peaks of the {111} magnetite crystal planes, where also multiple peaks for hematite were expected. This suggests that magnetite with a {111} crystal plane parallel to the surface is the only magnetite which grows crystalline on the polycrystalline surface. The lack of detected hematite in the GIXRD results, despite the hematite outer layer found by XPS, is attributed to the non-epitaxial growth of the hematite on the {111} magnetite [50], as well as the possible amorphous state of hematite. Amorphous or nano-crystalline domains cannot be detected by GIXRD.

On the purple specimen, which was heated with a final temperature of 450 °C, both magnetite and hematite were detected by GIXRD, as summarized in Table 4.2. When we compare the crystallographic information to the results of oxidation of magnetite single crystals by Zhou et al. [50], as shown in Table 4.3; we conclude that the hematite phases found in this work correspond mainly to the oxidation products found on {111} magnetite. Similar to literature, after heating several hours at 450 °C, also a double layer was found, though with a very small top layer of hematite, compared to magnetite [32]. Also after continued heating, the magnetite sub-layer grew faster than the hematite top layer.

Table 4.3. Iron oxide phases found on magnetite single crystals, from Zhou et al. [50].

Magnetite	Fe_3O_4	Fe_2O_3
(100)	(400)	(120); (132)
(110)	(220); (440)	(-211)
(111)	(222); (444)	(121); (132); (343)

Notwithstanding the importance of the oxidation process on the surface of complex materials as polycrystalline stainless steel rather scant literature was found on the detailed relationship between the crystallography and microstructure of the substrate. However, comparable work was performed to relate the crystallography

of Fe based substrates with the thickness and crystallography of the oxidation products.

Vernon [3] showed that for pure Fe oxidized in air a double layer was formed of an inner magnetite and outer hematite layer at 200 °C. Zhou [50] studied the oxidation of magnetite at 300 °C; it was concluded that the formation of hematite on (100) and (111) magnetite was not epitaxial; for (110) magnetite it was unlikely to be epitaxial. The work as presented in literature raises the question whether the same relationship holds for Fe-Cr based systems and whether crystallography of the different layers can be related to each other. For single crystal magnetite specifically oriented hematite crystals form on the differently oriented crystal planes, as listed in Table 4.3. For temperatures above 600 °C the oxidation film consists of a mixture of iron oxides, where Wüstite, magnetite and hematite are present. A layer by layer growth is observed on polycrystalline Fe for a pressure of $2x10^{-4}$ mbar at 500 °C, whilst for 700 °C island growth is observed due to Wüstite formation [51]. The question that arises for polycrystalline Fe-Cr steel is whether there is an orientation relationship (OR) between the substrate and the inner magnetite; and the magnetite and the outer hematite. Moreover, are there prevalent atomic planes which dominate the oxidation kinetics?

The oxidation rate on an α-Fe substrate depends on the crystal plane at the surface: in decreasing order of oxidation rate that is {001} > {111} > {011} > {320} [52,53], which is opposite to the results found on our polycrystalline stainless steel in phase II. A less dense packed crystal plane at the surface is more susceptible to oxidation than a dense packed plane, because diffusion from and into the substrate is more likely. It is shown for Fe at 500 °C that planes with an higher atom density exhibit faster oxidation kinetics in the initial oxidation reaction [51]. The diffusion rate of Fe to the surface is around 1-2 $x10^{-15}$ cm^2/s [53]. For the case of iron, at 250 °C and a low O_2 pressure a pure magnetite layer is formed on all planes; whilst at 550 °C for a higher O_2 pressure the oxidation film consists of an inner magnetite and outer hematite layer; the found OR for this layer was $\{001\}_{Fe}||\{001\}_M||\{114\}_H$ [54]. The growth rate of the hematite cap layer on the different magnetite planes (and therefore the oxidation speed) was ordered as (100) > (110) > (111) [50]. Therefore, the oxidation mechanism is not to be expected similar for polycrystalline stainless steel compared to iron.

Study on the initial oxidation at low pressures (~10^{-8} mbar) of Fe-Cr single crystals with chemical composition close to the material in this work gives us an insight in the influence of particular crystal planes at the surface when Cr is

involved. At room temperature oxidation starts with an initial Cr oxide layer followed by an iron oxide layer, whereby these thin oxide layers do not seem to have a "three-dimensional periodicity" [55]. If the oxidation takes place at 527 °C, also an initial Cr oxide layer is formed. The later formed iron oxide outer layer on the (100) crystal is a normal or inverse spinel-type phase with fcc symmetry, however no ordering is found on the (110) crystal [55].

It has to be emphasized that the magnetite layer does not grow directly on the Fe-Cr stainless steel, but rather on the passive layer present prior to the tempering treatment. This new finding for the Fe-Cr steel is a major difference compared to a Fe-system. As indicated by the XPS profile in Fig. 4.7, the passive layer is an (Fe,Cr)-oxide which is too thin to be detected by SEM, EBSD and GIXRD. Moreover, FeOOH could be present at the start of the tempering treatments, which decomposes to form Fe_2O_3 with increasing temperature.

Magnetite has the inverse spinel structure at low temperatures with an fcc oxygen sub-lattice structure. This means that all ions of Fe^{2+} valence and half of the Fe^{3+} occupy the octahedral sites and half of the Fe^{3+} occupy the tetrahedral sites [44,45]. Magnetite {111} planes therefore consist of octahedral and mixed octahedral/tetrahedral located atoms along the <111> directions. A relationship between oxidation rate and dense packed planes can be retrieved, namely that more dense packed planes are more susceptible for oxidation. Magnetite has a Verwey transition around -153 °C, above this temperature it will act as a half metal with mobile electrons. Therefore it is treated as one type of Fe without valence difference and their behavior is considered identical [56,57].

The attributed mechanism for oxidization of magnetite is mainly diffusion of iron cations by Zhou et al. [50], in which the diffusion constant is greater for <100> than along <110> and <111> directions. In contrast, our observation is that at temperatures < 400 °C the oxidation rate for the different crystal planes of the Fe-Cr substrate are in an increasing order {001} < {111}&{110}, which would mean that the dense packed planes are more susceptible to oxidation. Pöter et al. [51] showed that in the initial oxidation phase diffusion of cations from the bulk through the oxidation layer is faster than oxygen from the gas phase to the metal phase. For higher temperatures, (which generally increases diffusion), we observed a further distinction between oxidation rate and crystal planes of the substrate: {001} < {111} < {110}. Given that the OR in Table 4.4 is correct and due to the presence of the magnetite layer on the substrate at temperatures > 400 °C, the

following relation of oxidation rate and crystal planes of the magnetite can be deduced: {001} < {210} < {111}, which agrees with our GIXRD results.

For the diffusion of Fe towards the surface, the respective diffusion constant through the different oxide products, magnetite and hematite, is of great importance. However, also the vacancies present in the oxidation product play a crucial role [58].

Table 4.4. Orientation relationship between an α-Fe substrate and magnetite layer as well as a magnetite substrate and a hematite layer, from [53]*.*

α-Fe	Magnetite	Hematite
{001}<010>	{001}<110>	{114}
{011}<100>	{111}<110>	{001}<100>
{111}<011>	{210}<100>	{211}

The oxidation of polycrystalline Fe-Cr reveals a clear distinction between {100}, which is less oxidized, and {111} & {110} crystal planes, as shown in Fig. 4.2. For the initial oxidation of an Fe_{bcc} substrate, as summarized in [5], the adsorption of oxygen at room temperature results in faster oxidation on the more open Fe{111} surface. When oxidation proceeds, ordered phases on Fe{100} and Fe{110} are formed [5]. However, for unknown reasons the presence of Cr seems to cause an ordered oxide on Fe-Cr{100} and not on Fe-Cr{101} [55].

The initial oxidation in our polycrystalline material at a temperature below 400 °C seems a steady diffusion of cations through the spinel/magnetite layer, as schematically shown in Fig. 4.9. Oxidation seems to be controlled by bulk diffusion. The main argument here is that if transport of ions would occur predominantly along the grain boundaries, a thicker oxide on the grain boundaries would be present. Also lateral growth of the oxide from the boundaries on the grains would take place: phenomena which were not observed in Fig. 4.2. On the contrary, the individual grains possess a very uniform colour contrast and brightness, an indication of a uniform oxide layer. A process which is changing when the temperature is increased towards 450 °C: a non-regular grain decoration is started to be seen, with possible iron oxide substructures, not corresponding to grain boundaries.

On the base of the above presented results and discussion we propose the following physical picture. At temperatures above 200 °C the diffusion speed of

cations is promoted. Fe is diffusing faster through the non-structured magnetite layer on Fe-Cr{101} and Fe-Cr{111} compared to more difficult traveling through ordered structures on Fe-Cr{100}.
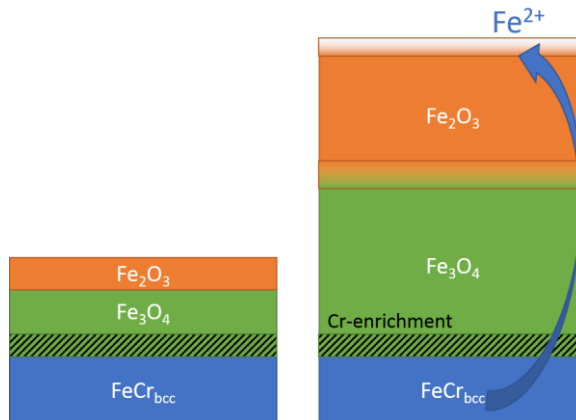

Figure 4.9. Schematic representation of the growth of the oxide layer on Fe-Cr steel. Left: passive layer in the order of several nanometres prior to heat treatment. Right: iron cation diffusion and increasing oxide thickness towards tenths of nanometres during a heat treatment in air.

It could be argued that the systems on single crystals studied in literature may apply to describe the system of a polycrystalline alloy. Surprisingly the polycrystalline structure oxidized in a uniform way per grain orientation, where for the first oxidation stage the oxide growth direction was normal to the surface. This allowed for a multi "single crystal" approach where results obtained for single crystals in literature contributed to the understanding of the oxide structure per grain. It is observed that due to the alloying with Cr, the ORs between the substrate and magnetite are not identical compared to a system with a pure iron substrate. It is, however, the addition of Cr which is beneficial to the corrosion resistance by suppression of ion diffusion. Since the start of this process by Faraday, Stodart and Bertier almost 200 years ago, research on this topic expanded from a pure chemical approach to an approach where the material crystallography is central. Considering experimental conditions representing industrial conditions, this Chapter is aimed to the understanding of bulk processes on nano- and micro level, hence bridging the gap between metallurgy, microstructural analysis and the onset of corrosion.

4.5 Conclusions

The major conclusions are the following:

There is a bulk grain crystal orientation – oxidation progression relationship for polycrystalline Fe-Cr steel. The driving factor is the diffusion constant, which is influenced by temperature. The different oxidation processes change gradually whereby the first stage is mainly present up to 350 °C, second stage is most pronounced at 450 °C.

- At the start of oxidation the surface oxidation is decomposed in {001} lacking behind of {111} & {101} planes: {001} < {111} & {101}.
- The second stage of oxidation is split into a threefold system with {001} planes still lacking behind, but {101} progress faster than {111}: {001} < {111} < {101}.

The oxide layer consists of a crystalline magnetite inner, and hematite outer sublayers.

The order of oxidation progression i.e. {001} < {111} & {101}, has not been reported in literature. In fact for a Fe based system, {001} is found to have the relative highest oxidation progression, as opposed to results of this work for a Fe-Cr alloy.

4.6 References

[1]   N. Cabrera, N.F. Mott, Theory of the oxidation of metals, Reports Prog. Phys. 12 (1949) 163–184. doi:10.1088/0034-4885/12/1/308.

[2]   W.H.J. Vernon, F. Wormwell, T.J. Nurse, The Thickness of Air-formed Oxide Films on Iron, J. Chem. Soc. (1939) 624–632.

[3]   W.H.J. Vernon, E.A. Calnan, C.J.B. Clews, T.J. Nurse, The Oxidation of Iron around 200 degrees C, Proc. R. Soc. A Math. Phys. Eng. Sci. 216 (1953) 375–397. doi:10.1098/rspa.1953.0028.

[4]   W. Weiss, W. Ranke, Surface chemistry and catalysis on well-defined epitaxial iron-oxide layers, Prog. Surf. Sci. 70 (2002) 1–151. doi:10.1016/S0079-6816(01)00056-9.

[5]   G.S. Parkinson, Iron oxide surfaces, Surf. Sci. Rep. (2016) 272–365. doi:10.1016/j.surfrep.2016.02.001.

[6]   J. Stodart, M. Faraday, Experiments on the alloys of steel made with a view to its improvement, Philos. Mag (Ser. 1). 56 (1820) 26–35. doi:10.1080/14786442008652361.

[7]   P. Berthier, Sur les Alliages du chrôme avec le fer et avec l'acier, Ann. Chim. Phys. XVII (1821) 55–64.

[8]   J. Stodart, M. Faraday, On the Alloys of Steel, Philos. Trans. R. Soc. London. 112 (1822) 253–270.

[9]   C.O.A. Olsson, D. Landolt, Passive films on stainless steels - Chemistry, structure and growth, Electrochim. Acta. 48 (2003) 1093–1104. doi:10.1016/S0013-4686(02)00841-1.

[10]   I. Olefjord, H. Fischmeister, ESCA studies of the composition profile of low temperature oxide formed on chromium steels-II. Corrosion in oxygenated water, Corros. Sci. 15 (1975) 697–707. doi:10.1016/0010-938X(75)90034-7.

[11]   S. Jin, A. Atrens, Passive films on stainless steels in aqueous media, Appl. Phys. A. 50 (1990) 287–300. doi:10.1007/BF00324495.

[12]   D. Ramachandran, R. Egoavil, A. Crabbe, T. Hauffman, A. Abakumov, J. Verbeeck, I. Vandendael, H. Terryn, D. Schryvers, TEM and AES investigations of the natural surface nano-oxide layer of an AISI 316L stainless steel microfibre, J. Microsc. 264 (2016) 207–214. doi:10.1111/jmi.12434.

[13]   F. Qin, N.P. Magtoto, M. Garza, J. a. Kelber, Oxide film growth on Fe(111) and scanning tunneling microscopy induced high electric field stress in Fe2O3/Fe(111), Thin Solid Films. 444 (2003) 179–188. doi:10.1016/j.tsf.2003.08.043.

[14]   T. Ossowski, A. Kiejna, Oxygen adsorption on Fe(110) surface revisited, Surf. Sci. 637–638 (2015) 35–41. doi:10.1016/j.susc.2015.03.001.

[15]   S. Ekelund, C. Leygraf, A LEED-AES STUDY OF THE OXIDATION OF Cr(110) AND Cr (100), Surf. Sci. 40 (1973) 179–199.

[16]   P. Michel, C. Jardin, Oxygen adsorption and oxide formation on Cr(100) and Cr(110) surfaces, Surf. Sci. 36 (1973) 478–487. doi:10.1016/0039-6028(73)90396-8.

[17]   G. Gewinner, J.C. Peruchetti, A. Jaegle, A. Kalt, Photoemission study of the chromium(111) surface interacting with oxygen, Surf. Sci. 78 (1978) 439–458. doi:10.1016/0039-6028(78)90090-0.

[18]   V. Maurice, S. Cadot, P. Marcus, XPS , LEED and STM study of thin oxide films formed on Cr(110), Surf. Sci. 458 (2000) 195–215.

[19]   J.R. Lince, S. V. Didziulis, D.K. Shuh, T.D. Durbin, J.A. Yarmoff, Interaction of O2 with the Fe0.84Cr0.16(001) surface studied by photoelectron spectroscopy, Surf. Sci. 277 (1992) 43–63. doi:10.1016/0039-6028(92)90611-9.

[20]   H. Fujiyoshi, T. Matsui, J. Yuhara, Segregation and morphology on the surface of ferritic stainless steel (001), Appl. Surf. Sci. 258 (2012) 7664–7667. doi:10.1016/j.apsusc.2012.04.116.

[21]   F. Genuzio, A. Sala, T. Schmidt, D. Menzel, H.-J. Freund, Interconversion of α‑Fe2O3 and Fe3O4 Thin Films: Mechanisms, Morphology, and Evidence for Unexpected Substrate Participation, J. Phys. Chem. C. 118 (2014) 29068–29076. doi:10.1021/jp504020a.

[22]   F. Genuzio, A. Sala, T. Schmidt, D. Menzel, H.J. Freund, Phase transformations in thin iron oxide films: Spectromicroscopic study of velocity and shape of the reaction fronts, Surf. Sci. 648 (2016) 177–187. doi:10.1016/j.susc.2015.11.016.

[23]   S.-Y. Lu, K.-F. Yao, Y.-B. Chen, M.-H. Wang, X.-Y. Ge, Influence of Heat Treatment on the Microstructure and Corrosion Resistance of 13 Wt Pct Cr-Type Martensitic Stainless Steel, Metall. Mater. Trans. A. 46 (2015) 6090–6102. doi:10.1007/s11661-015-3180-1.

[24]   S.Y. Lu, K.F. Yao, Y.B. Chen, M.H. Wang, N. Chen, X.Y. Ge, Effect of quenching and partitioning on the microstructure evolution and electrochemical properties of a martensitic stainless steel, Corros. Sci. 103 (2015) 95–104. doi:10.1016/j.corsci.2015.11.010.

[25]   S.Y. Lu, K.F. Yao, Y.B. Chen, M.H. Wang, X. Liu, X. Ge, The effect of tempering temperature on the microstructure and electrochemical properties of a 13 wt.% Cr-type martensitic stainless steel, Electrochim. Acta. 165 (2015) 45–55. doi:10.1016/j.electacta.2015.02.038.

[26]   B. Pujilaksono, T. Jonsson, H. Heidari, M. Halvarsson, J.-E. Svensson, L.-G. Johansson, Oxidation of Binary FeCr Alloys (Fe–2.25Cr, Fe–10Cr, Fe–18Cr and Fe–25Cr) in O2 and in O2 + H2O Environment at 600 °C, Oxid. Met. 75 (2011) 183–207. doi:10.1007/s11085-010-9229-z.

[27]   T. Jonsson, B. Pujilaksono, H. Heidari, F. Liu, J.-E. Svensson, M. Halvarsson, L.-G. Johansson, Oxidation of Fe–10Cr in O2 and in O2+H2O environment at 600°C: A microstructural investigation, Corros. Sci. 75 (2013) 326–336. doi:10.1016/j.corsci.2013.06.016.

[28]   T. Jonsson, S. Karlsson, H. Hooshyar, M. Sattari, J. Liske, J.-E. Svensson, L.-G. Johansson, Oxidation After Breakdown of the Chromium-Rich Scale on Stainless Steels at High Temperature: Internal Oxidation, Oxid. Met. 85 (2016) 509–536. doi:10.1007/s11085-016-9610-7.

[29]   I. Saeki, T. Saito, R. Furuichi, H. Konno, T. Nakamura, K. Mabuchi, M. Itoh, Growth process of protective oxides formed on type 304 and 430 stainless steels at 1273 K, Corros. Sci. 40 (1998) 1295–1305.

[30]   J. Yuan, W. Wang, H. Zhang, L. Zhu, S. Zhu, F. Wang, Investigation into the failure mechanism of chromia scale thermally grown on an austenitic stainless steel in pure steam, Corros. Sci. 109 (2016) 36–42. doi:10.1016/j.corsci.2016.03.021.

[31]   D.-I.H. Kim, S.H. Phaniraj, M.P. Han, J.-P. H.N. Ahn, W.Y. Cho, Microstructural analysis of oxide layer formation in ferritic stainless steel interconnects, Mater. High Temp. 28 (2011) 285–289. doi:10.3184/096034011X13185032513419.

[32]   C. Juricic, A.H. Pinto, A.D. Cardinali, A.M. Klaus, C. Genzel, A.A.R. Pyzalla, Effect of Substrate Grain Size on the Growth, Texture and Internal Stresses of Iron Oxide Scales Forming at 450 °C, Oxid. Met. 73 (2010) 15–41. doi:10.1007/s11085-009-9162-1.

[33] Y. Takabatake, Y. Kitagawa, T. Nakanishi, Y. Hasegawa, K. Fushimi, Heterogeneity of a Thermal Oxide Film Formed on Polycrystalline Iron Observed by Two-Dimensional Ellipsometry, J. Electrochem. Soc. 163 (2016) C815–C822. doi:10.1149/2.0211614jes.

[34] K. Fushimi, A. Kazuhisa, M. Seo, Evaluation of Heterogeneity in Thickness of Passive lron by Scanning Flectrochemical Microscopy Films on Pure, ISIJ Int. 39 (1999) 346–351.

[35] A. Schreiber, C. Rosenkranz, M.M. Lohrengel, Grain-dependent anodic dissolution of iron, Electrochim. Acta. 52 (2007) 7738–7745. doi:10.1016/j.electacta.2006.12.062.

[36] K. Fushimi, Y. Takabatake, T. Nakanishi, Y. Hasegawa, Microelectrode techniques for corrosion research of iron, Electrochim. Acta. 113 (2013) 741–747. doi:10.1016/j.electacta.2013.03.021.

[37] Y. Takabatake, Y. Kitagawa, T. Nakanishi, Y. Hasegawa, K. Fushimi, Grain Dependency of a Passive Film Formed on Polycrystalline Iron in pH 8.4 Borate Solution, J. Electrochem. Soc. 164 (2017) C349–C355. doi:10.1149/2.1011707jes.

[38] U.R. Evans, The Colours Due to Thin Films on Metals, Proc. R. Soc. A Math. Phys. Eng. Sci. 107 (1925) 228–237.

[39] R.L. Higginson, C.P. Jackson, E.L. Murrell, P.A.Z. Exworthy, R.J. Mortimer, D.R. Worrall, G.D. Wilcox, Effect of thermally grown oxides on colour development of stainless steel, Mater. High Temp. 32 (2015) 113–118. doi:10.1179/0960340914Z.00000000083.

[40] F.H. Constable, Spectroscopic observations on the growth of oxide films on Iorn, Nickel, and Copper, Proc. Roy. Soc. 117 (1928) 376–387.

[41] T. Fujii, F.M.F. De Groot, G.A. Sawatzky, F.C. Voogt, T. Hibma, K. Okada, In situ XPS analysis of various iron oxide films grown by NO2-assisted molecular-beam epitaxy, Phys. Rev. B. 59 (1999).

[42] T. Yamashita, P. Hayes, Analysis of XPS spectra of Fe2+ and Fe3+ ions in oxide materials, Appl. Surf. Sci. 254 (2008) 2441–2449. doi:10.1016/j.apsusc.2007.09.063.

[43] S. Suzuki, K. Sugiyama, Y. Waseda, Changes in the Chemical State and Composition of the Surface of Iron Oxides due to Argon Ion Sputtering, J. Surf. Anal. 9 (2002) 455–458.

[44] E.J.W. Verwey, E.L. Heilmann, Physical Properties and Cation Arrangement of Oxides with Spinel Structures I, J. Chem. Phys. 15 (1947) 1091–120. doi:10.1063/1.1747852.

[45] E.J. Verwey, P.W. Haayman, F.C. Romeijn, Physical Properties and Cation Arrangement of Oxides with Spinel Structures II, J. Chem. Phys. 15 (1947) 181–187. doi:10.1063/1.1746466.

[46] H.J. Yearian, J.M. Kortright, R.H. Langenheim, Lattice Parameters of the FeFe(2—x)CrxO4 Spinel System, J. Chem. Phys. 22 (1954) 1196–7. doi:10.1063/1.1740331.

[47]   M.C. Biesinger, B.P. Payne, A.P. Grosvenor, L.W.M. Lau, A.R. Gerson, R.S.C. Smart, Resolving surface chemical states in XPS analysis of first row transition metals, oxides and hydroxides: Cr, Mn, Fe, Co and Ni, Appl. Surf. Sci. 257 (2010) 2717–2730. doi:10.1016/j.apsusc.2010.10.051.

[48]   J. Landoulsi, M.J. Genet, S. Fleith, Y. Touré, I. Liascukiene, C. Méthivier, P.G. Rouxhet, Organic adlayer on inorganic materials: XPS analysis selectivity to cope with adventitious contamination, Appl. Surf. Sci. 383 (2016) 71–83. doi:10.1016/j.apsusc.2016.04.147.

[49]   R. Steinberger, C.E. Celedón, B. Bruckner, D. Roth, J. Duchoslav, M. Arndt, P. Kürnsteiner, T. Steck, J. Faderl, C.K. Riener, G. Angeli, P. Bauer, D. Stifter, Oxygen accumulation on metal surfaces investigated by XPS, AES and LEIS, an issue for sputter depth profiling under UHV conditions, Appl. Surf. Sci. 411 (2017) 189–196. doi:10.1016/j.apsusc.2017.03.163.

[50]   Y. Zhou, J. Xuesong, Y.M. Mukovskii, I. V Shvets, Kinetics of oxidation of low-index surfaces of magnetite, J. Phys. Condens. Matter. 16 (2004) 1–12. doi:10.1088/0953-8984/16/1/001.

[51]   B. Pöter, I. Parezanović, M. Spiegel, In-situ scanning electron microscopy and electron backscatter diffraction investigation on the oxidation of pure iron, Mater. High Temp. 22 (2005) 185–193. doi:10.1179/mht.2005.021.

[52]   J.B. Wagner, K.R. Lawless, A.T. Gwathney, Rate of formation and structure of oxide films formed on single crystal of iron, Trans. Met. Soc. AIME. 221 (1961) 257–261.

[53]   R.M. Cornell, U. Schwertmann, The Iron Oxides: Structure, Properites, Reactions, Occurences and Users, 2nd ed., WILEY-VCH, 2003.

[54]   M. Gebhardt, Epitaxy in crystal growth: An introduction, North-Holland Publishing Co, 1973.

[55]   C. Leygraf, G. Hultquist, S. Ekelund, A LEED/AES study of the oxidation of Fe0.84Cr0.16 (100) and (110), Surf. Sci. 51 (1975) 409–432. doi:10.1016/0039-6028(75)90391-X.

[56]   F.A. Kröger, H.J. Vink, Relations between the Concentrations of Imperfections in Crystalline Solids, Solid State Phys. - Adv. Res. Appl. 3 (1956) 307–435. doi:10.1016/S0081-1947(08)60135-6.

[57]   N.F. Mott, Materials with mixed valency that show a verwey transition, Philos. Mag. B Phys. Condens. Matter; Stat. Mech. Electron. Opt. Magn. Prop. 42 (1980) 327–335. doi:10.1080/01418638008221874.

[58]   S. Hallström, L. Höglund, J. Ågren, Modeling of iron diffusion in the iron oxides magnetite and hematite with variable stoichiometry, Acta Mater. 59 (2011) 53–60. doi:10.1016/j.actamat.2010.08.032.

Chapter 5

Phase transformation characteristics

This Chapter presents the results obtained with in-situ high temperature electron-back scatter diffraction (HT-EBSD). We concentrate on the dynamics of interphase boundary motion during transformations. HT EBSD was employed to study the ferrite-austenite-ferrite transformation in low carbon steel. A novel method was designed to derive the velocity of the interphase boundaries from the EBSD phase maps. It is concluded that the motion of the transformation front occurs in a jerky-type motion, i.e. not continuous in time on a microscale, as the Johnson-Mehl-Avrami-Kolmogorov (JMAK) equation would predict on the macro-scale. As development of material science seems to proceed in a jerky type motion, so does the interphase boundary.

5.1 Introduction

Many laws in phenomenological materials physics are based on the concept that a constant force or driving force will lead to a response which is constant in time. In fact, the entire framework of solid mechanics, founded by Isaac Newton himself, is based on this principle. For example, a constant force per unit of area will lead to a particular deformation response everywhere and at any time in the material; also, a constant driving force will lead to a certain velocity at each point of an interface and to recrystallization and transformation kinetics well described by various phenomenological models. In this Chapter 5 we concentrate on the dynamics of phase transformations in time as a function of temperature. The Russian mathematician Kolmogorov and American metallurgists Johnson, Mehl

and Avrami independently formulated the first mathematical descriptions of isothermal solid-state phase transformation kinetics [1] for the fraction of transformed volume *f*:

$$f = 1 - \exp(-kt^n), \tag{5.1}$$

where k and n are time-independent constants for a particular reaction. Note that k cannot be considered a frequency factor as its unit depends on the value of the exponent n. In fact it would be better to formulate the exponent as *(kt)^n* with *k* is per unit of s^{-1}. Nevertheless, this modification will not affect the analysis as Eq. (5.1) is developed for a constant value of *n*. The resulting model is nowadays known as the Johnson-Mehl-Avrami-Kolmogorov (JMAK) equation.

More important is to realize that those three essentially equivalent models predict the volume fraction *f* converted as a function of time *t* in a very large specimen, i.e. boundary effects are ignored and it follows that crystallites nucleate homogeneously throughout the bulk and grow at a constant rate under interfacial control. These models represent the kinetics of a solid state phase transformation as a process of nucleation and growth of a product phase at the expense of the parent phase. The original approach is only valid for random homogeneous nucleation and isotropic growth, but in a modified form it was shown to be applicable for continuous cooling [2] and heterogeneous nucleation [3]. The most important concept in these latter models is that of extended volume, i.e. the volume of the new phase that would have been formed if there is no interference from other nuclei.

Nevertheless, this concept has been used very successfully but it breaks down under critical examination, for non-diffusional transformation or under thin film conditions. Also, in recent times it has been demonstrated convincingly, albeit not systematically, that in many situations of phase transformations such a simple Newtonian concept does not apply and possibly interfaces do not move continuous in time but in a jerky-type fashion, i.e. not in accordance with Eq. (5.1) when downsizing the observations to a smaller scale. It should be pointed out that the experimental conditions required to observe jerky-type motion are utmost demanding since criteria of high spatial and time resolution have to be met. It is therefore not surprising that the details of the jerky nature of the transformation has gone unnoticed for a long time. With the novel developments in instrumentation it is relevant to revisit the JMAK equation again and ask the question whether and when it will break down and at which length scales? Recent evolution of this setup on the speed of in-situ signal processing, allows us to study the dynamics of phase

changes with an enhanced temporal resolution. In our work we combine a heating stage and electron-back scattering diffraction (EBSD), resulting in in-situ scanning electron microscopy (SEM) observations of microstructural changes [4–8].

To test the hypothesis that JMAK will break down we concentrated on ferrite-austenite phase transformations in steel. New generations such as Dual-Phase, TRIP and TWIP achieve mechanical properties from particular mixing of e.g. austenite and ferrite. Therefore, theoretical tools to investigate and predict the transformation interfaces have become increasingly important and with increasing complexity the need to validate the kinetics increases. In addition, in-situ observations of dynamics provide necessary physical insight into the nature of transformations.

In most of the theoretical approaches an interface is reduced to a mathematical surface, characterized with variables and parameters as interface thickness, trans-interface diffusivity and interface binding energy [9]. The speed of phase boundary movement in steel has been reviewed by several authors with in-situ experimental techniques as optical microscopy [10], confocal laser microscopy [11] and dilatometry [12,13]. As every applied technique has its own unique advantage with respect to imaging speed, field of view or sampling volume, information on the crystal orientation cannot be retrieved simultaneously. In the work presented here, we make use of the strength of EBSD to accurately determine the phase front within sub-micron error, combined with the measured crystal orientation of the parent and daughter grains. This allows in-situ observation of nucleation and phase front movement, followed by reverse transformation, i.e. from ferrite to austenite and back to ferrite. For all the microscopy techniques listed above, including EBSD, the derived phase boundary velocity is that of the free surface of the sample; and limited to a 2D projection of the (3D-) phase boundary.

In particular, we concentrate on the nucleation of a new phase and the mobility of the interphase boundary during transformation. The experimental method to perform EBSD at high temperatures is presented, together with a novel analytical technique to quantify interphase boundary movement.

The material selected for this in-situ investigation is steel of grade S355, with specifications of chemical composition: maximum 0.24 wt.% C and a maximum of 1.6 wt.% Mn. Energy-dispersive X-ray spectroscopy (EDS) measurements showed a composition containing Carbon, 0.94 wt.% Mn and 0.4 wt.% Si. The onset of transformation to austenite can be expected at 750 ± 10 °C (Ac1), and should be completed around 911 ± 10 °C (Ac3) [14].

5.2 Nucleation of austenite

In-situ observed nucleation of austenitic phase is shown in Fig. 5.1. Nucleation was seen occurring either at quadruple junctions or on grain boundaries. Solid (blue) circle indicates nucleation at junctions and dotted (blue) circle points at grain-boundary nucleation.

The ratio of the energy barrier for heterogeneous nucleation to the energy barrier for homogeneous nucleation can be represented by a so-called shape factor [15]. With a conservative estimation value of 0.8 J/m^2 [16] for the austenite-ferrite phase boundary energy, and 1.11 J/m^2 [17] for the ferrite-ferrite phase boundary (pure Fe), calculation leads to a value for the ratio of 0.13 and 0.03 for nucleation on grain boundary and junction, respectively. A lower value of 0.6 J/m^2 [15] compared to 0.8 J/m^2 for the austenite-ferrite phase boundary energy, results in even lower ratios. In other words: it means that the barrier for heterogeneous nucleation would be approximately 8 or 33 times lower than for homogeneous nucleation. As expected, ratios of these magnitudes make homogeneous nucleation very unlikely and heterogeneous nucleation at junctions are preferred over heterogeneous nucleation at grain-boundaries.

This specimen was heated from 650 °C with a rate of 3 °C/min, whereby the first austenite grains were detected at 840 °C. Since a relatively small area is considered, the transformation could have started earlier, somewhere outside the observed area. The majority of the grains was seen to have the Kurdjumov-Sachs Orientation Relationship (K-S OR) with at least one neighboring ferrite grain: $(111)_{fcc}$ || $(110)_{bcc}$; $[0\bar{1}1]_{fcc}$ || $[1\bar{1}1]_{bcc}$. This is due to the lower nucleation barrier for the formation of grains with special orientation relationships. This observation is in line with the observations of the ferrite-austenite phase transformation in Fe-Ni alloys, where both the Kurdjumov-Sachs and Nishiyama-Wasserman $(111)_{fcc}$ || $(110)_{bcc}$; $[0\bar{1}1]_{fcc}$ || $[001]_{bcc}$ OR were observed [4,8] and EBSD observations of low carbon steel, where the Kurdjumov-Sachs OR dominated [18]. In the work presented here the growth was also observed to be mainly into ferrite grains, for which the austenite grains did not have the K-S OR. The nucleated grains were seen to prefer first to grow along grain boundaries, before encountering other austenite grains and junction and growing into ferrite grains.
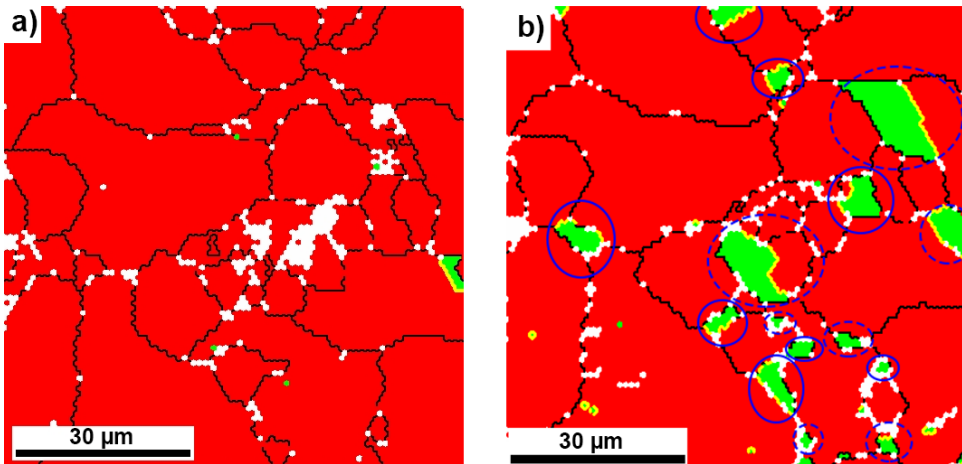
Figure 5.1. Heating from 650 °C with 3 °C/min. Phase OIM map from the same area: a) at 687 °C with ferrite (red) and austenite (green) grains; b) at 840 °C nucleation of new austenite grains. Highlighting shows nucleation at junctions (solid blue circle) and grain boundaries (dashed blue circle). Black lines indicate boundaries with misorientation angle > 5°. The bold yellow line indicates interphase boundaries that fulfill the Kurdjumov-Sachs orientation relationship.

5.2.1 Hesitating phase transformation

In another experiment the sample was heated to 800 °C with 10 °C/min, followed by heating to 820 °C with 2 °C/min. Austenite grains were already visible on the first scan at 700°C, and at 750 °C three more austenite grains had nucleated. A large amount of ferrite grain recrystallization was observed at 814 °C, as shown in Fig. 5.2. Instead of new austenite grain nucleation, the size of two of the austenite grains had decreased and one of these grains disappeared. The driving force for recrystallization seems to have increased during the heating. The reverse transformation can be assisted by a change in the carbon gradient. Carbon diffusion from the phase boundary into the austenite grain can cause a local carbon depletion zone. The drop in carbon concentration in this binary interphase temperature range, makes the ferrite phase more favorable.
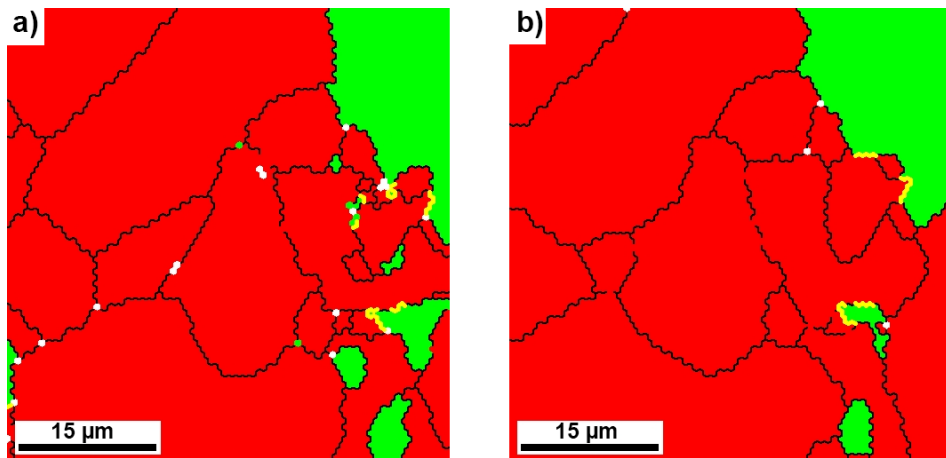
Figure 5.2. Phase OIM maps from the same area of specimen heated to 800 °C with 10 °C/min, followed by heating to 820 °C with 2 °C/min. ***a)****: Map at 750 °C showing ferrite (red) and austenite (green).* ***b)****: At 814 °C recrystallization of parent ferrite grains, and reverse transformation of the initial austenite grains to ferrite. Black lines indicate boundaries with misorientation angle > 5°. The bold yellow line indicates interphase boundaries that fulfill the Kurdjumov-Sachs orientation relationship.*

On a third specimen the first nucleation was noticed at 895 °C. Together with the previous observations, i.e. transformation at 840 °C and below 700 °C, it can be concluded that surface transformation deviates from the expected bulk transformation temperatures. These starting temperatures are probably influenced by the history of the material such as heating ramp and holding time at certain temperatures, and the presence of a high-energy interface at the extreme surface.

5.3 Velocity of moving interphases

The strength of EBSD is the accurate determination of the phase front within sub-micron error, combined with the measured crystal orientation of the parent and daughter grains. In this work a novel analytical method was developed to derive the velocity of the phase interface from the EBSD phase maps. In this method partly transparent phase maps were first overlaid in such a way that the junctions in the consecutive maps were approximately at the same position. The position of a relative straight phase boundary, which was often found between two junctions, is determined by the average of two parallel straight lines which constrain the most

forward and backward position of the interphase boundary. The technique is schematically demonstrated in Fig. 5.3, where the dashed line represents the average interphase boundary position. The operation was repeated for each successive map, whereby all new lines were drawn parallel to the initial phase boundary. The absolute differences between the average phase boundary positions are representing the boundary position evolution in time. In this way the dynamic behavior could be monitored for the time intervals where these boundaries remained near straight, with a clear growing direction.
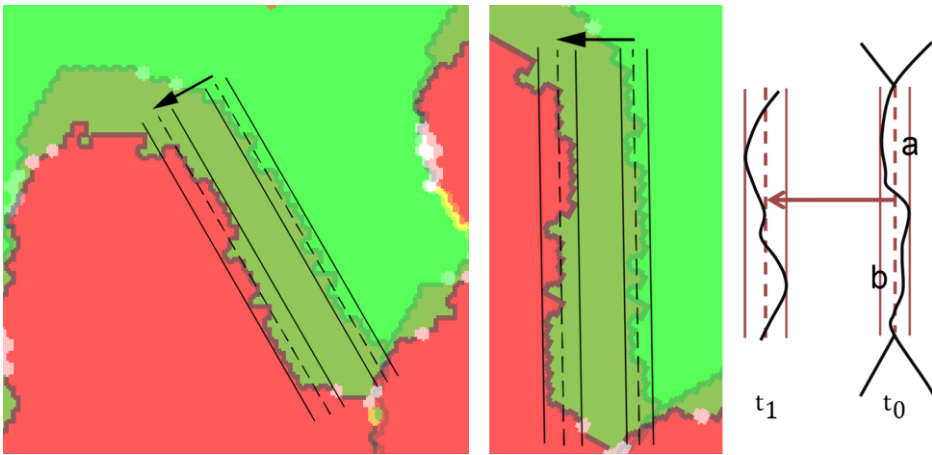

Figure 5.3. Interphase boundary position determination on two overlaid successive maps. In schematic form on the right side: t_0 is the initial boundary position, defined as the average of the difference between parallel lines a and b.

5.3.1 Velocity of growth front during heating

We applied the aforementioned novel method for interphase boundary position determination on austenite grains, which had different misorientations with respect to the ferrite parent grain. These misorientations and growth directions are indicated in Fig. 5.4. The obtained interphase boundary position as a function of time is shown in Fig. 5.5. The *average* velocity during this trajectory is listed in Table 5.1. The 48° misorientation interphase boundary moved with almost equal distance on every consecutive map, resulting in an average speed of 4.0 ± 0.2 nm/s. Then it made a sudden jump between two scans, as Fig. 5.4 b) shows. It is possible to give an estimate of the lower limit of this jerky motion jump of 40 - 90 nm/s.
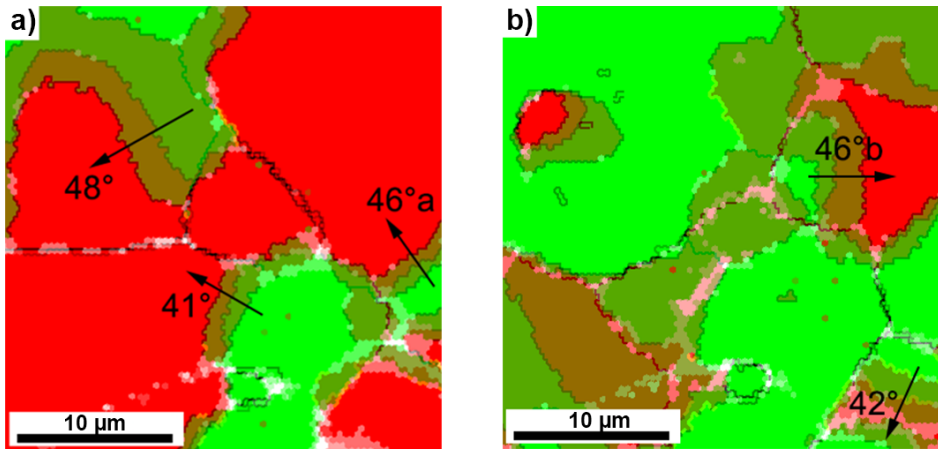
*Figure 5.4. Heating from 820 °C with 1.5 °C/min. Overlaid phase maps for **a)** early stage of transformation at around 835 °C, and **b)** nearly full transformed around 847 °C. Ferrite displayed in red and austenite grains in green. Growth directions are indicated by the black arrows, together with the grain misorientation angles.*
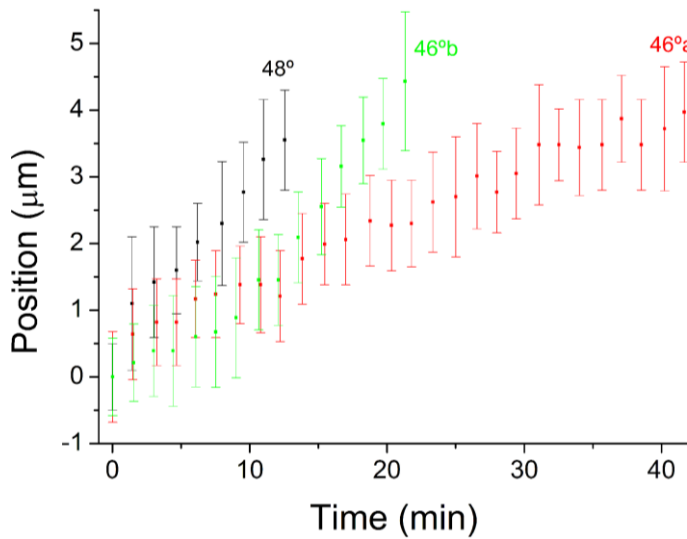

Figure 5.5. Interphase boundary motion during heating with 0.5 °C/min for several interphase boundary angles.

Table 5.1. Average speed of the interphase boundary during heating with 0.5 °C/min, for several parent-daughter interphase boundary angles as indicated in Fig. 5.5.

Misorientation (˚) (± 0.5)	Average speed (nm/s)
48	4.0 ± 0.2
46 a	1.5 ± 0.2
46 b	3.3 ± 0.2
42	2.5 ± 0.2
41	1.4 ± 0.2

For the determination of the velocity of the interphase boundary, the position of the boundary itself was averaged. As illustrated in Fig. 5.2, the boundary is not straight. When the interphase boundary shifts, it does not maintain a similar waviness and roughness. Fig. 5.6 shows the evolution of the interphase boundary shape. Clearly rough and wavy fronts as in a) c) f) can be discriminated from relatively straight ones like e) and g).
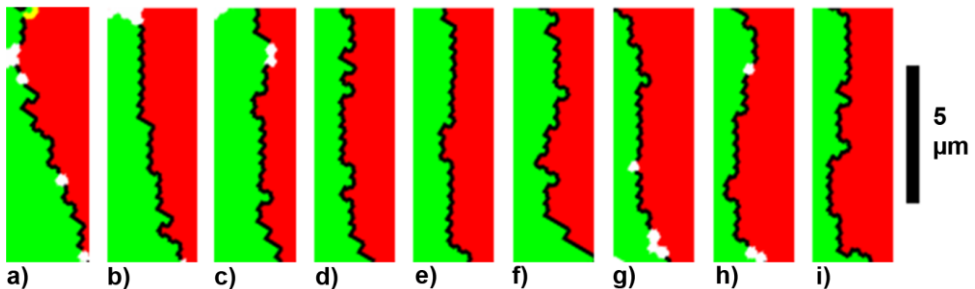

*Figure 5.6. Snapshots of a ferrite-austenite phase front as it propagates trough the ferrite parent grain (red). The time between the snapshots is 85 seconds, while a heating ramp of 0.5 °C/min was applied. Frame **a)** is taken at 831 °C; **i)** at 838 °C.*

Besides the crystal orientation, interphase boundary movement and roughness, also the phase fractions as a function of time can be determined from the EBSD maps. The increase of the fraction of austenite during heating with 0.5 and 1.5 °C/min, is shown in Fig. 5.7.

Using the general mathematical form of the JMAK equation of Eq. (5.1) the reaction rate indicated by factor n can be derived by the determination of the

slope of ln [-ln (1 – f(t))] vs. ln (t). A value of n = 4.8 ± 0.1 was found for heating with 1.5 °C/min. However, two stages of growth with different speeds were observed when heating with 0.5 °C/min. First stage n = 1.39 ± 0.03, and second stage n = 4.5 ± 0.1. Below 840 °C the main contribution to the increase of the austenite fraction is due to the fact that an existing austenite grain extends along the grain boundary. The jump in fraction of austenite at 840 °C (time = 35 minutes) corresponds to the rapid interphase boundary movement of the grain with 48° misorientation at the top left of Fig. 5.4. This event also marks the onset of the second stage of transformation with higher reaction rate. The contribution to the fraction of this second stage is a summation of both steady growth and boundary jumps. Steady growth and jumps were also observed for heating with 1.5 °C/min, however this did not result in two stages of growth in the austenite fraction. The higher reaction rate and the limited temporal resolution, already disables to visualize the individual contribution of the two processes.
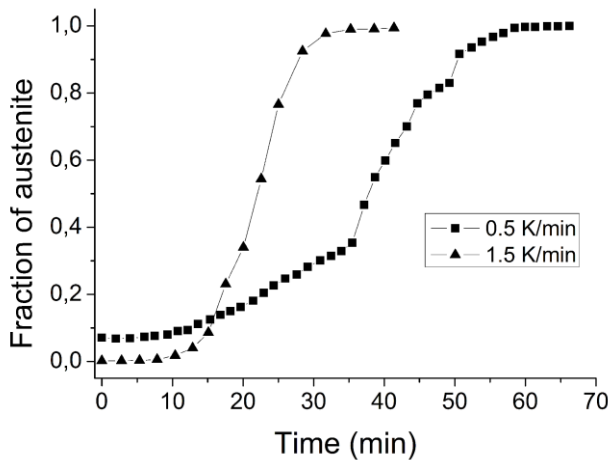

Figure 5.7. Austenite fraction versus time shows JMAK behavior for heating with 1.5 °C/min, and two-stage transformation behavior for heating with 0.5 °C/min.

5.3.2 Velocity of growth front during cooling

A fully austenitic sample was cooled from 860 °C with a cooling rate of 1 °C/min. The first ferrite was observed at 801.7 °C. The decreasing fraction of austenite during cooling also shows JMAK behavior. The absolute value of $n = 18.7 \pm 0.6$ is much larger compared to the found value of $n = 4.8 \pm 0.1$ for heating with 1.5 °C/min. Although the temperature ramp is smaller, the back transformation from austenite to ferrite is much faster. Nucleation of the ferrite grains occurred outside the scan area. The first two incoming grains moved along the austenite grain boundary, similar as interphase growth during heating. At 783 °C a ferritic grain is penetrating the center of an austenitic grain, as shown in Fig. 5.8, for which jerky motion was observed. The mean velocity was ranging between 5.0 ± 0.2 and 6.4 ± 0.2 nm/s (Table 5.2). The precise dynamics of this accelerated stage could not be observed due to limited number of scans. Estimation of the lower limit of the speed yields about 130 nm/s. It is concluded that jerky motion is thus also observed during cooling.
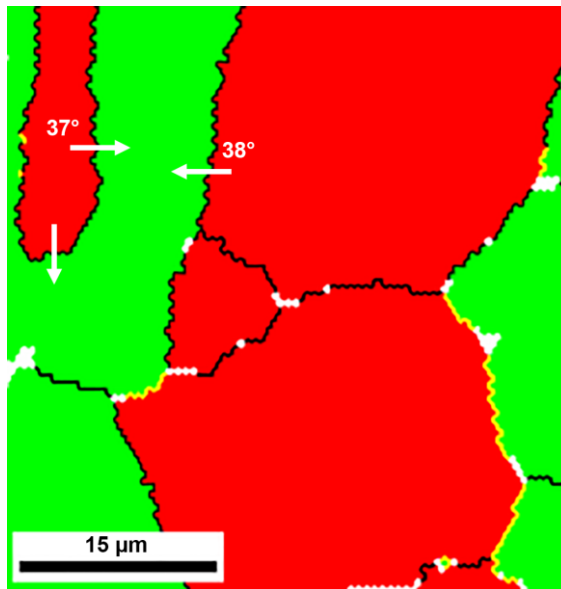

Figure 5.8. Growth of ferrite (red) into parent austenite (green) grain. Directions are indicated by the white arrows together with the interphase boundary misorientation angles. Jerky motion downwards with about 130 nm/s. Cooling from 860 °C with 1 °C/min, the first ferrite was observed at 802 °C.

*Table 5.2. Average speed of the interphase boundary during cooling with
1 °C/min, for several parent-daughter interphase boundary angles.*

Misorientation (˚) (± 0.5)	Average speed (nm/s)
38	6.4 ± 0.2
37	5.0 ± 0.2

5.3.3 Velocity of interphase front at constant temperature

In the aforementioned experiments the temperature was increased at constant rate (isochronal) in order to reveal the nucleation sites and dynamics of interphase growth. The following isothermal experiment was performed to study these phenomena in quasi-static conditions.

The specimen was heated up and kept at 820 °C for 20 minutes. Thereafter heating continued to 840 °C with 0.5 °C/min. First small changes started to occur at 835 °C. Although a new grain nucleated between 830 °C and 835 °C, very little growth took place in the following 37 minutes afterwards. Austenitic grain growth became more pronounced at 840 °C. Two new grains nucleated, one after 17 minutes and one after 25 minutes. As observed before, expansion of the austenite phase took place mostly along the grain boundaries. At this temperature a ferrite grain became surrounded by austenite grains. As shown in Fig. 5.9, the austenite grains grew radial inwards with small steps. Often a step was formed on the interphase boundary, followed by boundary growth along the step (demonstrated in Fig. 5.9, c) - e)). On a few occasions also reverse transformation took place along the same step, to be succeeded again by ferrite-austenite transformation. The mean velocity of the inwards moving interphase boundary ranged between 0.4 ± 0.2 and 1.7 ± 0.3 nm/s, as displayed in Table 5.3. No clear correlation can be seen between the average velocity and the misorientation between the parent-daughter interphase boundaries. It was observed that twin daughter fractions grew slightly faster.

A new grain nucleated on a grain-boundary while heating to 845 °C. This grain had the K-S OR with the ferrite grain on one side of the nucleus, but grew mostly in the direction opposite to this OR in the ferrite grain on the opposite side which did not have the K-S OR. As expected the incoherent interphase boundary which does not have the K-S OR, provides a greater driving force to move this

interphase boundary at a higher mean velocity, than the semi-coherent K-S OR boundary.
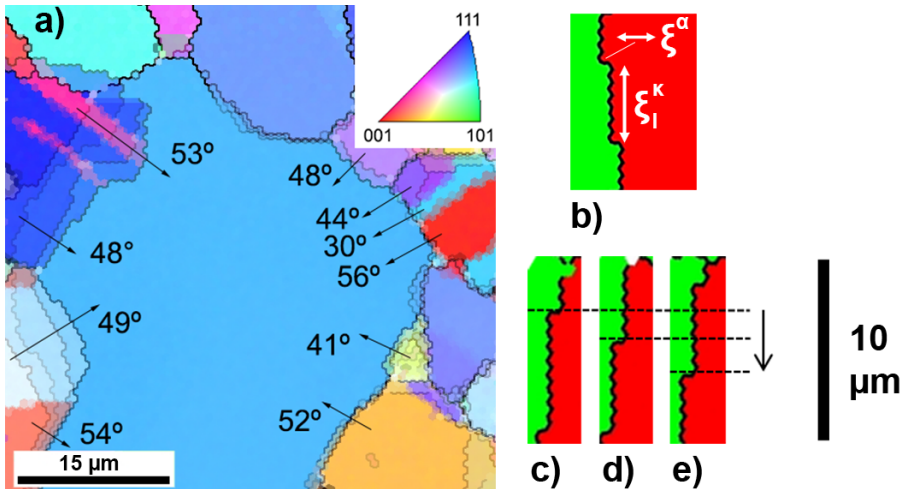
*Figure 5.9. **a)** Overlaid [001] inverse pole figure maps indicating interphase boundary growing directions and boundary misorientation at a constant temperature of 840 °C. The large grain in the center is ferritic, and surrounded by new austenite grains. **b)** Ledge step ξ^{α} equal to scan step size of 0.75 µm, and ledge correlation length ξ_l^{κ}. **c), d), e)**: Section of the 49° interphase boundary at 840 °C, time between scans is 65 seconds. Recorded expansion of the interphase boundary ledge along ξ_l^{κ} with two steps of 1.5 µm.*

Table 5.3. Average speed of the interphase boundary at constant temperature of 840 °C, for several parent-daughter interphase boundary angles.

Misorientation (°) (± 0.5)	Average speed (nm/s)
54	0.4 ± 0.2
53	1.7 ± 0.2
49	1.5 ± 0.2
48	1.4 ± 0.2

5.4 Phase transformation memory[*]

So far, we studied phase transformations during one thermal cycle per sample. Nucleation of a new phase to the the full phase transformation can span easily 50-100 °C, as seen in Sections 5.2 & 5.3. Low heating and cooling rates in the order of 1 °C/min have been used to be able to study the phase change in a controlled mode. Multiple heating cycles can be performed on the same sample, but would be very time consuming. In order to continually study migration of the interfaces, the recently introduced cyclic partial phase transformation (CPPT) approach [19] can be folowed. In a CPPT route, the temperature is cycled in such a manner that both α and γ phases are present. The transformation proceeds with back-and-forth migration of α/γ interfaces. Using this approach, a so-called 'stagnant stage' is reached. Depending on the composition of the material (i.e. the amount of Mn), this stagnant stage can span only several tens of °C. The material selected for the following experiment is a medium Mn steel with a nominal composition of Fe-0.056C-2.0Mn (wt.%).

Following the procedure of the previous sections, the initial ferritic steel is heated inside the electron microscope. After the first phase transformation, the specimen is kept in the stagnant stage. In this stage, the temperature is cyclically increased and decreased with a slow rate of 1 °C/min. within a temperature interval < 30 °C. Within this interval, the temperature was brought up until the microstructure was fully austenitic. During cooling down a mix of ferritic and austenitic grains was obtained. With further cooling the fraction of ferrite increased until all austenite was transformed. Thereafter the sample was heated and the inverse took place, i.e. the fraction of austenite increased. This cycle was repeated six times. The obtained microstructure at each end of the temperature interval, i.e. fully ferritic are austenitic, is shown in Fig. 5.10. The map on the left of Fig. 5.10a shows the IPF map of ferrite at 800 °C. As the map size is 200x100 μm^2, it can be seen that the grains have a size in the order of 20 μm. Upon further heating to 814 °C, a full austenite structure is obtained with grains ranging from 20 to 100 μm (Fig. 5.10a, right). After back transformation to ferrite, we see the ferritic grains have become courser, with grain sizes in the order of 20 to 60 μm. Coursening of the microstructure during a heating is a common behavior, as the history of the starting microstructure (obtained during the steel manufacturing process) is erased.

---

[*] *The work presented in Section 5.4 is part of a collaboration with the TU Delft, and will therefore also be placed in the PhD-thesis of Hussein Farahani.*

Apart from the grain size, we observe that the transformation to austenite after each cycle leads to an almost identical microstructure. One can see that the same grain dimensions, crystal orientations and also twin boundaries return, even after the 6th transformation cycle (Fig. 5.10f, right). The twins are observed in austenitic phase, e.g. in the pink grain on the right side of the map, by the characteristic double straight boundaries with identical misorientations. The ferritic microstructure is more subject to variations, although almost the same microstructure is observed at the 4th and 5th transformation cycle (Fig. 5.10 d) and e), left).

The origin of this 'phase transformation memory' is not known yet. To our knowledge, this behavior has not been reported in literature. As we have discussed in the previous sections, the two phases can have a coupling through orientation relationships such as the Kurdjumov-Sachs or e.g. Nishiyama-Wasserman. However during the phase transformation from austenite to ferrite, the microstructure is altered: during the occurring ferrtic grain coarsening, the information of the austenitic grain structure should disappear. The origin of the transformation memory might be found in the chemical composition of this steel. The fair amount of 2% of Mn could play an active role during the transformation. It is known that the Mn can have a pinning effect on the phase boundary [20–23]. We hypothesize that the Mn, perhaps together with remaining C, resides on the grain boundaries of the austenitic microstructure. Upon transformation to ferrite, the mobility of the phase boundary might be higher than the Mn. The phase boundary might move along, leaving enrichments of Mn in the new ferritic microstructure. During back transformation to austenite, the Mn enrichments can determine the boundaries of the new formed austenite grains.

	Ferrite	**Austenite**

a) Starting microstructure and first phase transformation to austenite

b) 2nd transformation cycle

c) 3rd transformation cycle

d) 4th transformation cycle

e) 5th transformation cycle
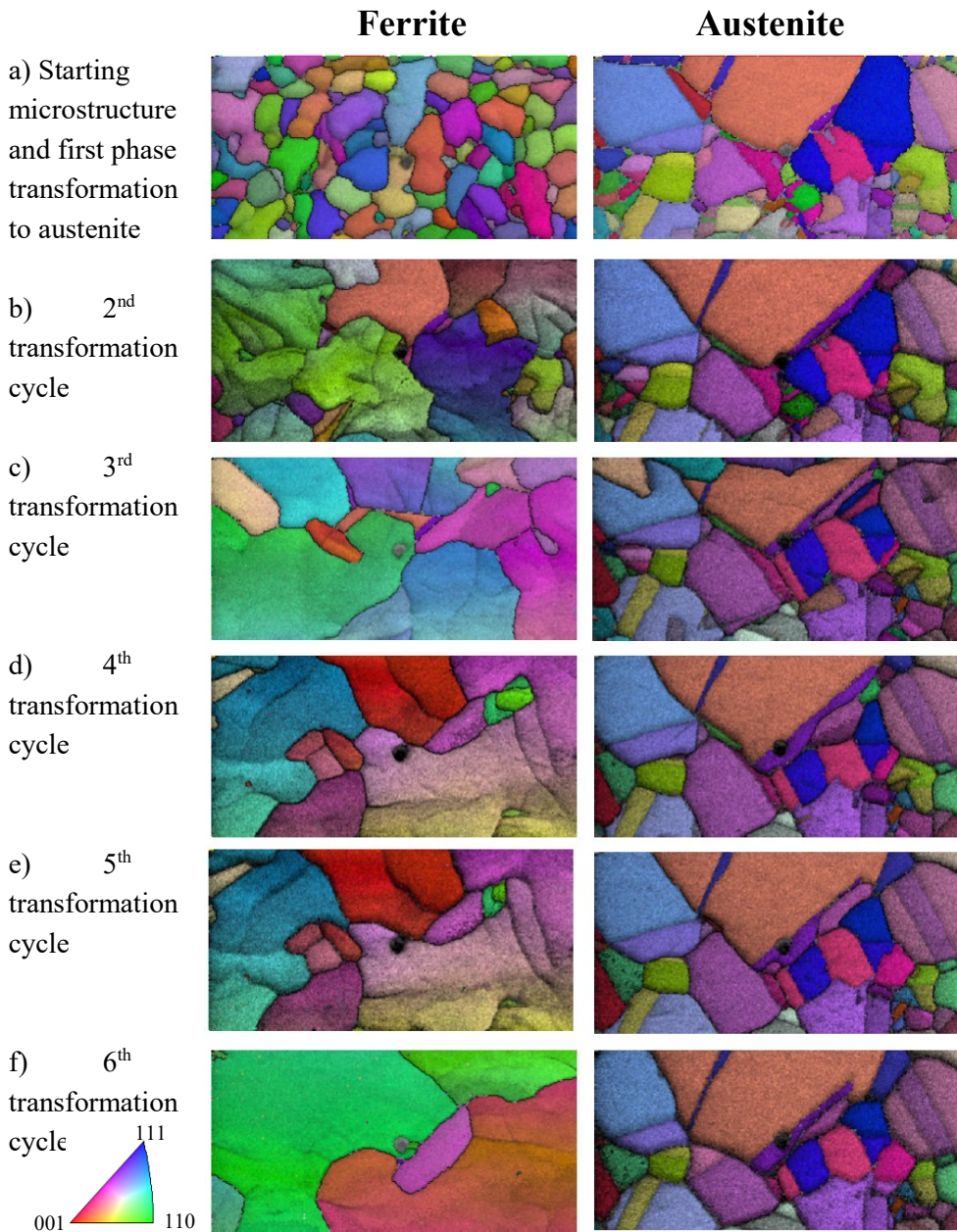
f) 6th transformation cycle

Figure 5.10. [001] Inverse Pole Figure combined with image quality maps made in-situ from the same area during cyclic heating. **a)** *800 °C ferrite (F), 814 °C austenite (A);* **b)** *797 °C (F), 830 °C (A);* **c)** *813 (F), 832 (A);* **d)** *806 (F), 833 (A);* **e)** *829 (F), 839 (A);* **f)** *819 (F), 838 (A). Map size is 200x100 μm².*

5.5 Details on grain-boundary and heterophase mobility

The importance of interfaces, either grain-boundaries or heterophase interfaces is determined primarily by their inherent inhomogeneity, i.e. the fact that physical and chemical properties may change dramatically at or near the interface itself. As a result of these sharp gradients an isotropic bulk solid may change locally into a *highly anisotropic medium*. Interfaces between different crystallographic structures or different bonding, such as those between metals and carbides, are of a special kind. Experimental and theoretical work has been carried out in recent years on model systems to understand the *static structure* of these interfaces. These model systems are usually well-defined simple interfaces, which are boundaries with known orientation, high symmetry, between simple, known constituents. The hope is that general concepts governing adhesion, structure, chemistry, mechanical behavior, and their interdependence can be elucidated.

Boundary phenomena usually take place in a very narrow region, of the order of a few nanometers where the two grains meet. For this reason the structure of grain boundaries has been investigated extensively in the last decade, both experimentally and with the help of computer simulations. Such calculations contributed very significantly to our understanding of general features of grain boundary structure even though they were usually made using pair-potentials. While this is a crude approximation for most materials, significant results of these studies have often been found to be very little dependent on interatomic forces used and are common either to whole classes of materials or certain types of grain boundaries (for reviews see [24]).

One general result of this type is the structural unit model which relates structures of boundaries corresponding to different misorientations of the grains. The model was originally developed for periodic tilt boundaries. It was later extended to twist boundaries [25] and was generalized to non-periodic irrational tilt grain boundaries [26]. In the case of special boundaries the structures are composed of mixtures of different structural elements, and described in displacement- shift-complete (DSC) dislocations related to the coincidence site lattice (CSL). We will come back to CSLs later.

We have to admit that almost all these studies concentrate on the static structure of 2D defects whereas most of the properties of materials depend on the dynamic and kinetic behavior of defects. With the advent of *in situ* electron microscopy the field extended significantly into kinetics and dynamic studies of

interface mobilities, mainly focusing on recrystallization and annealing in single phase systems. In any polycrystalline material junctions between grain-boundaries are one of the most prominent defects and a relevant question is whether these defects are controlling the overall grain-growth phenomenon upon e.g. annealing and recrystallization. However, such a study will become even more exciting if also phase transformations are involved since the interplay between junctions and grain-boundaries may affect the kinetics of nucleation and growth of phases and grains.

Interestingly enough the system under study in this chapter comprises both the important defects of grain-boundaries and of heterophase interfaces with junctions and here we study the mutual correlations through *in situ* scanning electron microscopy. In a 3-D arrangement of grains we may distinguish in total 3 topological defects, i.e. besides the grain-boundary plane we have triple lines and even quadruple points where four grains meet. These defects are indicated in Fig. 5.11 taken from the paper by R. Phelan and Dennis Weaire 'the Kelvin problem' [27], also published as 'Cellular Structures in Three Dimensions' [28].
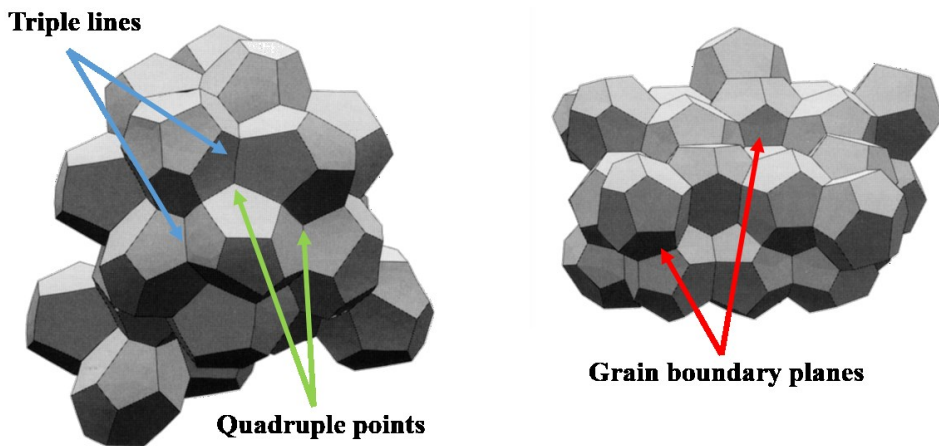

Figure 5.11. Examples of possible polycrystalline structures, reproduced from R. Phelan and Dennis Weaire 'the Kelvin problem' [27], also published as 'Cellular Structures in Three Dimensions' [28].

In our work, dealing with kinetics and dynamics, triple lines are in particular of interest since movements of boundaries due to phase transformations and grain-growth occur along the line of intersection of the boundaries, which are called 'triple lines'. Obviously there exists a large variety and broad distribution of the

geometrical details of a triple line. This is so due to the geometrical degrees of freedom to construct a topological defect like a grain-boundary or a heterophase interface.

In total a grain-boundary has 5 degrees of freedom (3 rotations, plus 2 from the boundary plane normal). For a heterophase interface we might even add another set of 2 variables, i.e. making it in total 7 degrees of freedom, reflecting translational expansions/contractions along and perpendicular to the interface plane. As a consequence of all these degrees of freedom, a triple line is defined at least by 12 independent geometrical parameters whereas a heterophase interface needs 18 for a complete characterization. Even more impressive, a quadruple point requires at least 21 independent geometrical parameters for a full characterization in a point where 4 triple lines, 4 grains and 6 boundaries meet. These considerations show that a full characterization of these topological defects seems to be hardly feasible by any electron microscopy technique producing only a project view in 2D. A major drawback in the following is in particular the uncertainty about the geometrical/crystallographic details about the various interface planes making up the junctions. Focused Ion Beam – FIB [29] may help to reveal the 3D configuration to a certain extent but not under dynamic *in situ* conditions of moving boundaries, i.e. only as a post-mortem technique.

Let's turn what these *in situ* experiments have shown us. In Fig. 5.12.we see the growth of austenite into ferrite. The experimental details are described in Section 5.3.1. The austenite area on top first expands over the grain boundary towards the triple junction of the ferrite grains. The next map shows that the austenite area has reached the junction (see Fig. 5.12b). At this moment we observe that a part of the interphase on the right side of the austite area has a suspected special boundary with a misorientation of 42.7, as indicated with a yellow line (we will address this boundary later). The austenite does not exceed this interphase boundary, but instead thickens at the left side into the left ferrite grain (see Fig. 5.12c). Fig. 5.13 shows the schematic representation of the two phases at the triple line.
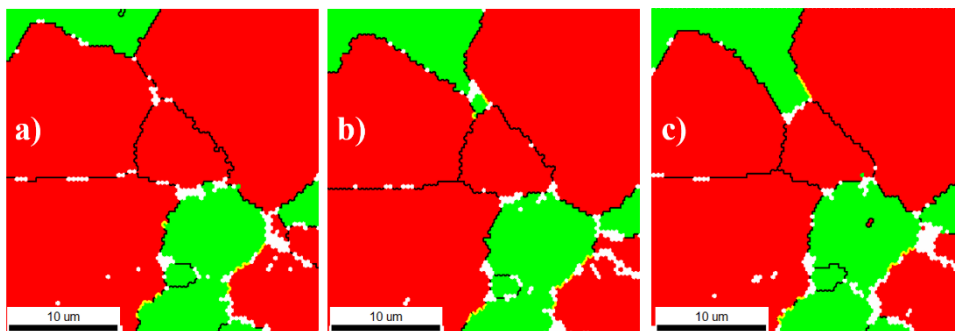
*Figure 5.12. Growth of austenite (green) area at the top, into ferrite (red) on phase OIM maps. Maps made at: **a)** 830.5 °C; **b)** 831.5 °C; **c)** 832 °C. The bold yellow line on the right of the austenite area at the top indicates a suspected special interphase boundary, with a misorientation of 42.7°.*
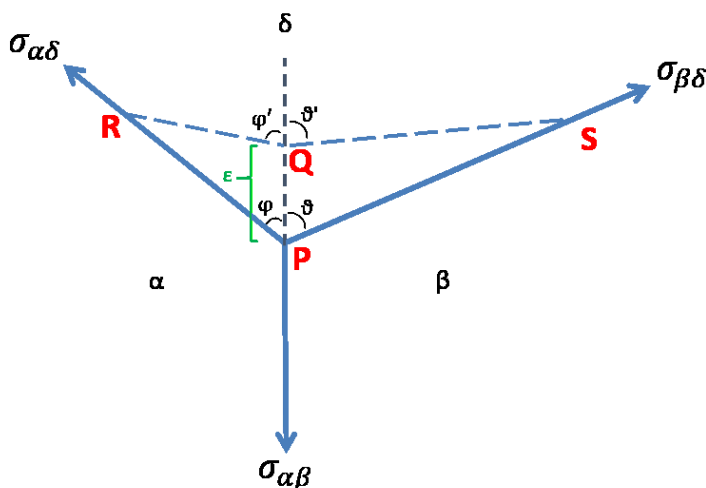

Figure 5.13. Schematics of the triple lines (indicated by the solid blue lines) seen in the experiment. Another line is assumed to run in 3D perpendicular to the figure. σ_{ij} represents the tension acting on the junction along the interfaces between the various phases in the directions as indicated. In the comparison with the experiment as shown in Fig. 5.12, $\sigma_{\alpha\beta}$ represents the interfacial tension along the grain-boundary, i.e. called γ_{GB} in the following whereas $\sigma_{\alpha\delta}$ and $\sigma_{\beta\delta}$ represent the interfacial tension γ_i along the heterophase interface between ferrite and austenite. Point P is the triple junction; α and β are the ferritic grains; δ is the austenitic grain at the top of Fig. 5.12.

Our analysis of the experimental observations is as follows. Obviously interfacial tensions and energies play a predominant role in the kinetics and we write, as it is usual done in physics, the velocity $\vec{v}$ as the product of mobility m and driving force $\vec{F}_d$, i.e.:

$$\vec{v} = m\,\vec{F}_d \tag{5.2}$$

The force fields along the interfaces are illustrated schematically in Fig. 5.13. The interfacial tensions along the boundaries act in such a way of shortening the boundary (along the line outwards).

At equilibrium, based on trigonometry we have

$$\sigma_{\alpha\beta} - \sigma_{\alpha\delta}\cos\varphi - \sigma_{\beta\delta}\cos\vartheta = 0 \tag{5.3}$$

or

$$\frac{\sigma_{\alpha\beta}}{\sin(\varphi+\vartheta)} = \frac{\sigma_{\alpha\delta}}{\sin\beta} = \frac{\sigma_{\beta\delta}}{\sin\alpha} \tag{5.4}$$

If all interfacial tensions are equal, it follows $\alpha = \beta = (\varphi + \vartheta) = 2\pi/3$. As expected this is all fine for liquids since the interfacial tension does not depend on the area, but not necessarily correct for solids. Only when the temperature is high enough and if the interfacial tensions are not a function of the area, the surface tension may be numerically identified with the surface free energy. In fact σ_{ij} may critically depend on the misorientation (coincidence site lattices (CSLs), orientation relationships etc.) leading to angular forces upon turning the interfaces in special crystallographic orientations with lower energy.

Suppose we displace the triple junction of Fig. 5.13 over a distance ε from the origin P to Q. The total energy dG change is the sum of the energy change leading to Eq. (5.3) and adding the angular contributions, i.e.:

$$\frac{dG_1}{L} = (\sigma_{\alpha\beta} - \sigma_{\alpha\delta}\cos\varphi - \sigma_{\beta\delta}\cos\vartheta)\varepsilon \; + \; \frac{\partial\sigma_{\alpha\delta}}{\partial\varphi}\varepsilon\,\sin\varphi \; + \; \frac{\partial\sigma_{\beta\delta}}{\partial\vartheta}\varepsilon\,\sin\vartheta \tag{5.5}$$

and at equilibrium

$$\sigma_{\alpha\beta} - \sigma_{\alpha\delta}\cos\varphi - \sigma_{\beta\delta}\cos\vartheta \; + \; \frac{\partial\sigma_{\alpha\delta}}{\partial\varphi}\sin\varphi \; + \; \frac{\partial\sigma_{\beta\delta}}{\partial\vartheta}\sin\vartheta = 0 \tag{5.6}$$

The first term of dG_1 / L in Eq. (5.5) depends on the distance PQ, i.e. ε. To arrive at the remaining terms in Eqs. (5.5) and (5.6), the change in energy due to

the orientation change of the αδ and βδ interfaces depends on RQ and SQ which for small angles can be written as a function of ε:

$$\frac{\partial\varphi}{\varepsilon} = \frac{\sin\varphi}{RQ}\; ;\; \frac{\partial\vartheta}{\varepsilon} = \frac{\sin\vartheta}{SQ} \tag{5.7}$$

and

$$\frac{dG_2}{L} = \left[\frac{\partial\sigma_{\alpha\delta}}{\partial\varphi}\partial\varphi\right]RQ\; ;\; \frac{dG_3}{L} = \left[\frac{\partial\sigma_{\beta\delta}}{\partial\vartheta}\partial\vartheta\right]SQ \tag{5.8}$$

The angular contributions are considered to be small in most cases for solid materials. However, for special boundaries, say of the CSL type and in case of orientation relationships, the situation might be completely different. Obviously the energy will change dramatically with a change in misorientation due to the angular force when a more coherent boundary is involved. In fact the interface tension will change very rapidly when the coherency is lost upon change in the misorientation.

In the analysis of our experimental observations (see Fig. 5.12) we set $\sigma_{\alpha\beta}$ equal to value of the grain-boundary energy γ_{GB} in ferrite, and $\sigma_{\alpha\delta} = \sigma_{\beta\delta} = \gamma_i$ the interfacial energy between ferrite and austenite. The angle φ is taken to be equal to ϑ, more or less according to the experimental observations.

The velocity of the junction can be written as (see Eq. (5.2) and Eq. (5.3):

$$v_t = m_t(2\gamma_i\cos\vartheta - \gamma_{GB}) \tag{5.9}$$

where m_t is the mobility of the junction. In steady state follows for a width λ of the heterophase:

$$m_t(2\gamma_i\cos\vartheta - \gamma_{GB}) = \frac{2\vartheta}{\lambda}m_i\gamma_i \tag{5.10}$$

with m_i is the mobility of the interface, or:

$$\frac{2\vartheta}{2\cos\vartheta - \frac{\gamma_{GB}}{\gamma_i}} = \frac{m_t\lambda}{m_i} = \Lambda \tag{5.11}$$

Since the dimension of GB mobility is different from that of the mobility of a junction and the ratio $\frac{m_i}{m_t}$ has the dimension of length, the above ratio Λ is dimensionless. Λ reflects the retarding or inhibiting effect of the junction on the interface velocity. A larger value of Λ does not affect the overall mobility and the

junction is not the controlling factor. For smaller Λ the junction becomes more important to consider as the determining factor.

Experiments indicate that at higher temperature $\gamma_i = 0.6 \, J/m^2$ [30], whereas γ_{GB} is calculated from the surface free energy of ferrite ($\gamma_{GB} = 1/3 \, \Delta G_{Sv}^{\alpha-Fe}$) and equal to $\gamma_{GB} = 0.8 \, J/m^2$. These input values lead to:

$$\vartheta = cos^{-1} \frac{\gamma_{GB}}{2\gamma_i} \tag{5.12}$$

or $\varphi + \vartheta = 96°$ (see Fig. 5.13), which is pretty close to the experimental observation in Fig. 5.12a of about 101°. The value of Λ is large and we may conclude that the onset of the mobility of the interface, reducing the grain-boundary length and tension, is not affected by the junction.

Nevertheless the situation changes if the movement proceeds. In fact we have observed that the interfacial tension becomes on one side influenced through a lock-in effect of the interface in a special orientation relationship of the CSL/orientation relation type. Obviously, the interfacial tension γ_i becomes larger than the γ_{GB} and the value of Λ becomes substantially smaller. It means that upon propagation the junction becomes the controlling factor and one expects that the direction of the movement will alter. In fact extending the CSL/orientation relationship interface with higher $\sigma_{\beta\delta}$ becomes less likely (also due to the abovementioned angular force fields involved, $\frac{\partial \sigma_{\beta\delta}}{\partial \vartheta} sin\vartheta$). Consequently it will be more favorable to extend along the interface without a special orientation relationship. This is precisely what was observed experimentally, i.e. the transformation front moves to the left.

We can analyze the situation in a bit more detail since the question arises whether ϑ across the interface between austenite and ferrite would suggest a special boundary and a special interfacial energy as is suggested above. ϑ is found to be 42.7° experimentally but does it indicate a special interface?
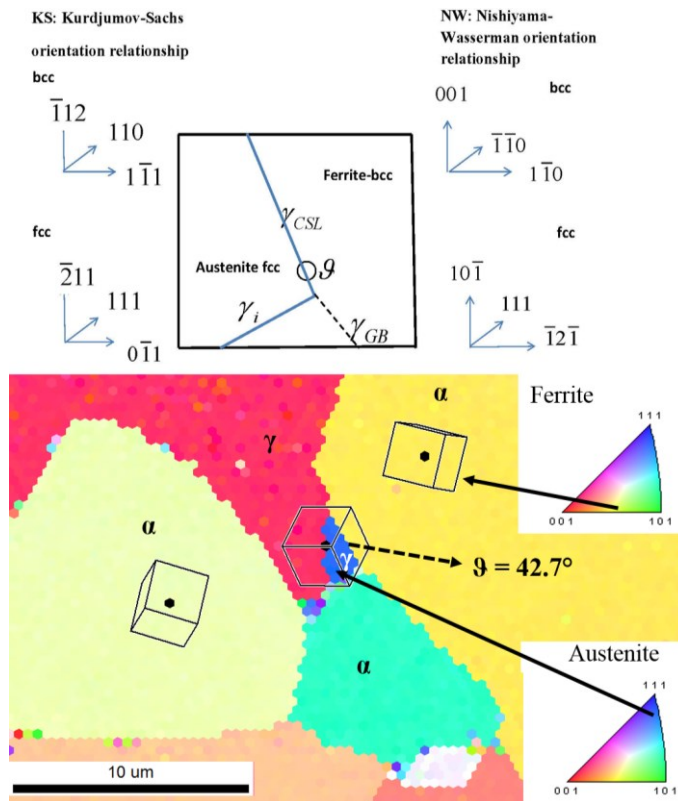
Figure 5.14. [001] IPF representation of the map of Fig. 5.12c. Indicated are the plane orientations parallel to the surface (in colour), and the phases ferrite by α and austenite by γ (the latter should not to be confused with the interfacial tension γ_i). Also shown is the schematic representation at the triple line, together with possible special orientation relationships. Axonometric unit cell projections to the surface plane are also indicated.

Cubic systems show a special (coincidence site lattice) CSL of a rotation $46.83@ <111>$ and $38.94@ <110>$; the former represent CSL $\Sigma 19b$, the latter CSL $\Sigma 9$. However the Kurdjumov-Sachs orientation relationship reads that the close–packed planes {111} of fcc are parallel to the close packed {110} planes of bcc and similarly the close-packed directions <110> and <111>, of fcc and bcc, respectively (see Fig. 5.14). Therefore we have to rotate the [111] to another <111>, say $[1\bar{1}1]$, over $\pm48.18°$ to the interface plane in austenite we observe

experimentally. The same is true for the rotation from [110] to [1$\bar{1}$0] in ferrite, i.e. ±90° leading to a total rotation over the interface of 41.82°, which is close to the experimental value of 42.66°.

Therefore we may conclude that the interface which appears during the propagation of the transformation front fulfills most likely a Kurdjumov-Sachs orientation relationship. Please keep in mind that for a Kurdjumov-Sachs orientation relationship an additional rotation of is necessary bringing the <110>$_{fcc}$ and <111>$_{bcc}$ in parallel and creating a so-called invariant line. This rotation over 5.26° will take place in the interface plane which is not be detected here. But, even in that case the interface is not a coherent interface since the six-fold symmetry of a {111} of an austenite–fcc will never match with the two-fold symmetry of the {110} ferrite-bcc planes. As a consequence even with a (Kurdjumov-Sachs or any other, like a Nishiyama-Wasserman etc.) orientation relationship, the interface will be a semi-coherent interface with regions of disregistry corresponding to a dislocation network, which contribute also to the interfacial energy/tension contribution in our analysis.

The conclusion which can be drawn is that when various interfaces and therefore various interfacial tensions are involved the kinetics of boundary movement is not a continuous process. The onset and nucleation phase might be quite different compared to the propagation phase. Indeed, local dynamical phenomena have to be analyzed when presenting a more detailed picture of boundary motion and boundary mobility.

So far our analysis concentrated on the driving force term in Eq. (5.2). Future analysis could also be focused on the mobility term, Eq. (5.2), which, in a thermally activated process, might be very much affected by impurities (in this particular case by carbon atoms). In this framework it is also relevant to examine the precise time window when both impurities and triple lines and quadruple junctions are moving at elevated temperature. Obviously the mobility of the junction will become temperature dependent and will depend on the activation energy of, say carbon atoms and the adsorption gradients between junction and interfaces affecting both $m_{i,t}$ and σ_{ij}. Better, i.e. more clean and neat experiments are needed to investigate and to unravel the separate contributions of these interrelated effects to the triple line- interface mobilities. *In situ* electron microscopy (both transmission and scanning) may have significant impact to this field of research because of the ability to provide simultaneously crystallographic and chemical information about the kinetics and dynamics at a local, sub-nm scale.

5.6 Discussion

We performed a careful literature search so as to place our findings in the right context. For decarburization experiments, with a macroscopic moving interphase front, an interface velocity between $0.01 - 0.1\ \mu m/s$ is reported [31] (but note: from austenite to ferrite). The velocities of the planar front that are ranged between sub-micrometer to nanometer per second [9]. It is shown [32] that ferrite growth under decarburization following parabolic growth kinetics. Schmidt et al. [33] used heating rates of 3 to 10 °C/s and found that the migrating austenite front in interstitial free steel covers a distance of about 200 micron in 1 second. An overview is listed in Table 5.4.

Table 5.4. Experimental values of mean velocities in ferrite-austenite (Fer.-Aus.) and austenite-ferrite (Aus.-Fer.) transformations.

Material	Transformation	Temp. ramp (°C/min)	Velocity (µm/s)	Technique	Ref.
Fe-4.2 at.% Cr IF-steel	Fer.-Aus.	5	0.33-7.6	Optical	[10]
	Fer.-Aus.	180-600	200	Confocal laser	[33]
Pure Fe	Aus.-Fer.	5-15	3.05	Dilatometer	[12]
Fe-0.01 at.% Cr	Aus.-Fer.	20	1.6	Dilatometer	[13]
Pure Fe	Aus.-Fer.	20	3.9	Dilatometer	[13]
Fe-0.76C-0.84Si	Aus.-Fer.	Isothermal	0.1-0.001	Post-Mortem	[31]

Overall the interphase boundary velocities in austenite-ferrite transformation are a little higher compared to the ferrite-austenite transformation, but still in the same order of magnitude. It is difficult to say to what degree the velocities derived in this work can be compared with respect to each other. The difference, however, is believed to be the result of the higher cooling ramp (1 °C/min) as compared to the heating ramp (0.5 °C/min) and undercooling. Velocities for the austenite-ferrite transformation in pure Fe and ultralow carbon steel have been reported (Table 5.4), with differences in heating rates, 1 °C/min used here opposed to 5 - 20 °C/min in literature, show velocities differing by a

factor 1000, i.e. nm/s in this work vs. $\mu m/s$ in literature. Post-mortem analysis of isothermal decarburization of Fe-C-Si steel, provided derived speeds of $0.1 - 0.01\ \mu m/s$ [13]. Low impurity content, together with high cooling speeds seems to result in phase boundary speeds in the order of at least $\mu m/s$. The discrepancy is probably not only due to the difference in heating rate, but also due to the decrease in solubility of carbon.

In a few rare cases growth speeds have been presented in literature for phase transformations in pure iron and steel. From dilatometry data an average speed of 3.05 $\mu m/s$ was found in the case of the austenite-ferrite transformation in pure Fe for cooling rates of 5 - 15 °C/min [12]. In similar experiments an average speed of 1.6 $\mu m/s$ was found for the austenite-ferrite interface of a Fe-0.01 at.% C at 20 °C/min cooling, as compared to 3.9 $\mu m/s$ for pure iron at the same cooling rate [13]. In the same paper a transition from diffusion-controlled growth to interface-controlled growth was discussed. Diffusion-controlled growth was attributed to the initial stages of transformations for cooling rates of 5-10 °C/min. Velocities of about 5 times smaller (~10^{-7} m/s) than for massive interface-controlled growth, were derived from the average grain size diameter of small grains.

In optical microscopy experiments the ferrite-austenite transformation of Fe-4.2 at.% Cr with 5 °C/min heating showed two stage transformation behavior with 0.33 - 0.75 $\mu m/s$ and a stage with 3.7 - 7.6 $\mu m/s$, respectively [10,34]. The two stage behavior was believed to be due to a change in driving force related to the phase transformation from the ferrite-austenite coexisting region to the austenite single phase region of the Fe-Cr alloy. This two stage behavior was also observed for heating at a rate of 0.5 °C/min. In the first stage the average velocity was 4.0 ± 0.2 nm/s, followed by a jump of 40-90 nm/s. The two stages presented in this work differ an order of magnitude, similar as observed in [34]. It is questionable whether the temperature of 840 °C is the actual transformation temperature for fully austenite (in [34] attributed as the driving force), as other grains made a jump later, or not at all.

The existence of both boundary morphologies, i.e. ragged and straight, indicates a jerky-type interphase boundary movement mechanism, of a smaller order than the resolution reported in Figs. 5.5 and 5.6. In fact all interfaces in our case seem to move in a jerky manner, i.e. observations reveal a segmental motion of the interface, where segment length, stagnation period and local velocity may vary. By this mechanism, the boundary roughens by small segments of the new phase moving forward. When the boundary has a certain degree of waviness and

roughness and therefore an amount of stored energy, a "jump" sideways reduces the boundary length.

We ask ourselves: What determines the characteristic time scale and what affects the characteristic length scale? As aforementioned it should be pointed out that the experimental conditions required to observe jerky-type motion are most demanding since criteria of high spatial and time resolution have to be met simultaneously. In the present experimental set-up we are limited in spatial and temporal resolution and to put the in-situ EBSD-SEM observation in perspective let us define the spatio-temporal resolution δ_{ST} as the product of spatial and resolution in time:

$$\delta_{ST} = \delta_S \otimes \delta_T \tag{5.13}$$

In our current FEG-Lyra Tescan the spatial resolution is about 4-6 nm when using accelerating voltages ranging between 15 and 30 kV. Although we have employed a Hikari super camera which can achieve a maximum of 1400 indexed points per second, the actual EBSD processing speed may still suffer if the indexation time per spot increases due to decreasing signal quality. A conservative number is indexation of 50 spots per second, with a typical step size of 0.4 micrometer, this results in $\delta_{ST} = 8.0x10^{-9}m\ s$. However to construct a 30x30 μm map (one frame) with these parameters requires indexation of 6380 points, which leads to $\delta_{ST} = 5.1x10^{-5}m\ s$. The time between successive scans was around 85 s. In comparison, in-situ TEM experiments (not EBSD but dark field/bright field observations) to date offer a time resolution of about 30 frames per second with a spatial resolution of sub-nm leading to $\delta_{ST} = 10^{-11}\ m\ s$ (at best).

As shown in Section 5.3.1, the *in-situ* observations at low heating rate of 0.5 °C/min reveal a splitting in transformation reaction rates. First a slow growth along grain boundaries and inward ferrite parent grains with $n = 1.39 \pm 0.03$, followed by large steps of the interphase boundaries resulting in $n = 4.5 \pm 0.1$. It can be concluded that the motion is far from continuous, neither on a macroscale as analyzed with the help of JMAK Eq. (5.1) or on a local scale as observed in our experiments (see Section 5.3). The results of Fig. 5.7 not only indicate that the heating rate is a process-determining factor here, but also demonstrate that in-situ HT EBSD is capable of providing insight in:

- trends at both micro- and macroscopic scales: even on a small area of 40x40 micron squared clear stages of nucleation, growth and saturation

can be observed, resulting in an austenite fraction curve with a typical
JMAK shape;
- local phenomena like two different transformation phenomena in time,
which would remain hidden in more volume averaging experiments,
e.g. by using X-Ray diffraction.

The competition between continuous motion and jerky type motion is
determined by the driving force. The argument, as has been pointed out by John
Cahn [35,36], here is that jerky type motion will take place below a certain critical
driving force whilst above a sufficiently large force field continuous motion will
always be possible.

For an infinitely flat interface the driving force to move the entire interface
will not be easily achieved in practice, whereas in case of a highly
thermodynamically diffuse interface, i.e. with a lot of a preexisting disorder along
the interface plane, any driving force will make it moving in a jerky fashion. In the
present case of heterophase interfaces as observed in the present case, with a
Kurdjumov-Sachs $(111)_{fcc} || (110)_{bcc}$; $[0\bar{1}1]_{fcc} || [1\bar{1}1]_{bcc}$ orientation
relationship the interface is at least semi-coherent.

In addition to the KS orientation relationship, growth was also observed
into ferrite grains, starting from austenite grains, for which the austenite grains did
not have the KS-OR. Nucleated austenite grains were seen to grow first
preferentially along grain boundaries in ferrite, before encountering other austenite
grains and triple junctions and growing into ferrite grains. As a consequence, based
on these geometrical arguments of semi-coherent ferrite-austenite interfaces and of
growth along general grain-boundaries (not coincidence-site-lattice CSL!) it is not
a surprise that the motion of the transformation front occurs in a step-wise jerky
motion. The 'disorder' of ledges, kinks along the heterophase interface and of
'roughness' along *general* (not special or favoured) grain-boundaries are the cause
of jerkiness, i.e. not continuous in time on a microscale as the JMAK-equation
(Eq. (5.1)) would predict on the macro-scale.

When the front is already 'disordered' before the transformation happens,
there is no physical reason to believe that the front will straighten out to a planar
configuration upon and after any transformation. It can be shown that it can be cast
in a simple, sufficient and necessary mathematical condition, namely: provided the
Gibbs energy change per unit of atomic volume $\Delta g_{\alpha\gamma} / \Omega$ is much larger than the
fluctuations in the interfacial or in the grain boundary energy between the ferrite

and austenite phase, $\Gamma_{\alpha\gamma}$, per unit of lattice step height, a continuous motion is expected, when the driving force is large, i.e. when

$$\frac{\Delta g_{\alpha\gamma}}{\Omega} > \frac{\Gamma_{\alpha\gamma}}{h_0} \, \varphi, \qquad (5.14)$$

where φ is equal to unity for an infinitely straight front and decreases to lower values for ragged configurations. Substituting the appropriate values for $\Delta g_{\alpha\gamma}/\Omega$ of $0.2 * 10^7$ J/m^3 at 840 °C, $\Gamma_{\alpha\gamma}$ of 600 mJ/m^2 [10] and h_0 of the order of sub-nanometer into Eq. (5.14) leads to the conclusion that a continuous motion is not expected in the present case, i.e. the transformation front advances not continuously but rather by the motion of steps, kinks, ledges for the case of KS-OR along the interface and roughening for transformations along grain-boundaries.

The physical picture which emerges from our experiments and these theoretical considerations is demonstrated in Fig. 5.9. Obviously the mean velocity will depend on the correlation length along the transformation front. Further the mean displacement of the front depends on the local correlation length, i.e. the local step height or roughness amplitude, say $\bar{\bar{\xi}}$, whereas the time involved depends on the range of interaction, say ξ^κ [37]. Since there will be only a physical correlation length when the jerky type regime is operational, i.e. below a critical driving force F_c above which jerkiness becomes unlikely, the correlation length scales, taking into account Eq. (5.14), with:

$$\xi \propto \frac{1}{|F_c - F|^\mu} = \left| \frac{\Delta g_{\alpha\gamma}}{\Omega} - \frac{\Gamma_{\alpha\gamma}}{h_0} \, \varphi \right|^{-\mu}, \qquad (5.15)$$

where μ is a critical exponent. The mean velocity can be written as:

$$\bar{v} = \frac{\xi^\alpha}{\tau_\xi} \propto \left| \frac{\Delta g_{\alpha\gamma}}{\Omega} - \frac{\Gamma_{\alpha\gamma}}{h_0} \, \varphi \right|^\nu, \qquad (5.16)$$

with $\nu = (\kappa - \alpha)\mu$.

To investigate the scaling exponents this rather formal formulation of Eq. (5.16) can be confronted to the experimental observations and to the macroscopic mean velocity as predicted by simple thermodynamics. As abovementioned the snapshots of Fig. 5.6 are random frames of the process. In Fig. 5.6 g), a straight line segment of at least 4 μm can be seen. Due to the hexagonal scanning pattern with a step size of 0.4 μm, the boundary appears rather ragged. Hence the maximum roughness is half the step size: 0.2 μm. Fig. 5.6 f) has

a maximum roughness of 1 μm. Although the jump time is unknown due to the limited temporal resolution, it is shown that the maximum observed jump perpendicular to the interphase boundary of the whole segment presented in Fig. 5.6, is $1 \pm 0.2 \ \mu m$. It must be realized that this phase transformation may not take place in a plane, but rather in three dimensions.

Within a classical approach the mean velocity for the ferrite-austenite transformation upon increasing the temperature can readily be derived from the net transfer of atoms from ferrite to austenite per unit of time (assuming ferrite and austenite all have the same chemical composition which may not be the case because of carbon segregation in carbides and dissolution of carbides at higher T).

The mean velocity is written as:

$$\bar{v} = \lambda v_0 \ exp \left[-\frac{\Delta g_a + E_\alpha}{kT} \right] - \lambda v_0 \ exp \left[-\frac{\Delta g_a + \Delta g_{\alpha\gamma} \ E_\gamma}{kT} \right], \qquad (5.17)$$

where Δg_a is the activation energy for one atom to leave ferrite, crossing the interface and attach to austenite. The frequency of jumping atoms back and forth across the interface are taken to be identical in ferrite and austenite at the corresponding temperatures. E_γ and E_α refer to strain energies in gamma-austenite and alpha-ferrite, respectively and $\Delta g_{\alpha\gamma}$ is the change in free energy for the growth of austenite by the atoms coming from ferrite. For the moment, the mean velocity derived from simple thermodynamics can be written as:

$$\bar{v} \cong \lambda v_0 \ \frac{\Delta g_{\alpha\gamma}}{kT} exp \left[-\frac{\Delta g_a}{kT} \right] \qquad (5.18)$$

λ is the distance across the interface and v_0 the characteristic frequency (kT/h in Eyring's theory). Taking the values from literature the estimated mean velocity is found 1.5 nm s^{-1} at 840 °C, which is in the right order of magnitude (see Table 5.3) and maybe a bit fortuitous in accordance with the experimental observations.

It is assumed that at the onset of the transformation the concentrations of carbon atoms across the transformation front differ considerably (maximum carbon concentration in atomic percentage in austenite is 0.011 and 0.001 in ferrite at 840 $^\circ$C). However, carbon atoms may have moved over quite a large distance away from the front within the timeframes applied in our experiment. Taking the semi-empirical expression proposed by Ägren [38] as a starting point the diffusion of C in austenite at 840 °C is calculated to be $1.47 * 10^{-7}$ m^{2}s^{-1}. Experimental values of the diffusion coefficient of C in ferrite point at values of $3.57 * 10^{-6}$ m^{2}s^{-1} [39], i.e. leading to considerable velocities away from the interface. These time frames

involved are quite small compared with our experimental conditions, e.g. calculations show that the average carbon content of ferrite has decreased to 0.1 of its initial value in 0.005 s [40,41] at 400 °C. Depending on the local thermodynamic equilibrium conditions of C at the interface versus bulk, affecting the rate determining step (either the fast diffusivity of C in ferrite or the a bit slower diffusivity of C in austenite) in all cases the time scales are fast compared to the experimental conditions. It means that although the onset of the transformation austenite-ferrite is diffusion controlled through carbon diffusion away from the interface, it appears rather as 'interface-controlled' in our experiments. In fact the changes in slope in the Avrami plot (Fig. 5.7) can be related to a discontinuous thickening of the austenite along the grain-boundary indicating that the supply of ledges and steps is rate-limiting. The velocity of the measured discontinuous thickening of austenite can be evaluated by realizing that τ_ξ in Eq. (5.16) can be written as $\bar{\xi}_l^\kappa / \bar{v}_l$, where $\bar{v}_l$ is the mean ledge velocity and $\bar{\xi}_l^\kappa$ is the mean ledge correlation length, i.e.:

$$\bar{v} = \frac{\bar{v}_l \bar{\xi}^\alpha}{\bar{\xi}_l^\kappa} \propto \left| \frac{\Delta g_{\alpha\gamma}}{\Omega} - \frac{\Gamma_{\alpha\gamma}}{h_0} \, \varphi \right|^\nu \tag{5.19}$$

From the experiments (see caption Fig. 5.9) with $\bar{\xi}^\alpha = 0.75\,\mu m$, $\bar{v}_l = 0.02\,\mu m$/s and $\bar{\xi}_l^\kappa = 1.5\,\mu m$ and assuming full linearity in time and length, follows $\bar{v} = 10$ nm/s, which is the right order of magnitude for the mean velocity of the transformation front (see Table 5.3). Nevertheless, deviations from the experimental observations are due to non-linear effects of the correlation length on the actual jump distance and on the time lapse involved. Therefore, from Figs. 5.6 and 5.9 it is concluded that the power law exponents in Eq. (5.19) are not equal to unity being consistent with a jerky type of motion. Clearly the linear dependence between the velocity $\bar{v}$ and $\Delta g_{\alpha\gamma}$, as predicted by the thermodynamical approach Eq. (5.18)), is far too simple and the non-linearity as formulated in Eqs. (5.16) and (5.19) offers a better theoretical framework.

Obviously the rate-limiting factor of discontinuous thickening may become more pronounced and visible in the Avrami plot at lower heating rate and also for fully incoherent rather than for (semi-)coherent boundaries. Higher heating rates provide faster supply of atoms along ledges and kinks, i.e. less discontinuities in thickening and therefore a smoother Avrami plot.

5.7 Conclusions

We have presented a new analysis of moving interphase interfaces between ferrite and austenite at high temperatures using in-situ EBSD. The results are confronted to the well-known classical Johnson-Mehl-Avrami-Kolmogorov (JMAK) equation. It is observed that the interphase boundaries do not move continuously in time but in a jerky-type fashion, In particular, based on *in situ* EBSD observations as a function of temperature, we conclude that the nucleation takes place on grain boundaries and triple junctions and that growth occurs along grain boundaries.

A linear dependence between the average velocity and the driving force related to the change in Gibbs free energy between the phases as predicted by a classical thermodynamical approach turns out to be a far too simple and a non-linear description is offered for a more appropriate theoretical framework.

5.8 References

[1]   M. Avrami, Kinetics of Phase Change. I - General Theory, J. Chem. Phys. 7 (1939) 1103. doi:10.1063/1.1750380.

[2]   J.W. Cahn, Transformation kinetics during continuous cooling, Acta Metall. 4 (1956) 572–575. doi:10.1016/0001-6160(56)90158-4.

[3]   J.W. Cahn, The kinetics of grain boundary nucleated reactions, Acta Metall. 4 (1956) 449–459. doi:10.1016/0001-6160(56)90041-4.

[4]   T. Fukino, S. Tsurekawa, Y. Morizono, In-situ scanning electron microscopy/electron backscattered diffraction observation of microstructural evolution during alpha-gamma phase transformation in deformed Fe-Ni alloy, Metall. Mater. Trans. A Phys. Metall. Mater. Sci. 42 (2011) 587–593. doi:10.1007/s11661-010-0285-4.

[5]   A.F. Gourgues-Lorenzon, Application of electron backscatter diffraction to the study of phase transformations: Present and possible future, J. Microsc. 233 (2009) 460–473. doi:10.1111/j.1365-2818.2009.03130.x.

[6]   A.F. Guorgues-Lorentzon, Application of electron Backscatter diffraction to the study of phase transformations, Int. Mater. Rev. 52 (2007) 65–128.

[7]   I. Lischewski, D.M. Kirch, A. Ziemons, G. Gottstein, Investigation of the alpha-gamma-alpha phase transformation in steel: High-temperature in situ EBSD measurements, Texture, Stress. Microstruct. 2008 (2008). doi:10.1155/2008/294508.

[8]   T. Fukino, S. Tsurekawa, In-Situ SEM/EBSD Observation of α⁄γ Phase Transformation in Fe-Ni Alloy, Mater. Trans. 49 (2008) 2770–2775. doi:10.2320/matertrans.MAW200824.

[9]   M. Gouné, F. Danoix, J. Ågren, Y. Bréchet, C.R. Hutchinson, M. Militzer, G. Purdy, S. Van Der Zwaag, H. Zurob, Overview of the current issues in austenite to ferrite transformation and the role of migrating interfaces therein for low alloyed steels, Mater. Sci. Eng. R Reports. 92 (2015) 1–38. doi:10.1016/j.mser.2015.03.001.

[10]   T. Watanabe, K. Obara, S. Tsurekawa, In-Situ Observations on Interphase Boundary Migration and Grain Growth during α/γ Phase Transformation in Iron Alloys, Mater. Sci. Forum. 467–470 (2004) 819–824. doi:10.4028/www.scientific.net/MSF.467-470.819.

[11]   E.D. Schmidt, E.B. Damm, S. Sridhar, A study of diffusion- and interface-controlled migration of the Austenite/Ferrite front during Austenitization of a case-hardenable alloy steel, Metall. Mater. Trans. A Phys. Metall. Mater. Sci. 38 (2007) 698–715. doi:10.1007/s11661-007-9208-4.

[12]   F. Liu, F. Sommer, E.J. Mittemeijer, An analytical model for isothermal and isochronal transformation kinetics, J. Mater. Sci. 39 (2004) 1621–1634. doi:10.1023/B:JMSC.0000016161.79365.69.

[13]   Y.C. Liu, F. Sommer, E.J. Mittemeijer, The austenite-ferrite transformation of ultralow-carbon Fe-C alloy; transition from diffusion- to interface-controlled growth, Acta Mater. 54 (2006) 3383–3393. doi:10.1016/j.actamat.2006.03.029.

[14]   W. Piekarska, D. Goszczyńska-Króliszewska, Prediction of structure and mechanical properties of welded joints using analytical methods, Procedia Eng. 136 (2016) 82–87. doi:10.1016/j.proeng.2016.01.178.

[15]   P.J. Clemm, J.C. Fisher, The influence of grain boundaries on the nucleation of secondary phases, Acta Metall. 3 (1955) 70–73. doi:10.1016/0001-6160(55)90014-6.

[16]   Z. Yang, R.A. Johnson, An EAM simulation of the alpha - gamma iron interface, Model. Simul. Mater. Sci. Eng. 1 (1993) 707–716. doi:10.1088/0965-0393/1/5/010.

[17]   S. Ratanaphan, D.L. Olmsted, V. V. Bulatov, E.A. Holm, A.D. Rollett, G.S. Rohrer, Grain boundary energies in body-centered cubic metals, Acta Mater. 88 (2015) 346–354. doi:10.1016/j.actamat.2015.01.069.

[18]   G. Bruckner, J. Pospiech, I. Seidl, G. Gottstein, Orientation correlation during diffusional alpha ->gamma phase transformation in a ferritic low carbon steel, Scr. Mater. 44 (2001) 2635–2640. doi:10.1016/s1359-6462(01)00956-3.

[19]   H. Chen, S. van der Zwaag, An Overview of the Cyclic Partial Austenite-Ferrite Transformation Concept and Its Potential, Metall. Mater. Trans. A. 48 (2017) 2720–2729. doi:10.1007/s11661-016-3826-7.

[20]   J. Zhu, R. Ding, J. He, Z. Yang, C. Zhang, H. Chen, A cyclic austenite reversion treatment for stabilizing austenite in the medium manganese steels, Scr. Mater. 136 (2017) 6–10. doi:10.1016/j.scriptamat.2017.03.038.

[21]   H. Chen, S. Van Der Zwaag, Indirect evidence for the existence of the Mn

partitioning spike during the austenite to ferrite transformation, Philos. Mag. Lett. 92 (2012) 86–92. doi:10.1080/09500839.2011.634840.

[22]   H. Chen, S. Van Der Zwaag, An experimental study of the stagnant stage in bainite phase transformations starting from austenite-bainite mixtures, in: TMP 2012 - 4th Int. Conf. Thermomechanical Process. Steels, 2012. https://www.scopus.com/record/display.uri?eid=2-s2.0-84896891374&origin=resultslist&sort=plf-f&src=s&sid=1946a7bc694969cb3dc997da6da11cd7&sot=autdocs&sdt=autdocs&sl=18&s=AU-ID%2857188745139%29&relpos=33&citeCnt=0&searchTerm=.

[23]   H. Chen, B. Appolaire, S. Van Der Zwaag, Application of cyclic partial phase transformations for identifying kinetic transitions during solid-state phase transformations: Experiments and modeling, Acta Mater. 59 (2011) 6751–6760. doi:10.1016/j.actamat.2011.07.033.

[24]   J.T.M. De Hosson, V. Vitek, Chemistry and Physics of Fracture, in: R.M. Latanision, R.H. Jones (Eds.), Dordrecht, Martinus Nijhoft, 1987: p. 363.

[25]   J.T.M. De Hosson, V. Vitek, Atomic structure of (111) twist grain boundaries in f.c.c metals, Philos. Mag. A. 61 (1990) 305–327. doi:10.1080/01418619008234943.

[26]   A.P. Sutton, Irrational interfaces, Prog. Mater. Sci. 36 (1992) 167–202. doi:10.1016/0079-6425(92)90008-U.

[27]   R. Phelan, D. Weaire, the Kelvin problem, in: Taylor & Francis, 1996: p. 125.

[28]   D. Weaire, R. Phelan, Cellular Structures in Three Dimensions, Philos. Trans. R. Soc. A Math. Phys. Eng. Sci. 354 (1996) 1989–1997. doi:10.1098/rsta.1996.0087.

[29]   I. Basu, H. Fidder, V. Ocelík, J. Th.M de Hosson, Local Stress States and Microstructural Damage Response Associated with Deformation Twins in Hexagonal Close Packed Metals, Crystals. 8 (2018) 1–15. doi:10.3390/cryst8010001.

[30]   L.H. Van Vlack, Intergranular Energy of Iron and Some Iron Alloys, J. Met. 3 (1951) 251. doi:https://doi.org/10.1007/BF03397307.

[31]   C. Qiu, H.S. Zurob, D. Panahi, Y.J.M. Brechet, G.R. Purdy, C.R. Hutchinson, Quantifying the solute drag effect on ferrite growth in Fe-C-X alloys using controlled decarburization experiments, Metall. Mater. Trans. A Phys. Metall. Mater. Sci. 44 (2013) 3472–3483. doi:10.1007/s11661-012-1547-0.

[32]   A. Béché, H.S. Zurob, C.R. Hutchinson, Quantifying the Solute Drag Effect of Cr on Ferrite Growth Using Controlled Decarburization Experiments, Metall. Mater. Trans. A. 38A (2007) 2950–2955. doi:10.1007/s11661-007-9353-9.

[33]   E. Schmidt, D. Soltesz, S. Roberts, A. Bednar, S. Sridhar, The Austenite/Ferrite Front Migration Rate during Heating of IF Steel, ISIJ Int.

46 (2006) 1500–1509. doi:10.2355/isijinternational.46.1500.

[34]   T. Watanabe, K. Obara, S. Tsurekawa, G. Gottstein, A mechanism of plane matching boundary-assisted alpha/gamma phase transformation in Fe-Cr alloy based on in-situ observations, Zeitschrift Fur Met. 96 (2005) 1196–1203.

[35]   J.W. Cahn, Theory of crystal growth and interface motion in crystalline materials, Acta Metall. 8 (1960) 554–562. doi:http://dx.doi.org/10.1016/0001-6160(60)90110-3.

[36]   J.W. Christian, The Theory of Transformations in Metals and Alloys, Theory Transform. Met. Alloy. (2002) 832–858. doi:10.1016/B978-008044019-4/50024-6.

[37]   D.S. Fisher, Collective transport in random media: from superconductors to earthquakes, Phys. Rep. 301 (1998) 113–150.

[38]   J. Ågren, A revised expression for the diffusivity of carbon in binary FeC austenite, Scr. Metall. 20 (1986) 1507–1510. doi:10.1016/0036-9748(86)90384-4.

[39]   J.R.G. da Silva, R.B. McLellan, Diffusion of carbon and nitrogen in B.C.C. iron, Mater. Sci. Eng. 26 (1976) 83–87. doi:10.1016/0025-5416(76)90229-9.

[40]   M. Hillert, L. Höglund, J. Ågren, Escape of carbon from ferrite plates in austenite, Acta Metall. Mater. 41 (1993) 1951–1957. doi:10.1016/0956-7151(93)90365-Y.

[41]   S.A. Mujahid, H.K.D.H. Bhadeshia, Partitioning of carbon from supersaturated ferrite plates, Acta Metall. Mater. 40 (1992) 389–396. doi:10.1016/0956-7151(92)90313-4.

Chapter 6

Steel surface passivity and local corrosion behaviour

This Chapter sheds light on the time scales involved with passivation of steel surfaces. Corrosion resistance of these surfaces is assessed by a very local determination of the oxide layer chemical composition.

6.1 Introduction

Most metals, but more specific stainless steel, exhibit a passive layer which protects the bulk from further corrosion. The bare metal surface has a tendency to form a thin oxide film on the metal-gas interface. The passive film on stainless steel is a crucial barrier to retard or block further corrosion of the bulk. Although the kinetics of the growth of thin oxides can be described by the theory of Cabrera and Mott [1], scant knowledge is present of the characteristic time scale of the passivation process of stainless steel in ambient conditions, i.e. on air. When the passive layer is damaged, e.g. during processing steps in an industrial environment, the passive film has to recover. It is crucial to keep the material in an optimal environment during this recovery process, in order to ensure that the repassivated layer is of sufficient quality for further use. In general the structure and composition of this layer depends on the conditions present at formation, e.g. dry-, wet-, chloride containing environment or acid solutions, for which the thickness can vary from 1 to 4 nm [2]. An overview of the growth of ultrathin passive films is provided in [3]. Techniques as Scanning Kelvin Probe Force Microscopy (SKPFM) [4–11], and Scanning Tunneling Microscopy (STM) [12,13] are used for asessing the corrosion behaviour of these films.

Once a stable passive layer is formed, the layer can be forced to adapt to a changing environment such as a high temperature and can grow to thicknesses of several 100s of micrometers, as seen on steel exposed to steam at 600 °C [14–16], 700 °C [17]. and 1000 °C [18]. Apart from the conventional techniques, recently also ToF-SIMS has been used to characterize the oxide layer on steel, for example to characterize the oxide layer on 316L [19]; micrometer thick oxide layer on 310 SS [20]; coated steel [21] and the oxide layer on 304L after exposure of steam [22]. These studies focussed on the general composition of the oxide layer. ToF-SIMS has been used for more localized phenomena as pitting on CrNi steel [23], or on steel under bacteria attack [24].

Characterisation of thin layers on a polycrystalline material remains a challenge. Recent study on polycrystalline iron by Takabatake [25,26], established clear results with grains in the order of several 100s of micrometers. In this Chapter we try to push this length scale forwards to polycrystalline steel with grains of only 10 μm in diameter.

6.2 Recovery

In this Section a quantitative method is presented to follow the growth of the passive layer after damage, in-situ by AFM. The characteristic time of the recovery of the passive layer is also investigated stepwise with XPS and continuous using a Kelvin Probe.

6.2.1 In-situ AFM

The studied material is a martensitic stainless steel of class AISI 420. Samples were given a mirror polish finish, where the final step included polishing with ¼ micron diamond particles. An even smoother result could have been obtained by finishing with e.g. colloidal silica particle suspension as OP-S or OP-U which are of a typical size of 40 nm. However, these suspensions are water based, as opposed to the alcohol-type lubrication used for polishing with diamond particles. Recovery of the passive layer immediately after polishing would thus partly take place under very wet conditions, not resembling recovery in regular atmospheric conditions, which could affect the typical composition and thickness of the passive layer. After polishing with ¼ micron diamond particles, the surface was rinsed with ethanol and dried with warm air. Thereafter samples were placed

for 7 days in a controlled environment with 50% relative humidity and a temperature of 21 °C, in order to restore a stable passive layer.

The passive layer can be removed by sputtering the oxides with argon ions. Therefore, a sample was placed on an XPS sample-holder, as shown in Fig. 6.1. The upper part of the sample was shielded by a tantalum foil. The foil allows for close placement at the surface (without touching), to exclude shadowing and side effects during sputtering/bombardment with Argon ions. The sputtering gun has an incident angle with the surface of 50 degrees, releasing Ar^+ ions with energy of 2 keV. No large differences in oxide removal is expected, as the sputter rate of Fe_2O_3 and Cr_2O_3 are 0.62 and 0.54 respectively, relative to sputtering of SiO_2 [27]. The argon beam is rasterizing over the whole sample holder area, which provides an equal exposure to Ar^+ ions. Sputtering took place in an UHV preparation chamber, which was coupled to an XPS chamber. During the ion bombardment the pressure in the chamber increased from 10^{-9} to 10^{-7} mbar, caused by the leakage of argon ions. Nevertheless, the partial pressure of oxygen was too low for short term re-passivation of the bare substrate.
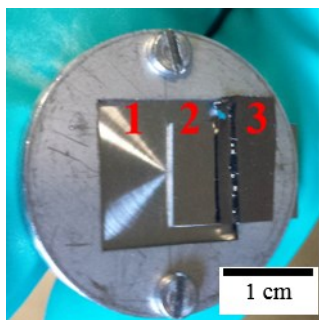

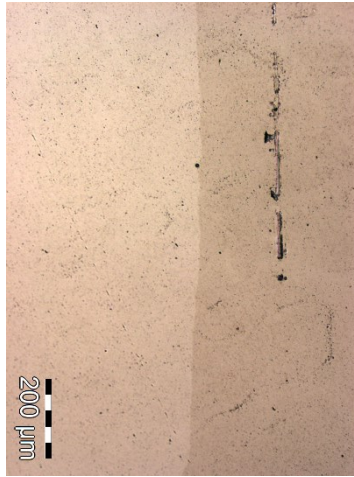*Figure 6.1. XPS sample holder (1), with sample (2) and tantalum foil shield (3).*

Figure 6.2. Optical image of the surface after sputtering. Light area (left) exposed to sputtering, dark area (right) shielded during sputtering.

Sputtering was periodically interrupted to perform an XPS scan to probe the surface composition. In this way it is verified that the passive film is removed, and unnecessary sputtering of the metal substrate is prevented. For the specimen considered in this work and three test samples, this point was reached after 15 minutes sputtering. The border between the sputtered and not-sputtered area is clearly visible by eye and under the optical microscope, as illustrated in Fig. 6.2.

Atomic force microscopy (AFM) was conducted using a Veeco Dimension 3100 with sub-nanometer resolution. The contrast between the two regions of Fig. 6.2 aids in finding the appropriate scanning position with the optical microscope of the AFM. An area of 25 x 25 μm^2 was sampled in normal tapping mode, with 512 x 512 line resolution per image. Care was taken to place the sample such that the AFM scanning trace was perpendicular to the border, i.e. from left to right as in Fig. 6.2. The resulting trace can be seen in Fig. 6.3. Although the trace has not been leveled with a plane fit, it is clearly seen that, from left to right, the surface contains a step on the left from the center.
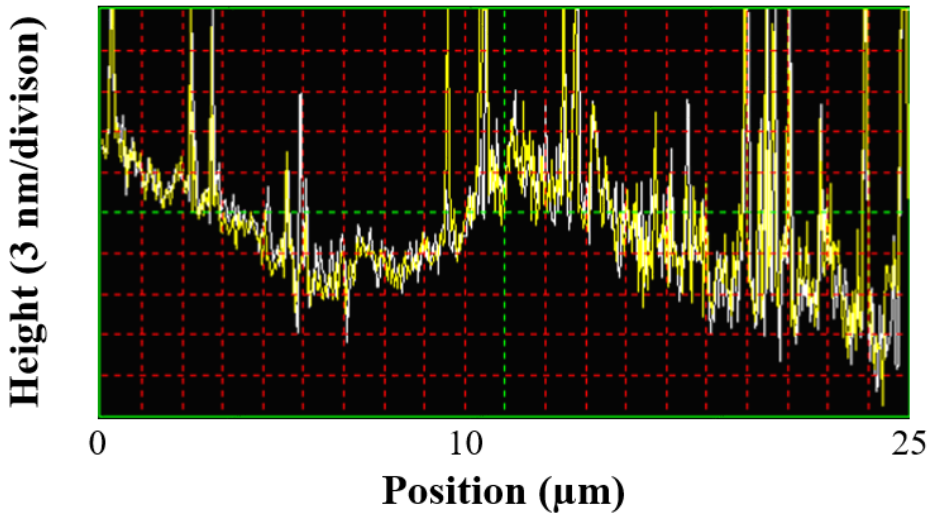
Figure 6.3. Typical trace with the step visible left of the center.

A complete 25 x 25 micrometer scan is shown in Fig. 6.4, with a plane fit for visualization purpose only. Visible over the whole substrate are scratches smaller than 25 nanometers, which are remnants from polishing. It is clear that the right-hand side has an elevation with respect to the left-hand side.

To quantify the step between these two areas, we define a data processing method with computer code (Mathematica software) which uses the raw AFM x, y and z data as input. The z values represent the height of the x and y plane, with y defined as parallel to the border. For each x position, the z values of all corresponding y points (i.e. a column) are averaged. In this way the traces as in Fig. 6.3, are averaged for each of the 512 y-entries, in order to make a 2D projection of the topography. This projection is shown in Fig. 6.5. The points in blue are used for a fit of the sputtered area, red for the not-sputtered. A third order polynomial function is fitted through the points of the step (in black). The x-value, where the first order derivative of this function changes sign, is defined as the position of the step. The absolute difference between the two planes fitting at this position is therefore taken as the height of the step.
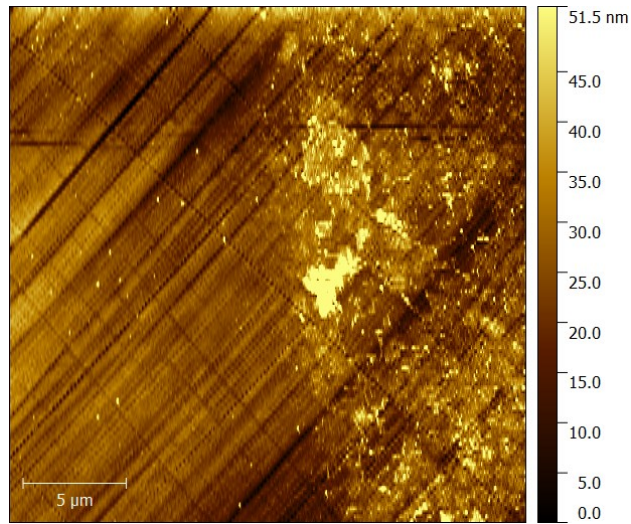
Figure 6.4. AFM topography map with sputtered section on the left side, and the elevated not-sputtered area on the right.
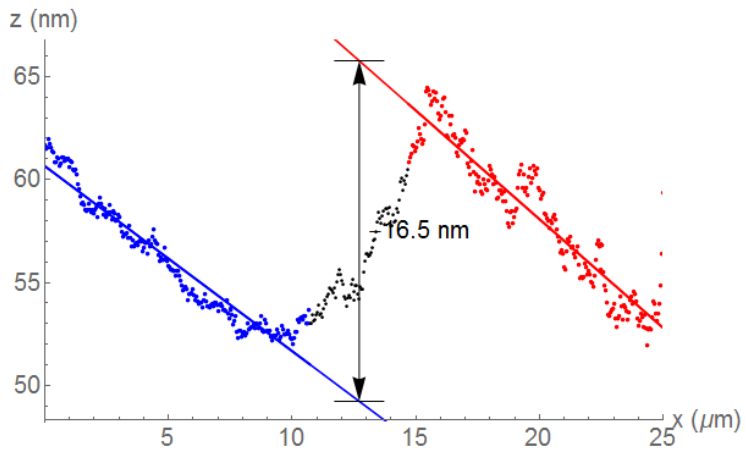

Figure 6.5. 2D projection of the topography, where blue represent a fit of the sputtered plane, red a fit of the not-sputtered plane.

The optical difference in color at the step is also noticeable after several weeks of re-passivation. Therefore the change in color (from dark to light, Fig. 6.4) is not only caused by the difference in passive layer thickness, but most likely also due to a difference in roughness.

In the following experiment the change of the step height after sputtering, due to recovery of the passive layer, will be presented. The sample was sputtered

until the passive layer was removed. Thereafter the specimen was removed from the vacuum chamber and placed in the AFM, under ambient conditions of about 50% RH and 21 °C. There the sputtering boundary had to be found and the AFM tip brought close to the surface. The first scan could be started 25 minutes after exposure, and took 20 minutes to complete. Immediately after finishing, a new scan was started on the same area. Following scans were made with an interval of one hour, as shown in Fig. 6.6. The step height decreases with time and stabilizes after 2 hours to a difference of -9 nanometers, confirmed by a measurement after 5 days.
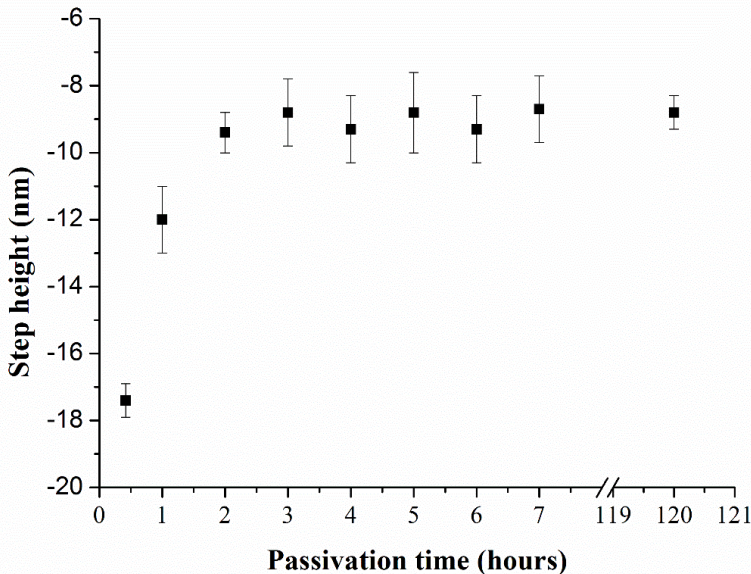

Figure 6.6. AFM recording of the decrease of the step height, during recovery of the sputtered passive layer.

Immediately after exposure to air, i.e. after removal from the vacuum chamber, the sputtered (bare) surface starts to oxidize. If we assume that in the early stage of passivation (< 1 hour) the growth of the layer is approximately linear, extrapolation of the first two points towards zero will provide an onset step (t=0) of -21 nm. The passive layer consists of Fe_3O_4, Fe_2O_3, and Cr_2O_3, with density of 5180, 5240 and 5210 kg/m^3, respectively [28], in contrast to 7874 kg/m^3 for pure iron. Therefore a density ratio of $\rho_{ox} / \rho_{met} = 0.67$ exists for Fe_2O_3 (ox) and Fe (met). The relation between the two becomes:

$$\frac{m_{ox}}{V_{ox}} = 0.67\, \frac{m_{met}}{V_{met}} \qquad\qquad (6.1)$$

If we assume, for example, that the passive layer consists solely of Fe_2O_3, the ratio of the molecular masses is

$$\frac{m_{ox}}{V_{ox}} = \frac{Fe_2O_3}{2*Fe} = \frac{159.7}{111.7} = 1.43 \qquad\qquad (6.2)$$

Inserting the relation of Eq. (6.2) into Eq. (6.1), results in:

$$\frac{V_{ox}}{V_{ox}} = 2.13 \qquad\qquad (6.3)$$

Repetition of this calculation for the other oxides gives a volumetric ratio of 2.10 for Fe_3O_4, and 2.02 for Cr_2O_3, respectively.

After removal of the passive layer, the bare metal surface is at the same height as the oxide-metal interphase of the remaining layer. Re-passivation implies that the metal surface has to be transformed to oxide. The remaining step of -9 nm after passivation represents therefore the equivalent metal layer of the removed passive layer. Considering Eq. (6.3), the volume of the oxidized metal is about 2.1 times the volume the metal ions would posses in the lattice of the corresponding metal. Hence the thickness of the passive layer can be estimated at about 2.1 * (-9) nm = -18.9 nm. This is close to the extrapolated initial step height of 21 nm. It must be realized that the metal-oxide interphase of the re-passivated area is now also 9 nm lower than the interphase of the not-sputtered area.

The density ratios calculated with Eq. (6.1) are for crystalline materials. However, parts of the passive layer can be amorphous. The density of a fully amorphous oxide is about 10% lower of the crystalline value. The volumetric factor of Eq. (6.3) will change to 2.39, resulting in an estimation of -21.5 nanometer of the passive film.

6.2.2 Static XPS

The characteristic time the passive layer needs for forming, has also been studied on a thermal hardened specimen. The initial ferritic material was heated to 1050 °C with a dwell time of 20 minutes, followed by rapid cooling in air which resulted in a fully martensitic structure. The surface was then polished as described before. As seen in Section 6.2.1, the passive layer starts to re-establish immediate after the polishing due to exposure to air (oxygen). From here the sample was taken into a controlled chamber where the relative humidity was kept at 50%. After the

desired exposure time, the sample was taken to a vacuum chamber. The time needed for transport until the opened vacuum chamber was pumped again, was 5 minutes. The chamber was pumped eventually to a pressure below 10^{-10} mbar, which is an ultra high vacuum. At this point the sample is considered not to proceed with re-establishing its (not full grown) passive layer, due to the scarcity of oxygen. The already existing passive layer is than sputtered with Ar-ions, and examined with XPS. The depth profiles of oxygen, iron and chromium were extracted. Chromium is from the top down, first mainly detected in the oxidized state, as it is part of the passive layer. Deeper in the passive layer a metallic chromium peak is arising, originating from the chromium in the bulk. The depth at which the amount of metallic chromium is 50% of the total signal can be considered as the end of the passive layer [29].

The above described procedure has been repeated for samples which were exposed to air for different times after polishing. The end of the passivation layer (indicated by the Ar-ion sputtering time) is shown as a function of exposure time in Fig. 6.7. The first data point is the minimum amount of 5 minutes after polishing. It can be seen that the measured thickness below 100 minutes of passivation is fluctuating. The points at 180 and 360 minutes are significantly higher.

The short exposed samples (<100 min.) might have suffered from small variations right after polishing during ethanol rinsing and drying with warm air, which influenced the initial speed of the repassivation. If the average of these points is taken, a thickness reached by 5.4 minutes of Ar-sputtering represents the initial step of repassivation. Considering the following points at 180 minutes (11 minutes sputtering) and at 360 minutes (14 minutes sputtering), the fastest growth of the passive layer is than between 5 and 180 mintues of exposure (an increase of 5.6), followed by a decrease of this speed between 180 and 380 minutes of exposure (an increase of 3). The data points however are too scattered for sound conclusions.
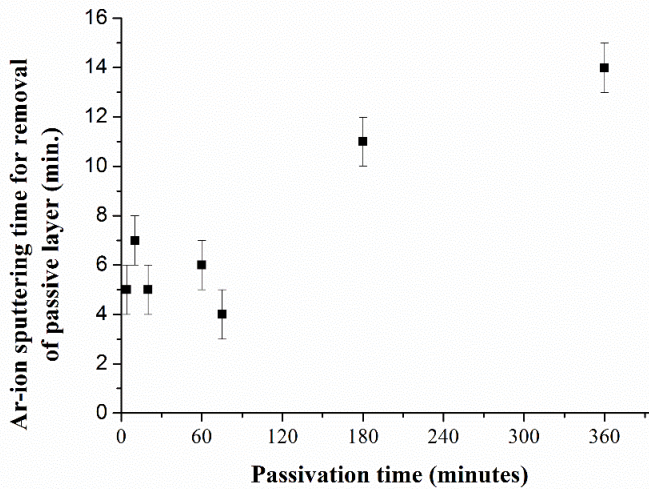
Figure 6.7. Oxide layer thickness (expressed as the time needed to remove the oxide layer with Ar-sputtering) as a function of exposure time to air after polishing, measured by XPS.

6.2.3 In-situ Kelvin Probe

A more continuous measurement of similar samples was done with a Kelvin Probe (KP) at TU Delft, Dept. of Materials Science and Engineering. With this approach the surface work function is derived. This work function, φ, is the result of dipoles in the top layer. The magnitude and direction of the dipoles depends on the chemical composition and surface microstructure. Details on the working principle of the KP can be found in [4,30]. With a vibrating tip of 0.5 mm in diameter, the voltage contact potential difference (V_{CPD}) between the tip and the surface is measured. The surface work funtion φ_{sample} is derived from the relation [30]:

$$V_{CPD} = \frac{\varphi_{tip} - \varphi_{sample}}{-e} \tag{6.4}$$

The tip work function φ_{tip} is determined by measuring a reference gold surface. The noble gold is assumed to be resistant to oxidation for which a constant surface work function of 5.1 eV is used. In general for an oxidized metal surface, the work function will increase.

The experiment was conducted with a KP in a humidity controlled environment. Details on this setup can be found in [31]. The sample surface received a final polishing with 1 μm diamond particles in an alcohol based lubricant

for 5 minutes, to remove the passive layer. After rinsing with ethanol and careful drying the sample was placed on the Kelvin Probe stage in the humidity chamber within 5 minutes from the moment the polishing was stopped. The Kelvin Probe V_{CPD} measurement was started while the chamber was still recovering from being opened. The intial fluctuations in the relative humidity set point of 50%, was ±3%. The measured V_{CPD} is very sensitive with respect to these fluctuations, as water on the surface causes the addition of more dipoles. The RH fluctuations were monitored on a reference sample, and caused a response of the V_{CPD} in the range of 100 mV. 5 minutes after opening of the humidity chamber, the RH was stable within 1%. From this point on the V_{CPD} was recorded continuously. Data points of a time span of 5 minutes were averaged in order to compensate for any small fluctuations. The work function of the recovering surface has been measured from 5 minutes after the passive layer was removed, and continued to a total of 17 hours, as shown in Fig. 6.8. The work function is increasing the most in the first two hours, while it stabilizes towards a value of 4.2 eV between 3 and 5 hours. The increase to higher work function values is in agreement with the mechanism of oxidation. The starting value of 3.5 eV seems to be off compared to literature work functions: 4.5 eV for Cr, 4.67 eV for Fe surfaces ({100} crystal planes) and 4.81 eV ({111} crystal planes) [32]. More recent work including calculations and measurements for Fe gives values of 4.12 – 4.93 eV, dependent on crystal orientation [33,34]. The reason for the discrepancy between the absolute value and the literature values is not known. However in the search of the characteristic recovery time we can observe a stabilization of the surface around 3 hours, which is in the same order of the previous results obtained from AFM (~2 hours) and XPS (between 3 and 6 hours).
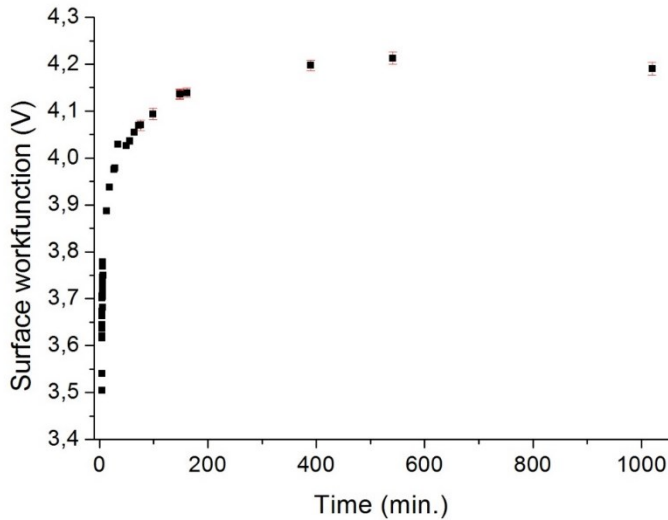
Figure 6.8. Surface workfunction as measured with a Kelvin Probe as a function of exposure time to air with 50% RH after polishing.

6.3 Local oxide layer alteration in relation to microstructure

As mentioned above, a study on polycrystalline iron showed a clear distinction of the oxide thickness with respect to the crystal orientation [25]. Although electrochemical tests on pure pure iron are not conclusive, the general image that arises is that {100} planes are more susceptible for oxidation [25,26,35–37].

In Chapter 4 we derived a relation between the bulk grain orientation and the amount of surface oxidation. Summarizing the main conclusions:

- At the start of oxidation the surface oxidation is decomposed in {001} lacking behind of {111} & {101} planes: {001} < {111} & {101}.
- The second stage of oxidation is split into a threefold system with {001} planes still lacking behind, but {101} progress faster than {111}: {001} < {111} < {101}.

We continue to investigate this grain orientation dependent oxidation on the microscale, through local chemical analysis with ToF-SIMS.

6.3.1 Oxidation at 300 °C in air – yellow surface

The first set of chemical analysis per grain has been done on a thermal treated surface. The polished sample was kept at 300 °C for 20 minutes in air, which induced a smooth gold-yellow surface. Prior to oxidation micro-indents had been made as reference markers. The surface was indexed with EBSD and suitable grains were selected with the distint crystal orientations close to {111}, {110} and {001} planes parallel to the sample surface. The average grain diameter is between 10 - 15 μm. An area of 50x50 μm^2 containing the selected grains was profiled with ToF-SIMS. A Focused Ion Beam (FIB) gun was operated in a raster over the selected area. The primary ion beam for sputtering consists of Gallium ions having energy of 10 keV and a total current of 200 pA. In this configuration, a spot size and thus a lateral resolution of about 40 nm in diameter was attained. The spots were binned in an image (frame) of 1024x1024 pixels. From the stack of frames, a 3D sampling is obtained. From this data, one can select an area on the surface and extract the counts of the selected ion throughout the frames. In this way a depth profile can be extracted. The marker indents and the appearing microstructure after grain orientation mapping assisted in locating the area of interest. The grain orientation map with the defined areas is shown in Fig. 6.9
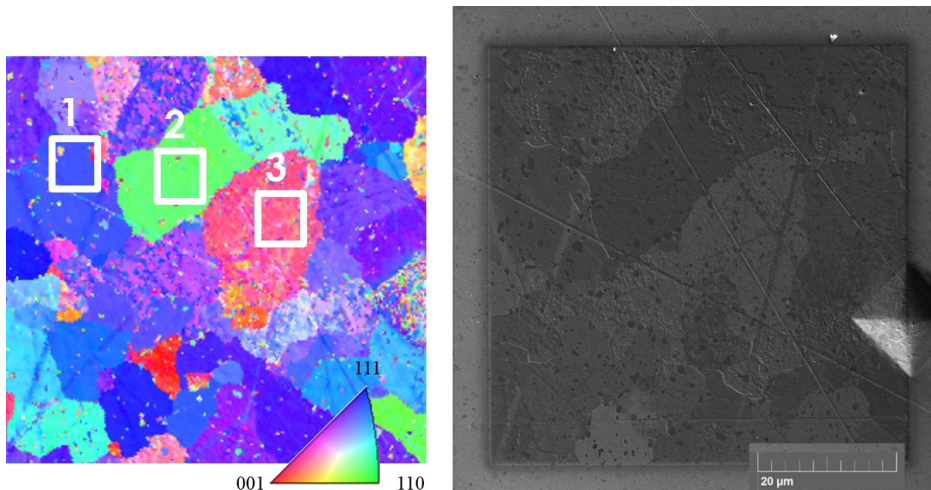

Figure 6.9. Left: investigated grains of the specimen after a thermal treatment at 300 °C. Areas 1, 2 and 3 are located within grains with {111}, {110} and {001} directions, respectively. Right: SEM image of the same area after ToF-SIMS mapping.

The oxygen depth profiles of these three grains are plotted in Fig. 6.10. Frame zero is the frame obtained from the surface. A higher frame number indicates a measurement from deeper in the surface. From the graph it is seen that the amount of detected oxygen shows a spike at the surface. This can be due to the presence of e.g. organic contaminants at the surface. The spike and the drop of the first recorded frames are considered as artefacts. After about 70 frames the amount of counts starts to reduce significantly, which can be correlated to the start of the end of the oxide layer. The oxide signal is almost zero at 110 frames, marking the end of the oxide layer. However, there is a difference between the lines originating from the oxides on the different bulk grain orientations. Both {100} and {110} reach their oxide minimum earlier compared to {111}. The oxygen profile of the {100} and {110} direction are almost equal. From these oxide depth profiles can therefore be deduced that the oxidation for this thermal treated specimen progresses in the order {111} > {110} & {001}.
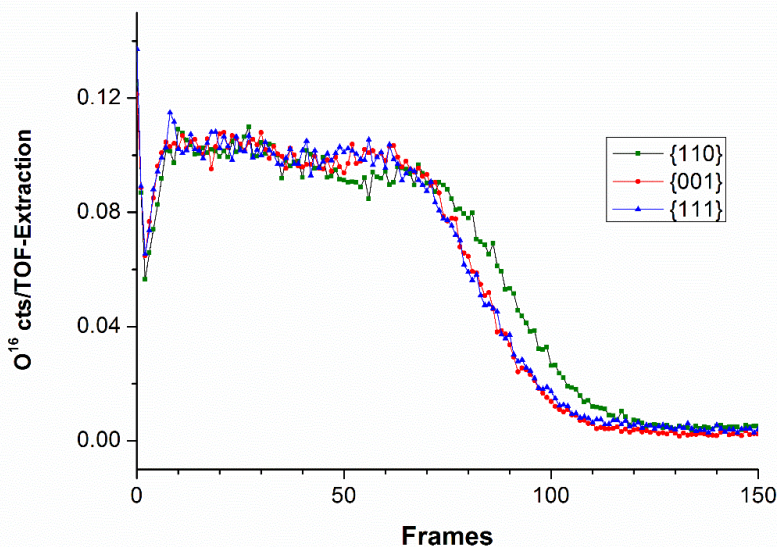

Figure 6.10. Depth profile for O- for grains of each of the three main crystal orientations after a thermal treatment at 300 °C in air.

Two areas of 50x50 μm^2 were mapped with ToF-SIMS operating in positive mode and negative mode for the two respective areas. The cross-sections of this sampling are shown for the ions O^-, Cr^+, CrO_2^-, Fe^+ and FeO_2^-.as depicted in Fig. 6.11. The surface contains an oxygen rich layer, which is divided into two

sublayers with an enrichment of FeO_2^- at the top, and CrO_2^- at the bottom. The secondary ions FeO_2^- and CrO_2^- are characteristic for the oxide species present in the film. In earlier work with XPS and GIXRD on this type of steel, the presence of this dual layer has also be shown to be an iron oxide Fe_2O_3 rich surface layer, with an inner Fe_3O_4 layer, which also has a chromium enrichment (see Chapter 4). Thin vertical lines can be seen on the Cr^+ cross section. These lines originate from the chromium carbides. The contribution of the carbides to the overall Cr^+ count is relatively small.
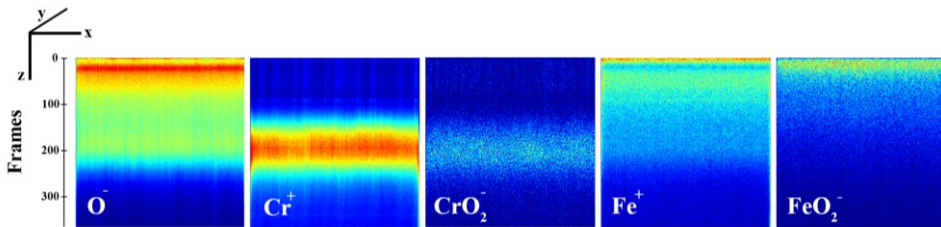

Figure 6.11. Cross section of stacked frames obtained by ToF-SIMS, for the ions O^-, Cr^+, CrO_2^-, Fe^+ and FeO_2^-. The x-axis (frontal) and the y-axis (perpendicular to the plane, integrated signal) are both 50 μm; the z-axis (top to bottom) is constructed by the frames, with frame 0 at the top as the initial outer surface. The colour code represents the count intensity, with red highest intensity and blue as the lowest with zero counts. The maximum (red) is different for each image.

6.3.2 Oxidation at 450 °C in air – purple surface

A specimen with a thicker oxide was acquired by applying a thermal treatment of 450 °C for 20 minutes in air, resulting in a characteristic purple/blue-ish surface. An optical image of a typical area is shown in Fig. 6.12, together with the [001] IPF map of the bulk grains at the surface.
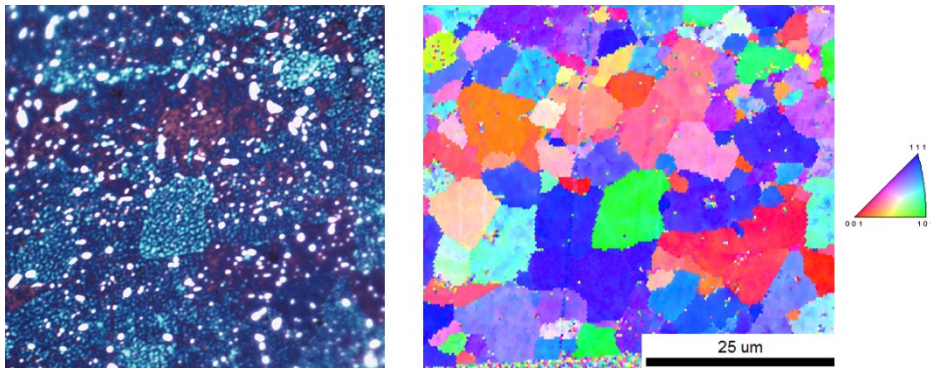
Figure 6.12. Left: optical image of the purple oxidized surface. Right: [001] IPF map of the same area as in the optical image.

The shape of the grain in the center with {101} crystal planes parallel to the surface with colour code green (Fig. 6.12 right), is also clearly seen in the optical image as a bright light blue area. The red colour coded grains with orientation towards the {001} direction are recognized in the optical image as dark red – purple areas. In particular seen above the center ({101} oriented-) grain, as well as on the bottom right-side. The colours observed with the optical microscope can be placed in an oxidation thickness colour palette, as also illustrated in Fig. 4.1. The bright blue indicates a thicker oxide layer than the dark red areas [38].

Two grains of each of the 3 principal orientations {111}, {110} and {001} were selected, from which the depth profile of oxygen was extracted. The lines of these 6 grains are shown in Fig. 6.13. For this specimen we observe that the end of the oxide layer is reached after about 300 frames. Also here a difference between the profiles originating from the oxides on the different bulk grain orientations is seen. The oxygen count for the grains with {001} direction goes first towards zero. Then for the {111} oriented grain, followed by {011} as very last. This indicates that the oxide thickness is not equal on each grain, in fact for this specimen it depends on the grain orientation in the order of {011} > {111} >{001}.

The amount of frames between the onset of the end of the oxide layer (at 200 frames) and the end (around 300 frames), provides information about the width of the oxide-bulk interface. For the {011} orientated grains the width is 150 frames, while the interface for the {001} grains is about 60 frames. The oxide-bulk mixed region for the grains with the{001} orientation is therefore less than half the thickness compared to the {011} orientated grains.
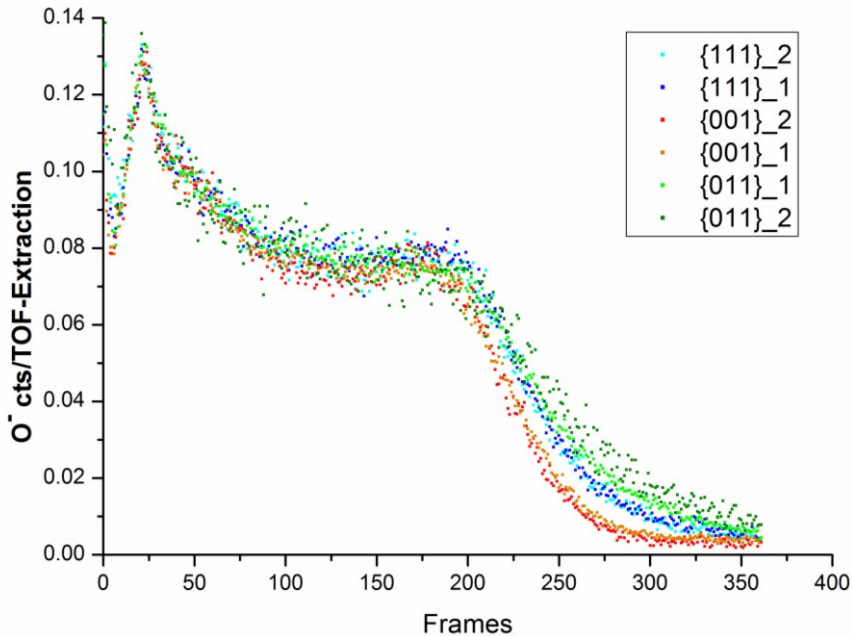
134

Figure 6.13. Depth profile for O⁻ of two grains (six in total) of each of the three main crystal orientations after a thermal treatment at 450 °C in air.

A similar area of 50x50 μm^2 was mapped in the so-called positive mode. Also here three main grain orientations were selected, from which both the Fe$^+$ and Cr$^+$ depth profiles were extracted. The counts of both ions from each frame have been divided in order to obtain the measured Cr$^+$/Fe$^+$ ratio throughout the oxide layer for each crystal orientation. These Cr$^+$/Fe$^+$ ratio profiles are shown in Fig. 6.14. The outer layer of the surface consists of mainly iron oxide, resulting in a ratio of almost zero for 125 frames. Thereafter the enrichment of chromium is reached, giving a notable increase in the ratio. This increase however is different for the three distinct grain crystal orientations. Clearly the {001} orientation has the highest ratio peaking at Cr$^+$/Fe$^+$ = 3.5, followed by {111} (Cr$^+$/Fe$^+$ = 2) and {110} (Cr$^+$/Fe$^+$ = 1.5) as last.
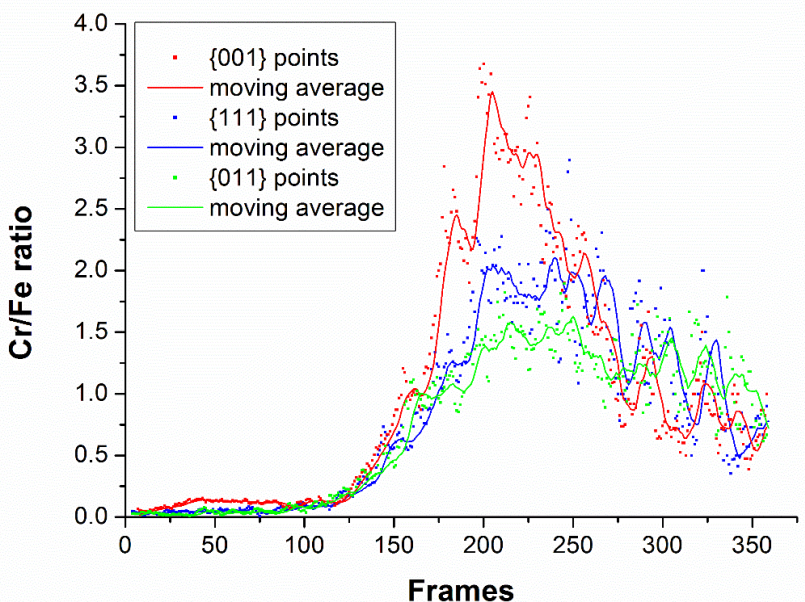
Figure 6.14. Cr^+/Fe^+ ratio throughout the oxide layer for the three main crystal orientations after a thermal treatment at 450 °C in air. The data points are obtained by applying a moving average of 6 frames for the counts of Cr^+ and Fe^+ respectively before calculation of the ratio. The solid lines are an average of this ratio constructed from points in the graph, applying a moving average of 10 for the three series.

The Cr/Fe ratio is an important parameter for the corrosion resistance of the passive or oxide layer, where a higher Cr content indicates a better corrosion resistance. It has to be noted that the calculated ratio here does not represent the absolute ratio. The relative sensitivity of each element is inversely proportional to the sputtering yield. For more details see e.g. [39]. The yield for Cr^+ is lower than for Fe^+. Initial there might be a preferential sputtering of Fe^+. However, as there is a chemical mixture in the matrix, the ratio will balance due to an equal sputter removal of the remaining (slightly abundant) Cr^+ ions and (preferential) Fe^+ removal.

The ratio for the FeO_2^- and CrO_2^- ions, characteristic for the oxide species, has been determined in a similar way as for the Cr^+/Fe^+ ratio. However, the profiles have been extracted from an area mapped in negative mode and are shown in

Fig. 6.15 The same distinction is noticed as for the Cr^+/Fe^+ ratio: the {001} orientation has the highest ratio, followed by {111} and {110}.
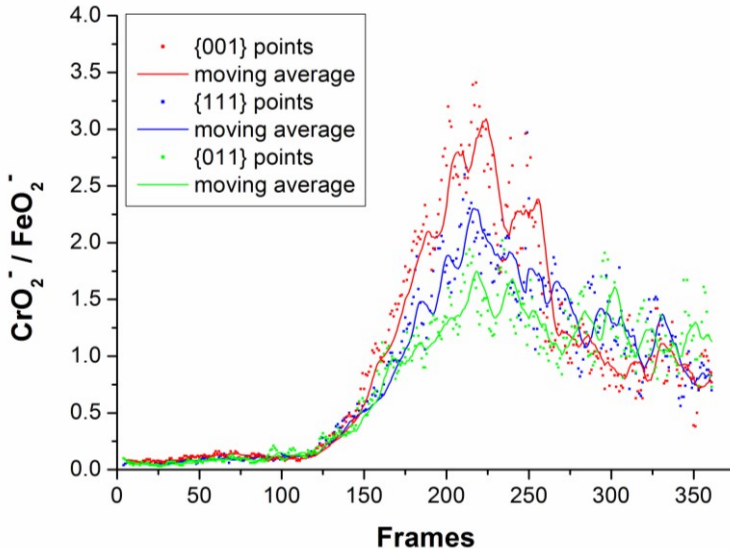

Figure 6.15. CrO_2^- / FeO_2^- ratio throughout the oxide layer for the three main crystal orientations after a thermal treatment at 450 °C in air. The data points are obtained by applying a moving average of 6 frames for the counts of CrO_2^- and FeO_2^- respectively before calculation of the ratio. The solid lines are an average of this ratio constructed from points in the graph, applying a moving average of 5 for the three series.

6.3.3 Non-oxidized reference surface

The previous results are compared with a non-oxidized reference specimen. This surface was two times mirror polished; including a final step with ¼ micron particles with an alcohol based lubricant to avoid etching and advanced corrosion due to exces water exposure. After polishing the sample was kept at room temperature in an environment with air of 50% RH for 48 hours to restore the passive layer. After the first polishing sequence indents were made to serve as reference point for an EBSD grain-orientation mapping. EBSD mapping requires exposure of the surface to the electron beam for several hours, in which processes as hydro-carbon deposition are active. The very last polishing and recovery steps were repeated to annul any effects which could influence the passive layer. The

various grains were not clearly distinguishable in the optical and electron microscope, compared to the colour oxidized speciments. After ToF-SIMS mapping, the grain boundaries and also contrast differences between the grains could be seen. This visual information combined with the known distance from the reference markers, made it possible to select areas in grains with the orientations of interest. The oxygen depth profile of this reference for three grain orientations is shown in Fig. 6.16. However, both {100} and {110} orientations reach the oxygen minimum earlier compared to {111} orientation. From this we might conclude that the oxide layer is slightly thicker on the {111} oriented grains.
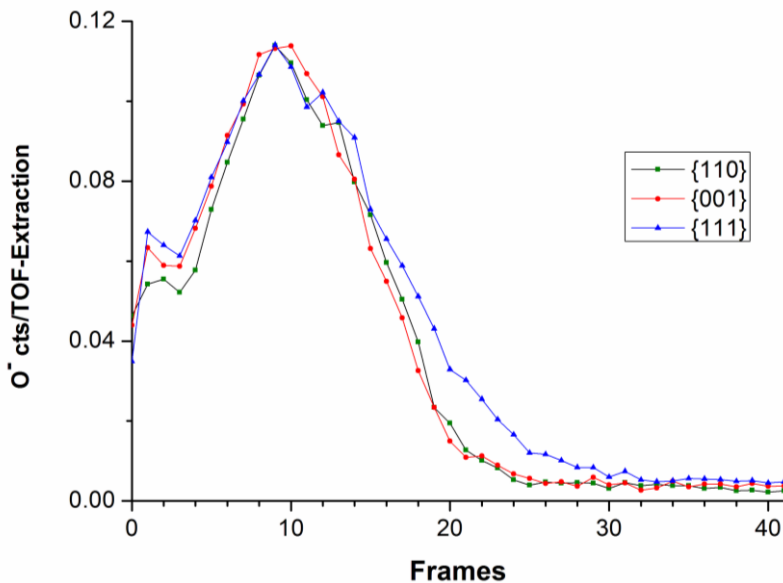

Figure 6.16. Depth profile for O^- for the three main crystal orientations of an untreated passive layer.

The point where the oxygen signal is close to zero, is reached after about 300 (purple surface), 100 (yellow surface) and 20 (not oxidized surface) frames. When a conservative value of 5 nm for the thickness of passive layer of the not-oxidized specimen is taken, a thickness estimation can be made of 25 nm and 75 nm for the yellow (300 °C) and purple (450 °C) surface respectively.

Considering the specimen with a thermal treatment at 450 ℃ in air, the {001} orientated grains reached the end of the oxide layer after 260 frames, versus 350 frames for the {011} orientated grains. With a difference of 90 frames and an

estimated thickness of 75 nm for 300 frames, a rough calculation shows that the end of the oxide layer is reached about 22 nm deeper for the {011} orientated grains compared to the {001} orientated grains.

Based on the oxide depth profile of the three grain, it is confirmed that the oxidation progresses in two stages with different final oxide layer thicknesses:

-   Stage one, which includes the passive layer and an induced thermal oxide layer formed up to 300 °C: {111} > {011} & {001}
-   Stage two with thermal oxidation to 450 °C: {011} > {111} > {001}.

6.4 Oxygen, does it gamble?

So far, characterization of the tempered surface is done by means of the detectable oxides through XPS, XRD or ToF-SIMS. The generated depth profiles sometimes give the impression of a uniform thick oxide layer. However the microstructure can have an influence on the local composition of the passive layer, as has been concluded in Chapter 4 and Section 6.3. On top of the grains and grain boundaries, also chromium carbides are part of the microstructure. The carbide oxidation behavior during thermal treatment is therefore investigated. A polished specimen was heated to 300 °C in air for 20 minutes. The resulting yellow/gold appearing surface was then scanned with AFM. The topography map is seen in Fig. 6.17. The carbides with their typical size of ~ 0.5-1 μm are recognized by their slightly elongated shape. Their dark color code in the topography maps indicate that they are located deeper in the surface. Fig. 6.18 shows a height profile over one of the carbides. It clearly shows that the carbide surface is flat, which is the result of the surface polish prior to oxidation. The rest of the matrix however is covered with round spherical tips which are emerging from the matrix creating a cauliflower-like surface. At the top they possess a diameter of about 100 nm. It has to be noted that the height differences between the tips are about 15 nm at max (as demonstrated at the side of the carbide in Fig. 6.17), where their lateral diameter is an order of magnitude higher. At this sub-micron scale, the surface is therefore best visualized as an undulating landscape. On Fig. 6.17-left, traces of the spheres can be seen forming sub-structures. These structures are more pronounced in the SEM image of the surface in Fig. 6.19. These structures form domains in the order of 500 nm, much smaller than the average bulk grain size of 10-15 μm. Therefore they can not be related to microstructural features as grain boundaries.
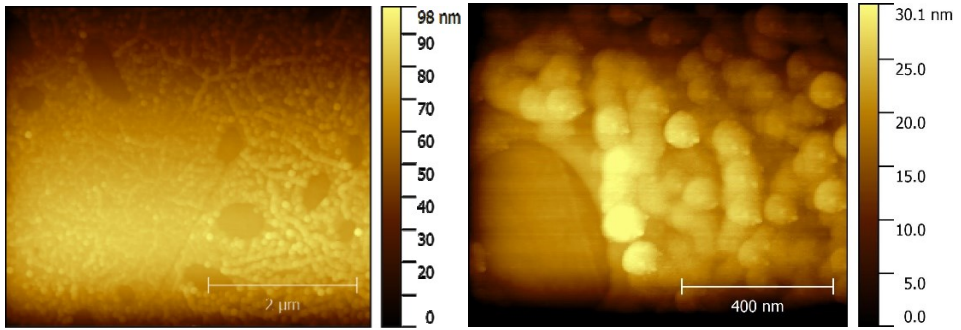
Figure 6.17. AFM topography map of a polished steel surface after a thermal treatment at 300 °C in air. The lower areas (dark colour code) are chromium carbides.
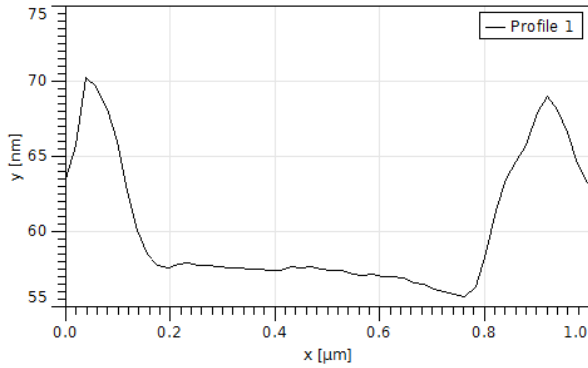

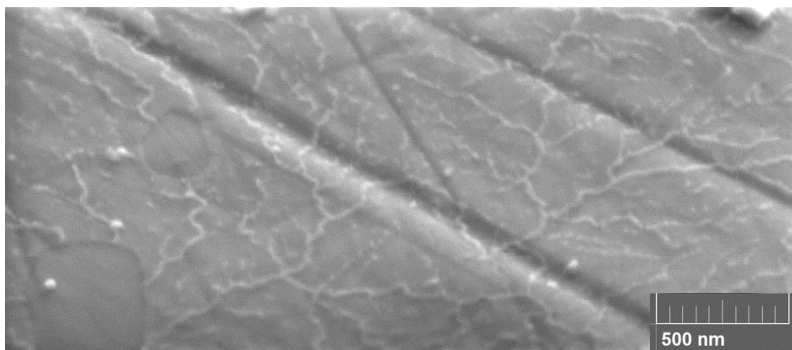*Figure 6.18. AFM height profile over a carbide.*

Figure 6.19. SEM image of a polished steel surface after a thermal treatment at 300 °C in air.

In Section 6.3 it was concluded that a secondary stage in the oxidation of the surface is reached when the specimen is heated to 450 °C in air for 20 minutes. A SEM close-up of this purple surface is shown in Fig. 6.20. Also here spheres are found at the surface, however with their size of about 400 nm in diameter they are 4 times larger than the spheres of the specimen heated to 300 °C in air. The area was mapped with ToF-SIMS. The superimposed 3D map for iron (Fig. 6.20) shows a low intensity of Fe at the chromium carbides. The oxide spheres however match with high Fe intensities. Also the map of oxygen shows, high oxygen concentrations on the spheres and low values for the carbides. On the other hand the stacked frames for Cr show high Cr concentrations at the carbides, but low values for the oxide spheres. This chemical analysis makes clear that the carbides conist of mainly Cr with a small (thin) chromium oxide layer. The chromium oxide on steel is known as a very stable oxide where a thin layer of a few nm already gives sufficient protection against further thermal corrosion. The mainly Fe-rich matrix is vulnerable to further oxidation. Although Cr enrichment is present at the oxide/bulk interface, the top part of the matrix oxide layer consists of mainly iron oxides, which tend to emerge in nodular structures. These structures lack in Cr, for the bigger spheres the absence of chromium is even further into the oxide.
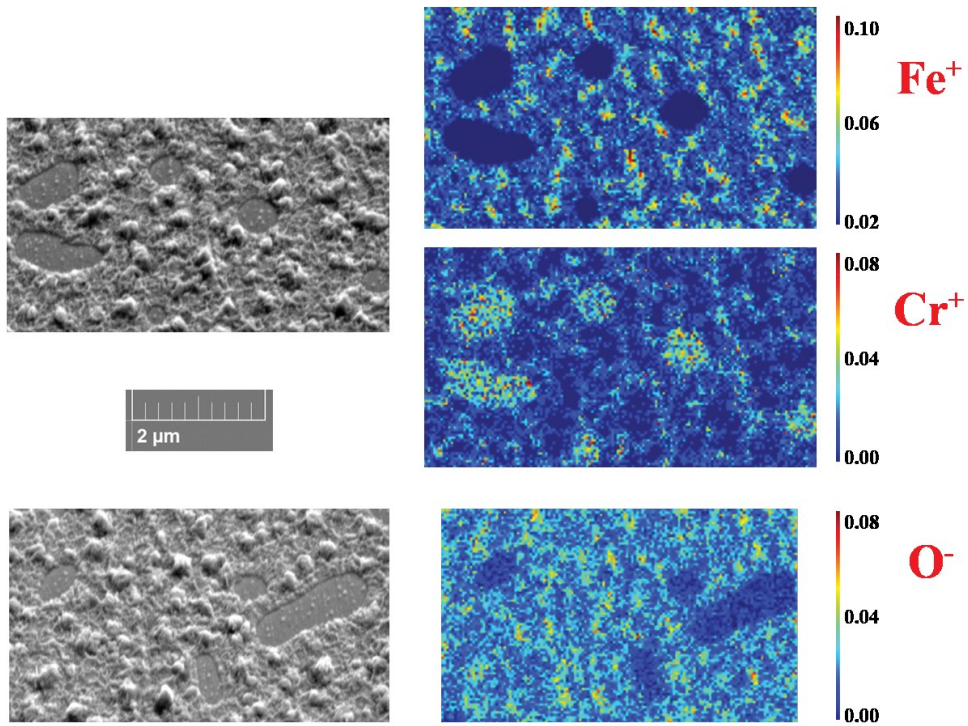
*Figure 6.20. **Left column:** SEM images of a polished steel surface after a thermal treatment at 450 °C in air. Clearly visible are the flat carbides laid deeper in the surface, and nodules decorating the surface. **Right column:** corresponding ToF-SIMS mappings of the SEM areas displaying the top 12 stacked frames of the surface for: Fe^+ (top); Cr^+ (middle); O^- (bottom).*

Instead of tempering in air, a heat treatment can also be applied in a low oxygen pressure environment. In the following experiments a Kammrath & Weiss heating module (see Fig. 2.7) was used inside an electron microscope, operating under a Partial Oxygen pressure $(PO_2) < 10^{-4}$ mbar. The polished specimen was heated at 550 ºC for 90 minutes. After this treatment the surface was mapped with AFM. The topography maps of an area including multiple grains, and a part of a grain boundary are shown in Fig. 6.21. The elevated features correspond to the microstructure: the grain boundaries and the carbides are oxidized and expand from the surface. A height profile over a grain boundary shows that this local microstructure swells 30 nm out of the surface. Here can be seen that the matrix but more profound the grain boundaries, are decorated with small spheres, presumably

oxides. With an XPS scan on the surface mainly oxidized chromium is detected. The Ellingham diagram [40] indicates that chromium oxide is more stable compared to the iron oxides. The papers of Hultquist and Leygraf [41,42] on an earlier stage of forming an oxide layer on FeCr alloy in slightly elevated temperature and low oxygen pressure conditions, report a competition between the oxygen supply at the surface and the supply of Fe or Cr at the surface, depending on their respective diffusion speeds through the bulk. In the early stage as shown in Fig. 6.21, it is clear that the oxidation takes place at mainly chromium rich places as carbides and grain boundaries. In fact, this oxidation behavior is completely in another way than oxidation in air where mainly the matrix was covered with iron oxides.
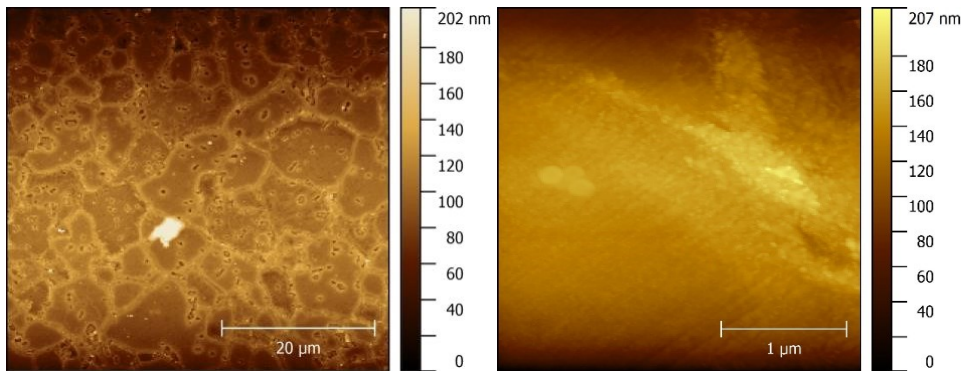

Figure 6.21. AFM topography map of a polished steel surface after heating to 550 °C in vacuum with $PO_2 < 10^{-4}$ mbar for 90 minutes. The higher areas (brighter colour code) are related to chromium carbides and grain boundaries.

Although the sample shows a uniform oxidation structure in the middle, at the edges of the sample a gradient of oxidation could be distinguished. The sample was partly clamped and possible at the edges also exposed to slightly more oxygen due to degassing of the heating stage. Three oxidation stages are displayed in Fig. 6.22 and show various degrees in the amount of chromium oxides, which exhibit a bright blue colour. In an early stage mainly the carbides oxidize. Later grain boundaries are fully covered with these oxides. From the boundaries the oxide grows lateral untill almost the whole grain is coverd. The oxide gradient of a sample heated to 920 ºC is shown in Fig. 6.23. Here we see that the surface is fully covered and as the oxide thickness increases, also the perceived colour is changing due to the thin film interference, as discussed in Chapter 4.
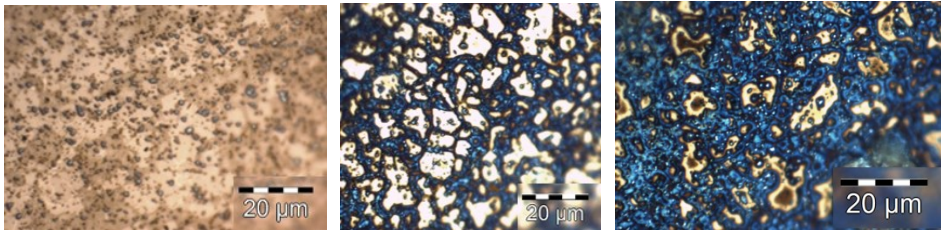
Figure 6.22. Optial images showing three stages of oxidation in a low oxygen pressure environment.
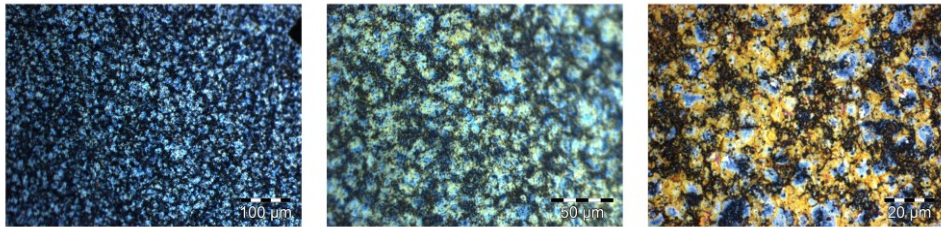

Figure 6.23. Optial images showing surfaces fully covered with chromium oxide, changing colour from blue to yellow as the film thickens.

6.5 Conclusions

Recovery of the passive layer after removal by argon ions has been followed in-situ with AFM. The nescesarry time needed for growth of the passive layer on this ferritic steel is about 2 hours. In situ measurement on a hardened specimen with a Kelvin Probe, indicated that the oxide layer is stabilized after 3 to 4 hours.

Chemical analysis with ToF-SIMS on the microscale of FeCr steel revealed that the oxide thickness is dependent on the orientation of the bulk grain at the surface. Two oxidation stages could be distinguished. The different oxidation processes change gradually whereby the first stage is mainly present up to 350 °C; the second stage is most pronounced at 450 °C.

- Stage I is present at the (not oxidized) reference sample, and for heating up to 300 °C in air. Here the surface oxide is thicker for grains with the {111} crystal planes parallel to the surface. The oxidation layer thickness order is: {111} > {110} & {001}.
- Stage II after heating for heating to 450 °C in air. The oxide thickness is not equal on each grain. In fact the order changed as the {011} grains are clearly more oxidized, followed by {111} grains. Least oxidized

are the grains with {001} orientation. Therefore the oxidation layer thickness order is: {011} > {111} > {001}.

The determined Cr^+/Fe^+ ratio is significant higher for the {001} grains.

Tempering in air leads to grain orientation dependent oxidation, where the mainly the matrix is covered with iron oxide nodules. The nodules are depleted in Cr, making them potential weak spots for corrosion attacks.

Tempering with low partial oxygen pressure induces selective oxidation on grain boundaries and carbides, forming predominantly chromium oxides.

6.6 References

[1] N. Cabrera, N.F. Mott, Theory of the oxidation of metals, Reports Prog. Phys. 12 (1949) 163–184. doi:10.1088/0034-4885/12/1/308.

[2] S. Jin, A. Atrens, Passive films on stainless steels in aqueous media, Appl. Phys. A. 50 (1990) 287–300. doi:10.1007/BF00324495.

[3] V. Maurice, P. Marcus, Passive films at the nanoscale, Electrochim. Acta. 84 (2012) 129–138. doi:10.1016/j.electacta.2012.03.158.

[4] M. Rohwerder, F. Turcu, High-resolution Kelvin probe microscopy in corrosion science: Scanning Kelvin probe force microscopy (SKPFM) versus classical scanning Kelvin probe (SKP), Electrochim. Acta. 53 (2007) 290–299. doi:10.1016/j.electacta.2007.03.016.

[5] Ö. Özkanat, B. Salgin, M. Rohwerder, J.M.C. Mol, J.H.W. de Wit, H. Terryn, Scanning Kelvin Probe Study of (Oxyhydr)oxide Surface of Aluminum Alloy, J. Phys. Chem. C. 116 (2012) 1805–1811. doi:10.1021/jp205585u.

[6] M. Nonnenmacher, M.P. O'Boyle, H.K. Wickramasinghe, Kelvin probe force microscopy, Appl. Phys. Lett. 58 (1991) 2921–2923. doi:10.1063/1.105227.

[7] H.N. McMurray, G. Williams, Probe diameter and probe-specimen distance dependence in the lateral resolution of a scanning Kelvin probe, J. Appl. Phys. 91 (2002) 1673–1679. doi:10.1063/1.1430546.

[8] V. Guillaumin, P. Schmutz, G.S. Frankel, Characterization of Corrosion Interfaces by the Scanning Kelvin Probe Force Microscopy Technique, J. Electrochem. Soc. 148 (2001) B163. doi:10.1149/1.1359199.

[9] B. Maachi, C. Pirri, A. Mehdaoui, N.E. Hakiki, J.L. Bubendorff, Atomic Force Microscopy, Scanning Kelvin Probe Force Microscopy and magnetic measurements on thermally oxidized AISI 304 and AISI 316 stainless steels, Corros. Sci. 53 (2011) 984–991. doi:10.1016/j.corsci.2010.11.031.

[10] C. Örnek, D.L. Engelberg, SKPFM measured Volta potential correlated

with strain localisation in microstructure to understand corrosion susceptibility of cold-rolled grade 2205 duplex stainless steel, Corros. Sci. 99 (2015) 164–171. doi:10.1016/j.corsci.2015.06.035.

[11]　L.Q. Guo, X.M. Zhao, B.C. Wang, Y. Bai, B.Z. Xu, L.J. Qiao, The initial stage of atmospheric corrosion on interstitial free steel investigated by in situ SPM, Corros. Sci. 70 (2013) 188–193. doi:10.1016/j.corsci.2013.01.028.

[12]　J. Kunze, V. Maurice, L.H. Klein, H.H. Strehblow, P. Marcus, In situ STM study of the duplex passive films formed on Cu(111) and Cu(001) in 0.1 M NaOH, Corros. Sci. 46 (2004) 245–264. doi:10.1016/S0010-938X(03)00140-9.

[13]　H. Chen, M. Bettayeb, V. Maurice, L.H. Klein, L. Lapeire, K. Verbeken, H. Terryn, P. Marcus, Local passivation of metals at grain boundaries: In situ scanning tunneling microscopy study on copper, Corros. Sci. 111 (2016) 659–666. doi:10.1016/j.corsci.2016.04.013.

[14]　B. Pujilaksono, T. Jonsson, H. Heidari, M. Halvarsson, J.-E. Svensson, L.-G. Johansson, Oxidation of Binary FeCr Alloys (Fe–2.25Cr, Fe–10Cr, Fe–18Cr and Fe–25Cr) in O2 and in O2 + H2O Environment at 600 °C, Oxid. Met. 75 (2011) 183–207. doi:10.1007/s11085-010-9229-z.

[15]　T. Jonsson, B. Pujilaksono, H. Heidari, F. Liu, J.-E. Svensson, M. Halvarsson, L.-G. Johansson, Oxidation of Fe–10Cr in O2 and in O2+H2O environment at 600°C: A microstructural investigation, Corros. Sci. 75 (2013) 326–336. doi:10.1016/j.corsci.2013.06.016.

[16]　T. Jonsson, S. Karlsson, H. Hooshyar, M. Sattari, J. Liske, J.-E. Svensson, L.-G. Johansson, Oxidation After Breakdown of the Chromium-Rich Scale on Stainless Steels at High Temperature: Internal Oxidation, Oxid. Met. 85 (2016) 509–536. doi:10.1007/s11085-016-9610-7.

[17]　J. Yuan, W. Wang, H. Zhang, L. Zhu, S. Zhu, F. Wang, Investigation into the failure mechanism of chromia scale thermally grown on an austenitic stainless steel in pure steam, Corros. Sci. 109 (2016) 36–42. doi:10.1016/j.corsci.2016.03.021.

[18]　I. Saeki, T. Saito, R. Furuichi, H. Konno, T. Nakamura, K. Mabuchi, M. Itoh, Growth process of protective oxides formed on type 304 and 430 stainless steels at 1273 K, Corros. Sci. 40 (1998) 1295–1305.

[19]　S. Tardio, M.-L. Abel, R.H. Carr, J.E. Castle, J.F. Watts, Comparative study of the native oxide on 316L stainless steel by XPS and ToF-SIMS, J. Vac. Sci. Technol. A Vacuum, Surfaces, Film. 33 (2015) 05E122. doi:10.1116/1.4927319.

[20]　A. Grinberg Dana, M. Starostin, G.E. Shter, A. Buk, O. Dinner, G.S. Grader, Metal Corrosion Screening in a Nitrogen-Based Fuel at High Temperature and Pressure, Oxid. Met. 82 (2014) 491–508. doi:10.1007/s11085-014-9504-5.

[21]　B. Díaz, E. Härkönen, J. Świątowska, A. Seyeux, V. Maurice, M. Ritala,

P. Marcus, Corrosion properties of steel protected by nanometre-thick oxide coatings, Corros. Sci. 82 (2014) 208–217. doi:10.1016/j.corsci.2014.01.024.

[22] A.S. Mamede, N. Nuns, A.L. Cristol, L. Cantrel, S. Souvi, S. Cristol, J.F. Paul, Multitechnique characterisation of 304L surface states oxidised at high temperature in steam and air atmospheres, Appl. Surf. Sci. 369 (2016) 510–519. doi:10.1016/j.apsusc.2016.01.185.

[23] A. Rossi, B. Elsener, G. Hähner, M. Textor, N.D. Spencer, XPS, AES and ToF-SIMS investigation of surface films and the role of inclusions on pitting corrosion in austenitic stainless steels, Surf. Interface Anal. 29 (2000) 460–467. doi:10.1002/1096-9918(200007)29:7<460::AID-SIA889>3.0.CO;2-T.

[24] A. Seyeux, S. Zanna, A. Allion, P. Marcus, The fate of the protective oxide film on stainless steel upon early stage growth of a biofilm, Corros. Sci. 91 (2015) 352–356. doi:10.1016/j.corsci.2014.10.051.

[25] Y. Takabatake, Y. Kitagawa, T. Nakanishi, Y. Hasegawa, K. Fushimi, Heterogeneity of a Thermal Oxide Film Formed on Polycrystalline Iron Observed by Two-Dimensional Ellipsometry, J. Electrochem. Soc. 163 (2016) C815–C822. doi:10.1149/2.0211614jes.

[26] Y. Takabatake, Y. Kitagawa, T. Nakanishi, Y. Hasegawa, K. Fushimi, Grain Dependency of a Passive Film Formed on Polycrystalline Iron in pH 8.4 Borate Solution, J. Electrochem. Soc. 164 (2017) C349–C355. doi:10.1149/2.1011707jes.

[27] D.R. Baer, M.H. Engelhard, A.S. Lea, P. Nachimuthu, T.C. Droubay, J. Kim, B. Lee, C. Mathews, R.L. Opila, L. V. Saraf, W.F. Stickle, R.M. Wallace, B.S. Wright, Comparison of the sputter rates of oxide films relative to the sputter rate of SiO2, J. Vac. Sci. Technol. A Vacuum, Surfaces, Film. 28 (2010) 1060. doi:10.1116/1.3456123.

[28] H. Viefhaus, K. Hennesen, M. Lucas, E.M. Müller-Lorenz, H.J. Grabke, Ion Sputter Rates and Yields for Iron-, Chromium- and Aluminium Oxide Layers, Surf. Interface Anal. 21 (1994) 665–672. doi:10.1002/sia.740210911.

[29] M. Vayer, I. Reynaud, R. Erre, XPS characterisations of passive films formed on martensitic stainless steel: qualitative and quantitative investigations, J. Mater. Sci. 35 (2000) 2581–2587. doi:10.1023/A:1004719213960.

[30] W. Melitz, J. Shen, A.C. Kummel, S. Lee, Kelvin probe force microscopy and its application, Surf. Sci. Rep. 66 (2011) 1–27. doi:10.1016/j.surfrep.2010.10.001.

[31] A. de Rooij, Polarization Measurements Under Atmospheric Conditions Using A Kelvin Probe As A Reference Electrode, 17th Int. Corros. Congr. (2008). http://esmat.esa.int/Publications/Published_papers/DeRooij17ICCLas_Veg

as.pdf.

[32]   CRC Handbook of Chemistry and Physics, (2015) 12–124.

[33]   P. Błoński, A. Kiejna, Calculation of surface properties of bcc iron, Vacuum. 74 (2004) 179–183. doi:10.1016/j.vacuum.2003.12.118.

[34]   P. Błoński, A. Kiejna, Structural, electronic, and magnetic properties of bcc iron surfaces, Surf. Sci. 601 (2007) 123–133. doi:10.1016/j.susc.2006.09.013.

[35]   K. Fushimi, A. Kazuhisa, M. Seo, Evaluation of Heterogeneity in Thickness of Passive lron by Scanning Flectrochemical Microscopy Films on Pure, ISIJ Int. 39 (1999) 346–351.

[36]   A. Schreiber, C. Rosenkranz, M.M. Lohrengel, Grain-dependent anodic dissolution of iron, Electrochim. Acta. 52 (2007) 7738–7745. doi:10.1016/j.electacta.2006.12.062.

[37]   K. Fushimi, Y. Takabatake, T. Nakanishi, Y. Hasegawa, Microelectrode techniques for corrosion research of iron, Electrochim. Acta. 113 (2013) 741–747. doi:10.1016/j.electacta.2013.03.021.

[38]   U.R. Evans, The Colours Due to Thin Films on Metals, Proc. R. Soc. A Math. Phys. Eng. Sci. 107 (1925) 228–237.

[39]   L.A. Giannuzzi, F.A. Stevie, Introduction to focused ion beams: Instrumentation, theory, techniques and practice, 2005. doi:10.1007/b101190.

[40]   H.J.T. Ellingham, Reductibility of oxides and sulphides in metallurgical processes, J. Soc. Chem. Ind. 63 (1944) 125–160. doi:10.1002/jctb.5000630201.

[41]   G. Hultquist, C. Leygraf, The initiation of selective oxidation of a ferritic stainless steel at low temperatures and oxygen pressures, Corros. Sci. 22 (1982) 331–346. doi:10.1016/0010-938X(82)90034-8.

[42]   G. Hultquist, M. Seo, N. Sato, Selective oxidation of FeCr alloys in the 295-450 K temperature range, Oxid. Met. 25 (1986) 363–372. doi:10.1007/BF01072915.

Summary

This work concentrates on the properties and functionality of materials used in product manufacturing. Special attention is paid to the relation between the material microstructure and its performance. An in-depth understanding of the microstructural and surface modifications during processing is acquired, in order to reveal their contributions to the final shape change and the surface properties of fabricated products.

The chain of processing steps for product manufacturing starts with forming. Here a piece of stainless steel of grade AISI 420 is shaped into the desired form by the process of deep drawing. This cold forming introduces large residual stresses. A breakthrough finding in our work is that when the product experiences a thermal treatment, these stresses relax due to a creep process and cause a shape change of the product. The mechanical behavior during forming and heat treatment is scrutinized by experiments and implemented in a Finite Element routine. In this way a powerful tool is developed which allows for a detailed study of the contribution of individual process parameters to the key shape parameters. Investigations of critical parameters indicate that metal forming (flattening) and a temperature gradient have a significant impact on the final cup shape change, and can either positively or negatively influence the quality of the product.

The thermal treatment also involves a phase transformation. The dynamics of interphase boundary motion during transformations is studied through in-situ high temperature electron-back scatter diffraction (EBSD). A novel method was designed to derive the velocity of the interphase boundaries from the EBSD phase maps. An important observation is that the interphase boundaries do not move continuously in time but in a jerky-type fashion. A new theoretical framework is presented to explain these observations.

The heat treatment also alters the surface chemical composition. The evolution of the oxide layer during a thermal treatment was investigated. The oxide thickness and composition of surfaces tempered at a range of temperatures under various environments, were characterized with the use of XPS. It was found that the substrate crystal orientation has a predominant influence on the composition and thickness of the oxide layer. Subsequently, electron microscopy was combined with a variety of other surface sensitive techniques to characterize the structure and

composition of the oxide film in further detail. In particular we have observed a novel sequence in oxidation rate of crystal planes parallel to the surface for Fe-Cr steel: {001} < {111} & {101}.

Finally, in practice the passive layer on steel is subjected during service to modifications after exposures to high temperatures or mechanical damage. A damaged passive layer is vulnerable for corrosion during its recovery. The surface should be kept at optimal conditions while recovering is taking place. The crucial question that needs to be addressed is: What is the required time for recovery? The answer is found after investigations with Kelvin Probe and AFM on damaged, but recovering parts of the surface. It is concluded that the recovering of the surface for this particular steel, stabilizes after 3 hours. This is a very relevant outcome for product manufacturing.

Samenvatting

Dit proefschrift richt zich op de eigenschappen en functionaliteit van materialen die worden gebruikt voor de fabricage van metalen componenten. De relatie tussen de microstructuur en de prestaties van dit materiaal staat hierbij centraal. In het promotietraject is diepgaande kennis van de aanpassingen van de microstructuur en oppervlakte verkregen, met als doel het aan het licht brengen van de effecten op de vormverandering en oppervlakte eigenschappen van de componenten.

Het fabricageproces van de metalen componenten begint doorgaans met het vormgeven van de componenten. Een stuk roestvast staal uit de klasse AISI 420 wordt in de gewenste vorm gebracht door middel van dieptrekken. Deze koudvormbewerking zorgt voor een aanzienlijke opbouw van restspanningen. Tijdens de noodzakelijke warmtebehandeling veranderen de componenten bovendien op kritische punten van vorm. Een belangrijke vondst in dit onderzoek is dat deze restspanningen afnemen door een thermisch geactiveerd kruipproces. Het mechanische gedrag tijdens het vormgeven en de warmtebehandeling is gedetailleerd in kaart gebracht door middel van experimenten. Hiermee is een materiaalmodel opgesteld, dat vervolgens geïmplementeerd is in een Eindige Elementen-rekenmethode. Met deze implementatie is een nieuwe en robuuste methode ontwikkeld waarmee de invloed van de afzonderlijke processtappen op de vormverandering kan worden berekend. Verder rekenkundig onderzoek van de processtappen met deze methode heeft uitgewezen dat zowel het vormgeven (dieptrekken), als een ongelijk temperatuurprofiel een significante invloed heeft op de uiteindelijke vorm van de componenten. Deze effecten kunnen zowel op een positieve als negatieve wijze invloed hebben op de kwaliteit van de componenten.

Tijdens de warmtebehandeling treedt er ook een fasetransformatie op. De dynamiek van de voortbewegende grens tussen twee fases is onderzocht met electron-back scatter diffraction (EBSD) bij hoge temperatuur. In dit werk is een nieuwe methode ontwikkeld om de snelheid van de fasegrens uit EBSD-fasemappen af te leiden. Een belangrijke observatie is dat de fasegrens niet continu voortbeweegt in de tijd, maar op een schokkerige wijze. Een nieuw theoretisch kader is gepresenteerd om deze observatie te beschrijven.

Door de warmtebehandeling verandert ook de chemische samenstelling van het oppervlak. De evolutie van de oxidelaag gedurende de warmtebehandeling is onderzocht met XPS. De oppervlaktes zijn blootgesteld aan diverse temperaturen en omstandigheden, waardoor de samenstelling en dikte van de oxides variëren. Een belangrijke ontdekking is dat de kristalorientatie van de korrels aan de oppervlakte een directe en dominante invloed hebben op de samenstelling en dikte van de oxidelaag. Een bijzondere vinding hierbij is de nieuwe volgorde in de oxidatie snelheid van polykristallijn Fe-Cr staal: de oxidatiesnelheid is afhankelijk van de kristalvlakken parrallel aan de oppervlakte in de volgorde {001} < {111} & {101}.

Afsluitend, in de praktijk is de passieve laag op staal onderhevig aan veranderingen door blootstelling aan hoge temperatuur of mechanische belasting. Zolang een beschadigde passieve laag herstellende is, is deze kwetsbaarder en gevoeliger voor corrosie. Daarom zou het oppervlak tijdens herstel in optimale omstandigheden moeten verkeren. Een cruciale vraag hierbij is: Wat is de benodigde tijd voor herstel? Deze vraag kon worden beantwoord na onderzoek met een Kelving Probe en AFM van beschadigde, maar herstellende delen van het oppervlak. Geconcludeerd kan worden dat het herstel van dit specifieke staal stabiliseert na drie uren. Deze uitkomsten van het onderzoek kunnen bij juiste implementatie bijdragen aan de optimalisatie van de commerciële fabricage van metalen componenten.

List of publications

Journal papers

G. Zijlstra, M. Groen, et al., "On the role of the residual stress state in product manufacturing", *Materials & Design,* 105 (2016) 375–380.

G. Zijlstra, M.S.B. van Daalen, D.I. Vainchtein, V. Ocelík, J.T.M. De Hosson, "Interphase boundary motion elucidated through in-situ high temperature electron back-scatter diffraction", *Materials & Design,* 132 (2017) 138–147.

G. Zijlstra, L.T.H. de Jeer, V. Ocelík, J.T.M. De Hosson, "The effect of surface texture on the oxidation behaviour of polycrystalline Fe-Cr", *Applied Surface. Science,* 459 (2018) 459–467.

M. Groen, G. Zijlstra, et al., "Product shape change by internal stresses", *Materials & Design,* 157 (2018) 492–500.

H. Farahani, G. Zijlstra, M. G. Mecozzi, V. Ocelík, J. Th. M. De Hosson, S. van der Zwaag, "In-situ high-temperature EBSD and 3D Phase Field studies of the austenite-ferrite transformation in a medium Mn steel", *(submitted for publication).*

G. Zijlstra, S. Gersen, Y.Y. Mostafa, V.M. Goossens, D.I. Vainchteina, P. Visser, H.B. Levinsky, J.Th.M. De Hosson, "On the morphology of Silicon Oxide deposition arising from the combustion of siloxane-containing biogas", *(submitted for publication).*

G. Zijlstra, T. Šamořil, H. Tesařová, V. Ocelík, J.Th.M. De Hosson, "Depth profile analysis of thin oxide layers on polycrystalline FeCr", *(in preparation)*

Conference proceedings

G. Zijlstra, E.T. Faber, V. Ocelík, J.T.M. De Hosson, "The growth of a passive film on steel studied with in-situ AFM", *Materials and contact characterisation VIII, WIT Transactions on Engineering Sciences*; vol. 116 (2017) 23-29

Curriculum Vitae

Gerrit Zijlstra

06 July 1989   Born in het Bildt, the Netherlands

Education

2014 - 2018   PhD in Applied Physics, *Materials Science* research group
Zernike Institute for Advanced Materials
University of Groningen
Title thesis: *Material structure and functionality in product manufacturing*
Supervisor: Prof. Jeff Th. M. De Hosson

2012 – 2014   Master degree in Applied Physics,
University of Groningen
Title thesis: *Microscopy study on the onset of plastic deformation and modeling creep behavior of AISI 420 stainless steel*
Supervisor: Prof. Jeff Th. M. De Hosson

2007 – 2012   Bachelor degree in Applied Physics
University of Groningen
Title thesis: *Reconstruction of high-energy neutrino-induced showers*
Supervisor: Prof. Herbert Löhner

Acknowledgements

"*And now… the end is near*", as Frank Sinatra would say. For me, the end is marked by this moment to write the concluding words of my thesis. And so we face the final pages of this apotheosis after four years of research. Although I experienced the freedom to do it *my way*, I surely did not do it alone.

The first person I would like to thank is my promotor Prof. De Hosson ("*please call me Jeff*"). You are an exceptional inspirational mentor. Your broad understanding of science and ability to scrutinize phenomena on so many levels, is unique. I feel privileged to have you as a guide in the journey to find the "meatballs in the scientific soup". Your sense of humour blended with your clear view on scientific matter, made that I always left your office with inspiration and a grin from ear to ear.

Many thanks for my co-promotor Dr. Václav Ocelík. You have taught me a lot on (electron) microscopy and conducting experiments. I enjoyed the many hours we spend together behind the microscopes in the MK-lab, and also our experimental work in Brno. I admire your patience and positive approach.

I would like to express my gratitude to the thesis assessment committee, Prof. Herman Terryn, Prof. Petra Rudolf and Prof. Jan Post, for careful reading of my thesis.

And then… the remarkable Materials Science group. People come and go, but never leave the MK-group. I am grateful that I had the opportunity to work with and learn from such highly skilled people. Special thanks to Michail Dutka, David Vainchtein and Emad Galinmoghaddam. It was not possible to conduct experiments on such a variety of specialist equipment without your technical support. I experienced the MK-group as a thriving atmosphere.

On a more personal note: Leo thank you for the work we did together and cracking jokes on 'Allo 'Allo. You are a good guy with a great sense of humor. Inverse Pole Figures will never be the same. Ondřej… you know why. For the sake of referring, I mention the monkey obstacle course on the Nandi hills. Herman, you

are a one-of-a-kind guy and always willing to help (with everything). I enjoyed our swift and frequent updates. You keep amazing me by being a walking car-encyclopaedia and knowing a bush-type solution for basically every situation. Indranil, I am impressed by your knowledge and calm approach. I am sure you will become a famous professor. Mister Diego thank you for being a good friend, colleague and office mate. I value the mutual level of understanding and the philosophical debates on many topics. Usually our conversations would jump from discussing linguistics to the bossanova and further to physics, without being incoherent. Pineapples could have replaced one of the topics in the previous sentence without changing the outcome. I am not sure if we sometimes *viajar na maionese* there, but it was fun for sure.

I would like to thank the tribology experts Deepak, Angela and Fabio for their great professional insights, and for their culinary and social expertise as well. It is a great pleasure to spend time with you.

The research for this thesis has been done in conjuncture with Philips Drachten. I would like to thank Jan Hovius and Manso Groen for their excellent collaboration. Furthermore, I am grateful to Onno Hoitinga and captain (of industry) Jan Post for enabling the project and a fruitful connection between the University of Groningen and Philips. Thanks to Gerrit K., Ronald, Johan, Mark, Huib, Redmer, Harm, Marijke, Jan S., Willem, Jan v.D., Paul and Steven for their interest in my work and the fun activities (not to forget the table football).

On several topics, I worked together with other research groups. I am very thankful for your collaboration, which resulted in an enrichment of my research. I would like to acknowledge:

Prof. Herman Terryn for your interest and helpful discussions. Also Isabelle Vandendael and Priya Laha from the Vrije Universiteit Brussel, for your work with the Auger Microscope.

Prof. Petra Rudolf for allowing me to work in your lab with XPS.

Dr. Yaiza Gonzalez-Garcia, Dr. Majid Sababi and Aytac Yilmaz from TU-Delft for the experiments on SKPFM and Kelvin Probe. Furthermore Prof. Arjan Mol for his ongoing interest and help.

Tomáš Šamořil and Hana Tesařová from Tescan Orsay, Brno, Czech Republic for the joint ToF-SIMS experiments.

During my PhD I had the privilege to supervise several students. Parts of their work found a place in this thesis. Maxens van Daalen, Sven van der Meer, Roy Blum, Casper Jansen, Mark van der Klok, Kevin Koster, Jannes Hopman, Yahia Mostafa, Vincent Goossens: thank you for your trust in me as a supervisor. As I saw you growing with knowledge, I also learned a lot from you.

Thanks to my paranymphs Mart Johan Deuzeman & Wilco Zuidema. We know each other for a very long time by now. I couldn't imagine that our studies and work would run parallel into this extend. Peculiar, but remarkable and valuable for sure!

Via deze weg wil ik mijn familie bedanken voor hun interesse in mijn werk. Hait en mim, danke wel foor 't onfoorwaardelyke fertrouwen.

Hoewel ik dit dankwoord aanving met de woorden *the end is near*, is het einde niet in zicht. Het proefschrift sluit welliswaar een periode van gefocussed onderzoek af, de opgedane kennis en inzichten zijn daarentegen een ervaring die juist aanzetten tot verder ontdekken. Het is fascinerend om de (fysische) wereld om je heen steeds beter te kunnen doorgronden. Daarmee komt ook de bewustwording dat er ontzettend veel is wat nog ontdekt kan (en moet?) worden. Een prikkelende gedachte die, naar ik hoop, de vlam der nieuwsgierigheid nog lang brandende houdt.

Dieudonnée, ik wil je bedanken voor de ruimte die je mij geboden hebt. Voor jouw oprechte interesse en steun. Steun die mij in moeilijke tijden, maar ook in goede tijden ontzettend veel energie heeft gegeven. Je bent een fantastische en veelzijdige vrouw. Ik hoop dat we lang samen nieuwsgierig kunnen blijven.

Gerrit Zijlstra
Wildervank, augustus 2018